

https://dspace.org/

Palladium-based carbon and ceria nanocomposites as electrocatalysts for fuel cell applications

Ogada, Jimoo Joretta

2021
https://hdl.handle.net/10539/32380

Downloaded from a DSpace repository. https://dspace.org/



PALLADIUM-BASED CARBON AND CERIA NANOCOMPOSITES AS ELECTROCATALYSTS FOR FUEL CELL APPLICATIONS

BY

JIMODO JORETTA OGADA

Student Number: 2200120

A dissertation submitted to the Faculty of Science, University of the Witwatersrand, Johannesburg, in fulfillment of the requirements for the degree of Master of Science.

Supervisors: Prof. Daniel M. Wamwangi and Prof. Kenneth I. Ozoemena

University of the Witwatersrand, Johannesburg, 2020

DECLARATION

I declare that this dissertation is my own, unaided work. It is being submitted for the Degree of Master of Science at the University of the Witwatersrand, Johannesburg. It has not been submitted before for any degree or examination at any other University.



_____

(Signature of candidate)

23rd day of April 2021 at Johannesburg

ABSTRACT

The electrooxidation of alcohol in alkaline media is vital for the development of alkaline direct alcohol fuel cells (ADAFCs). This research investigated and compared the electrocatalytic properties of different alternatives of palladium catalysts supported on carbon black (CB) and onion-like carbon (OLC), and their CeO_2 added counterparts - Pd/CB, Pd/OLC, Pd-CeO_2/CB and Pd-CeO_2/OLC - towards ethanol oxidation.

All the nanocatalysts were characterized by powder x-ray diffraction (PXRD), thermogravimetric analysis (TGA), Raman spectroscopy, transmission electron microscopy (TEM), high resolution transmission electron microscopy (HRTEM), scanning electron microscopy (SEM), x-ray absorption spectroscopy (XAS) and x-ray photoelectron spectroscopy (XPS).

The addition of CeO_2 significantly enhanced anodic performance as compared to carbon-only-based support for palladium. Half-cell reactions were studied, and Pd-CeO_2/OLC was observed to be the best of the four nanomaterials for EtOH oxidation reaction in terms of current densities (highest current density), smaller peak-to-peak separation (faster electron transport), higher j_f/j_b value (less poisoning from products of the intermediate reaction) and the lowest resistance to current flow as seen in the EIS results.

The Pd nanocatalysts were explored for hydrogen oxidation and oxygen reduction in alkaline environment. Pd-CeO_2/OLC showed the best behaviour towards both experiments, evidenced by higher current density. The addition of CeO_2 to the electrocatalysts enhances their performances toward the alkaline HOR and ORR. For ORR, the catalysts containing OLC showed better electrocatalysis.

DEDICATION

This work is specially dedicated to Adonai the Almighty, to my dad, Dr Joseph E. J. Ogada, my mum, Mrs Ngozi T. Ogada, my siblings, especially my twin brother Jide Joret Ogada and my sister Mrs Jiro Joanna Ogada-Christian, and my grandparents (of blessed memory) Raymond Iheanacho Ogada, Rosanna Nkwuzo Ogada, Stephen Anyanwu Oguguo and Cecilia Ukachi Anyanwu.

ACKNOWLEDGEMENTS

I would like to express my deep appreciation to Professor Daniel Wamwangi and Professor Kenneth Ozoemena for the opportunity to work on this interesting project. Every chat we had about my results gave me better understanding. I cannot thank you enough for your patience, guidance and for giving me all the support you could give.

Many thanks to members of the School of Physics and of Chemistry who helped make my experience more fulfilling. Special thanks to Adewale and Refiloe of the Ozoemena group for helping me get settled and finding my way around Wits University and my project and to Dr Patrick Mwonga for the DFT simulations.

I am thankful to Prof. Alexander Ziegler and Prof. Dave Billing for letting me use instruments in their respective facilities - the microscopy and microanalysis unit (MMU) and the powder X-ray diffraction spectroscopy unit (PXRDU). I thank Dr. Rudolph Erasmus for kindly assisting me with the Raman spectroscopy and Adam for PXRD, as well as the members of the MMU staff who kindly trained me on the use of instruments. I also thank Prof Shaowei Chen’s group (Department of Chemistry and Biochemistry, University of California at Santa Cruz, USA) for their assistance with the acquisition of the Synchrotron data. I am very grateful to Dr Dean Barrett (Wits School of Chemistry) for assistance with analyzing the XAS data. I thank Prof Frank Marken’s group (Department of Chemistry, University of Bath, UK) for assistance with the acquisition of the HRTEM data.

My unreserved thanks to Dee Ik Osuagwu and Daddy Solo Nwachukwu for being ever supportive on this journey. I am grateful to the Ozoemena family for a warm reception to South Africa and to my family and good friends for prayers and encouragement all the way. I would also love to express my sincere appreciation to the DST-NRF for financial support.

RESEARCH OUTPUT ARISING FROM THIS WORK

CONFERENCE PRESENTATIONS

1. Jimodo J. Ogada, Suhail Musa, Adewale Ipadeola, Hamish Miller, Francesco Vizza, Kenneth Ozoemena, Daniel Wamwangi (2019). Pd/C/CeO_2 as Electrocatalyst for Alcohol Fuel Cell. Energy Storage and Industry 4.0: Challenges and Prospects (ENSTIN 2019). Held July 31 – August 2, 2019 at KwaMaritane Bush Lodge, Pilanesburg National Park, South Africa.

2. Jimodo J. Ogada, Suhail Musa, Adewale Ipadeola, Hamish Miller, Francesco Vizza, Kenneth Ozoemena, Daniel Wamwangi (2019). Pd/C/CeO_2 as Electrocatalyst for Alcohol Fuel Cell. 70th Annual Meeting of the International Society of Electrochemistry. Held August 4 – 9, 2019 at the International Conference Centre, Durban, South Africa.

MANUSCRIPTS FOR PUBLICATION

1. Peer-Reviewed Publications (Under Editing for Submission) Jimodo J. Ogada, Adewale K. Ipadeola, Daniel M. Wamwangi, And Kenneth I. Ozoemena. A Comparative Study of Pd/CB And Pd/OLC As Electrocatalysts For Alkaline Direct Alcohol Fuel Cells (To Be Submitted to Phys Chem Chem Phys)

2. Jimodo J. Ogada, Adewale K. Ipadeola, Dean Barrett, Daniel M. Wamwangi, And Kenneth I. Ozoemena. Pd-CeO_2/OLC As Efficient Electrocatalyst For Alkaline Direct Ethanol Fuel Cell: Insights into CeO_2-

Induced Conductivity and Electron Transport (To Be Submitted to ACS Catalysis)

3. Jimodo J. Ogada, Adewale K. Ipadeola, Daniel M. Wamwangi, and Kenneth I. Ozoemena. A Comparative Study of Pd-CeO_2/CB and Pd-CeO_2/OLC as Electrocatalysts Oxygen Reduction and Hydrogen Oxidation Reactions in Alkaline Medium (To Be Submitted to J Phys Chem C).

CONTENTS

DECLARATION i

ABSTRACT ii

DEDICATION iii

ACKNOWLEDGEMENTS iv

RESEARCH OUTPUT ARISING FROM THIS WORK v

CONFERENCE PRESENTATIONS v

MANUSCRIPTS FOR PUBLICATION v

LIST OF FIGURES xii

LIST OF SCHEMES xvii

LIST OF TABLES xviii

LIST OF ABBREVIATIONS AND NOMENCLATURE xx

CHAPTER 1 1

INTRODUCTION 1

1.1 Motivation and Rationale 1

1.2 Statement of Research Problem 3

1.3 Research Aims and Objectives 4

1.4 Structure of the Dissertation 4

References 6

CHAPTER 2 10

LITERATURE REVIEW 10

2.1 Fuel Cell Technology 10

2.2 Types of Fuel Cell 11

2.2.1 Solid Oxide Fuel Cells (SOFC) 11

2.2.2 Proton Exchange Membrane (PEM) Fuel Cell 12

2.2.3 Alkaline Fuel Cells (AFC) 15

2.2.4 Molten Carbonate Fuel Cells (MCFCs) 16

2.2.5 Phosphoric Acid Fuel Cells (PAFC) 16

2.3 Fundamental Electrochemical Reactions for Fuel cells 20

2.3.1 Cathode Reaction: Oxygen Reduction Reaction (ORR) 20

2.3.2 Anode Reaction: Hydrogen Oxidation Reaction 21

2.3.3 Anode Reaction: Alcohol Oxidation Reaction 22

2.3 Direct Alcohol Fuel Cell (DAFC) 23

2.4 Alkaline Direct Alcohol Fuel Cells (ADAFCs) 23

2.4.1 Background of the Alkaline Direct Ethanol Fuel Cell (ADEFC) .. 23

2.4.2 Working Principle of Alkaline Direct Ethanol Fuel Cell 24

2.5 Nanostructured Palladium-based Electrocatalysts 26

2.5.1 Methods for the Preparation and Deposition of Nanostructured Materials 26

2.6 Electrochemical Techniques 34

2.6.1 Electrodes and Preparation for Use 35

2.6.2 Cyclic Voltammetry (CV) 37

2.6.3 Electrochemical Impedance Spectroscopy (EIS) 40

2.6.4 Chronoamperometry 43

2.6.5 Linear Sweep Voltammetry 44

2.7.5 Rotating Disk Electrode (RDE) and Rotating Ring Disk Electrode (RRDE) 46

2.7.6 Models Used in Potentiodynamic Experiments. 47

References 51
Chapter 3 METHODOLOGY 66
3.1 Synthesis Procedures 66
3.1.1 Synthesis of Pd/Carbon (10wt%) 66
3.1.2 Synthesis of Carbon-CeO_2 support (50:50) 67
3.1.3 Synthesis of Pd/CeO_2-CB (10wt%Pd) 67
3.1.4 Synthesis of Pd/CeO_2-OLC (10wt%Pd) 68
3.2 Material Characterization Methods 69
3.2.1 Powder X-ray diffraction (structure determination) 69
3.2.2 Raman spectroscopy 69
3.2.3 Energy dispersive X-ray spectroscopy (EDS) 71
3.2.4 Scanning electron microscopy (SEM) 72
3.2.5 Transmission electron microscopy (TEM) analysis 72
3.2.6 Thermogravimetric analysis (TGA) 74
3.2.7 Brunauer-Emmett-Teller (BET) surface area analysis 75
3.2.8 X-ray Photoelectron Spectroscopy (XPS) / Electron Spectroscopy for Chemical Analysis (ECSA) 76
3.2.9 X-ray Absorption Spectroscopy (XAS) 77
3.3 Electrochemical Measurements 78
3.3.1: Three-Electrode Configuration 79
3.3.2: Two-electrode configuration for full cell test 79
3.4 DFT Simulation 80
References 81
CHAPTER 4 87

RESULTS AND DISCUSSION 87
4.1 Materials Characterization 87
4.1.1 XRD spectroscopy of the electrocatalysts 87
4.1.2 Raman spectroscopic analysis of the nanocatalysts 89
4.1.3 Chemical composition and particle morphology analyses 91
4.1.4 High Resolution Transmission Electron Microscopy (HRTEM) . 96
4.1.5 Thermogravimetric analysis of the nanocatalysts 97
4.1.6 Evaluation of surface area and pore volume of the samples 99
4.1.7 X-Ray Absorption Spectroscopy (XAS) 99
4.1.8 X-ray Photoelectron Spectroscopy (XPS) 102
4.1.9 Electrode Surface Coverage Analysis 112
4.2 Ethanol Oxidation Reaction (EOR) 113
4.2.1 Cyclic Voltammetry (CV) 114
4.2.2 Linear Sweep Voltammetry (LSV) 122
4.2.3 Chronoamperometry (CA) 125
4.2.4 Electrochemical Impedance Spectroscopy (EIS) 126
4.2.5 Direct Ethanol Micro-Fuel Cell (μ-DEFC) Measurement 129
4.2.6 DFT Simulation for EOR 133
4.3 Hydrogen Oxidation Reaction 137
4.3.1 HOR Polarization Curves 139
4.3.2 Stability tests (HOR) 146
4.3.3 DFT Simulation Results 147
4.4 Oxygen Reduction Reaction (ORR) 149
4.4.1 ORR Polarization Curves 150

4.4.2 Accelerated Durability Test 154
4.4.3 Tolerance to ethanol crossover effect 155
4.4.4 DFT Simulation Results 156
References 159
CHAPTER 5 169
CONCLUSION AND RECOMMENDATION 169
5.1 Conclusion 169
5.1.1 Physical Properties 169
5.1.2 Ethanol Oxidation and ADEFC Test 169
5.1.3 Electrocatalysts for Hydrogen Oxidation and Oxygen Reduction Reactions in Alkaline Environment 170
5.2 Recommendations for Future Directions 170

LIST OF FIGURES

Figure 2.1: Cyclic voltammogram of a single electron redox reaction

Figure 2.2: (a,b) Nyquist plots with their respective Voigt *EEC* models and circuit elements (R_s, R_{ct}, $C_{dl,}$ and Z_{CPE}), and (c,d) typical Bode plots

Figure 2.3: A typical CA curve of Pd electrocatalyst at $E_{1/2}$ or OCV for EOR

Figure 2.4: A typical linear sweep voltammogram for (a) EOR (b) HOR (c) ORR

Figure 2.5: Schematic representation of a typical (a) RDE and (b) RRDE

Figure 2.6: (a) Koutecky-Levich plot and (b) Butler-Volmer plot for a potentiodynamic system.

Figure 3.1: Bruker Senterra laser Raman spectrometer.

Figure 3.2: FEI Tecnai T12 Transmission Electron Microscope.

Figure 3.3: Thermal analyzer used for the TGA.

Figure 3.4: The micromeritics RS232 Brunauer -Emmett-Teller (BET) surface area analyzer.

Figure 3.5 ***Left***: XAFS K-edge signal of crystalline copper (indicating the XANES and EXAFS region) and ***Right***: Argon

Figure 3.6: A three-electrode configuration for half-cell reactions.

Figure 3.7: A two-electrode 3D-printed cell.

Figure 4.1: XRD patterns of the Pd/CB, Pd-CeO_2/CB, Pd/OLC and Pd-CeO_2/OLC nanocatalysts.

Figure 4.2: Raman spectra of the nanocatalysts.

Figure 4.3: EDS spectrum of Pd/CB, Pd/OLC, Pd-CeO_2/CB and Pd-CeO_2/OLC.

Figure 4.4: SEM images of (A) Pd/CB (B) Pd-CeO_2/CB (C) Pd/OLC (D) Pd-CeO_2/OLC.

Figure 4.5: TEM images of (A) Pd/CB (B) Pd-CeO_2/CB (C) Pd/OLC (D) Pd-CeO_2/OLC.

Figure 4.6: The particle size distribution of the nanocatalysts. (A) Pd/CB (B) Pd-CeO_2/CB (C) Pd/OLC (D) Pd-CeO_2/OLC

Figure 4.7: HRTEM images of the samples.

Figure 4.8: (a) TGA of the nanocatalysts and the (b) Derivative Thermogravimetry (DTGA).

Figure 4.9. (A) Fourier transform of k^2-weighted spectrum (not phase corrected) and best fit for the samples 004, 005 and 006. (B) Fourier transform, best fit and fit contributions for the sample 004. (C) Normalized XANES spectra at Pd K-edge for all the samples and metallic reference.

Figure 4.10: XPS of the Pd/CB, Pd-CeO_2/CB, Pd/OLC and Pd-CeO_2/OLC nanocatalysts.

Figure 4.11: XPS C 1s scans of the Pd/CB, Pd-CeO_2/CB, Pd/OLC and Pd-CeO_2/OLC nanocatalysts.

Figure 4.12: XPS O 1s scans of the Pd/CB, Pd-CeO_2/CB, Pd/OLC and Pd-CeO_2/OLC nanocatalysts.

Figure 4.13: XPS Pd 3d scans of the Pd/CB, Pd-CeO_2/CB, Pd/OLC and Pd-CeO_2/OLC nanocatalysts.

Figure 4.14: XPS Ce 3d scans of the Pd-CeO_2/CB and Pd-CeO_2/OLC nanocatalysts.

Figure 4.15: Valence band spectra of the Pd/CB, Pd-CeO_2/CB, Pd/OLC and Pd-CeO_2/OLC nanocatalysts.

Figure. 4.16: Cyclic voltammograms of the bare and modified GCE.

Figure 4.17: Cyclic voltammograms of Pd/CB, Pd/OLC, Pd-CeO_2/CB and Pd-CeO_2/OLC (a) Specific activity (b) Mass activity.

Figure 4.18: Cyclic voltammograms of the EOR of the electrocatalysts (a) Specific activity (b) Mass activity.

Figure 4.19: Scan rate studies of the Pd-based catalysts.

Figure 4.20: Plot of current density against the square root of the scan rates for the EOR of Pd/CB, Pd/OLC, Pd-CeO_2/CB and Pd-CeO_2/OLC.

Figure 4.21: LSV concentration studies of (a) Pd/CB (b) Pd-CeO_2/CB (c) Pd/OLC (d) Pd-CeO_2/OLC.

Figure 4.22: Tafel Plot of the EOR at the Pd-CeO_2/OLC electrode.

Figure 4.23: CA evolutions of the Pd electrocatalysts.

Figure 4.24: Nyquist plots of the electrocatalysts.

Figure 4.25: Bode plots: (log Z vs log f) and their corresponding (phase angle vs log f).

Figure 4.26: A two-electrode set-up consisting of the micro 3D-printed cell for ADEFC test.

Figure 4.27: (a) potential and power curves, (b) galvanostatic discharge test at 20 mA cm^{-2}

Figure 4.28: (a) Nyquist plot of the Pd/CB, Pd/OLC, Pd-CeO_2/CB and Pd-CeO_2/OLC using a 3D-printed cell; and (b) the Voigt EEC model.

Figure 4.29: Electronic energy band structures of the Pd surfaces of Pd/CB (a), Pd/OLC (b), Pd-CeO_2/CB (c) and Pd-CeO_2/OLC (d).

Figure 4.30: The interactions between the ethanol molecule and the different palladium catalysts.

Figure 4.31: Cyclic voltammograms at the (b) Pd/CB (c) Pd/OLC (d) Pd-CeO_2/CB (e) Pd-CeO_2/OLC electrodes.

Figure 4.32: HOR Polarization curves at (a) Pd/CB (b) Pd/OLC (c) Pd-CeO_2/CB (d) Pd-CeO_2/OLC (e) 1600 rpm.

Figure 4.33: (a-d) Koutecky-Levich plot at different overpotential (η = 0.65, 0.7, 0.75, 0.8 and 0.85 V).

Figure 4.34: (a-d) Butler-Volmer plots of electrocatalysts.

Figure 4.35: The HOR Tafel plots of the electrocatalysts.

Figure 4.36: Chronoamperometry of the electrocatalysts @ 0.3 V vs. RHE and 1600 rpm.

Figure 4.37: LSV after the 1st and 1000th cycles of CV (50 mVs^{-1}) at 1600 rpm (a) Pd/CB (b) Pd/OLC (c) Pd-CeO_2/CB (d) Pd-CeO_2/OLC.

Figure 4.38: The interactions between the hydrogen molecule and the different palladium catalysts.

Figure 4.39: The Metrohm Autolab workstation.

Figure 4.40: (a) CV curves (b) Linear sweep voltammograms at 1600 rpm**.**

Figure 4.41: Linear sweep voltammograms for the catalysts at rotation rates between 400 and 2500 rpm.

Figure 4.42: (a-d) The K-L plots for the samples at various overpotentials (0.3, 0.35, 0.4, 0.45 and 0.5 V). (e) Tafel plots of all the samples 10 wt% Pd.

Figure 4.43: Stability test of the Pd-CeO_2/OLC catalysts towards ORR at the rotation rate of 1600 rpm after 5000 and 15000 cycles.

Figure 4.44: Cyclic voltammetric evolutions of the samples in oxygen-saturated KOH with and without ethanol.

Figure 4.45: The interactions between the adsorbates of ORR and the different palladium catalysts.

LIST OF SCHEMES

Scheme 1.1: Illustration of an energy management system

Scheme 2.1: Solid Oxide Fuel Cell (SOFC)

Scheme 2.2: Schematic diagram of the PEMFC

Scheme 2.3: Alkaline Fuel Cells (AFC)

Scheme 2.4: Molten Carbonate Fuel Cells (MCFC)

Scheme 2.5: Phosphoric Acid Fuel Cells (PAFC)

Scheme 2.6: Alkaline Direct Ethanol Fuel Cell Operation Scheme

Scheme 2.7: Schematic illustration of ALD Method

Scheme 2.8: Schematic illustration of the ECD system

Scheme 2.9: A representation of the spray pyrolysis method

Scheme 2.10: Schematic illustration of the sol-gel method

Scheme 2.11: An illustration of the hydrothermal/solvothermal processes

Scheme 2.12: Comparing the conventional heating process to the microwave-assisted heating

Scheme 2.13: Schematic representation of a three-electrode electrochemical setup

Scheme 3.1: Procedures for synthesis of Pd/Carbon

Scheme 3.2: Procedures for synthesis of Pd-CeO_2/Carbon

LIST OF TABLES

Table 2.1: The different fuel cells and their properties

Table 2.2: Electrochemical reactions of the different fuel cell types

Table 4.1: Lattice parameters of the Pd -based electrocatalysts at 2θ of *ca.* 40º

Table 4.2: Summary of the Raman data for the nanocatalysts

Table 4.3: BET surface areas and porosity of the electrocatalysts

Table 4.4: Fit results of the EXAFS data

Table 4.5: (a) XPS atomic percentage of each constituent element **(b)** Elemental identification of Pd/CB **(c)** Elemental identification of Pd-CeO_2/CB **(d)** Elemental identification of Pd/OLC **(e)** Elemental identification of Pd-CeO_2/OLC

Table 4.6: EOR data obtained at the Pd/CB, Pd-CeO_2/CB, Pd/OLC and Pd-CeO_2/OLC electrodes.

Table 4.7: Electrocatalytic properties of the Pd-CeO_2/OLC electrocatalyst towards EOR in alkaline media compared to other works (*n/a* not available).

Table 4.8: EIS values obtained at the electrodes.

Table 4.9: EIS parameters of the Pd-based electrocatalysts for the µ-DEFC

Table 4.10: Energies calculated for the Ethanol-Pd configurations.

Table 4.11: $j_{o,s}$ and $j_{o,m}$ of Pd/CB, Pd-CeO_2/CB, Pd/OLC and Pd-CeO_2/OLC

Table 4.12: Tafel slope values of the electrocatalysts at different regions.

Table 4.13: The different energies calculated for the HOR at the electrodes.

Table 4.14: Summary of the ORR performance (@ 1600 rpm)

Table 4.15: The different energies calculated for the ORR at the electrodes.

LIST OF ABBREVIATIONS AND NOMENCLATURE

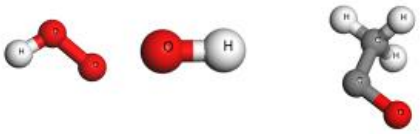
Abbreviation	Description
ADEFC	Alkaline Direct Ethanol Fuel Cell
AFC	Alkaline Fuel Cell
Ag|AgCl	Silver/Silver Chloride
BET	Branauer-Emmett-Teller
CA	Chronoamperometry
CB	Carbon black
CE	Counter electrode
CeO_2	Cerium Oxide
CH_3CH_2OH	Ethanol
CH_3COOH	Acetic acid
cm	Centimeters
CPE	Constant Phase Element
CV	Cyclic Voltammetry
D.C.	Direct Current
DEFC	Direct Ethanol Fuel Cell
DEGFC	Direct ethanol gas fuel cell

DLC	Double Layer Capacitance
E	Ideal potential of the cell
ECSA	Electrochemically Active Surface Area
EDS	Energy Dispersive X-ray Spectroscopy
EEC	Electronic Equivalent Circuit
EIS	Electrochemical Impedance Spectroscopy
EOR	Ethanol oxidation reaction
F	Faraday's constant
FC	Fuel Cell
FWHM	Full Width at Half Maximum
GCE	Glassy carbon electrode
GDL	Gas diffusion layers
HOR	Hydrogen Oxidation Reaction
HRTEM	High resolution transmission electron microscopy
I	Current
ID	Intensity of the distorted graphitic band of CNS
IG	Intensity of the ordered graphitic band of CNS
J	Current density
$j_{o,s}$	Exchange current density
$j_{o,m}$	Mass activity
LSV	Linear Sweep Voltammetry
mA	Milliamperes

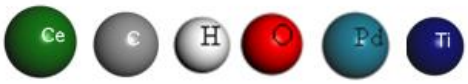
MCFC	Molten Carbonate Fuel Cell
MEA	Membrane Electrode Assembly
mg	Milligram
min	Minutes
mL	Millilitre
N_2	Nitrogen
nm	Nanometer
O_2	Oxygen
OLC	Onion-Like Carbon
ORR	Oxygen Reduction Reaction
PAFC	Phosphoric Acid Fuel Cell
Pd	Palladium
PEIS	Potentiostatic Electrochemical Impedance Spectroscopy
PEM	Proton Exchange Membrane or Polymer Electrolyte Membrane
PEMFC	Proton Exchange Membrane Fuel Cell
Pt	Platinum
PXRD	Powder X-ray diffraction
R	Resistance
R_{ct}	Capacitive resistance
RDE	Rotating disk electrode
RDS	Rate-determining step
RE	Reference electrode

RHE	Reversible hydrogen electrode
rpm	Revolution per minute
R_s	Series connection resistance
s	seconds
SEM	Scanning electron microscopy
SOFC	Solid Oxide Fuel Cell
TEM	Transmission electron microscopy
TEM	Transmission Electron Microscopy
TGA	Thermogravimetric Analysis
TGA	Thermo-Gravimetric Analysis
WE	Working Electrode
wt %	Weight percentage
XAS	X-Ray Absorption Spectroscopy
XPS	X-Ray Photoelectron Spectroscopy
XRD	X-Ray Diffraction
Z’	Real impedance
Z”	Imaginary impedance
θ	Scattering angle
λ	Wavelength
ω	Frequency

Adsorbates



Atoms Key



CHAPTER 1

INTRODUCTION

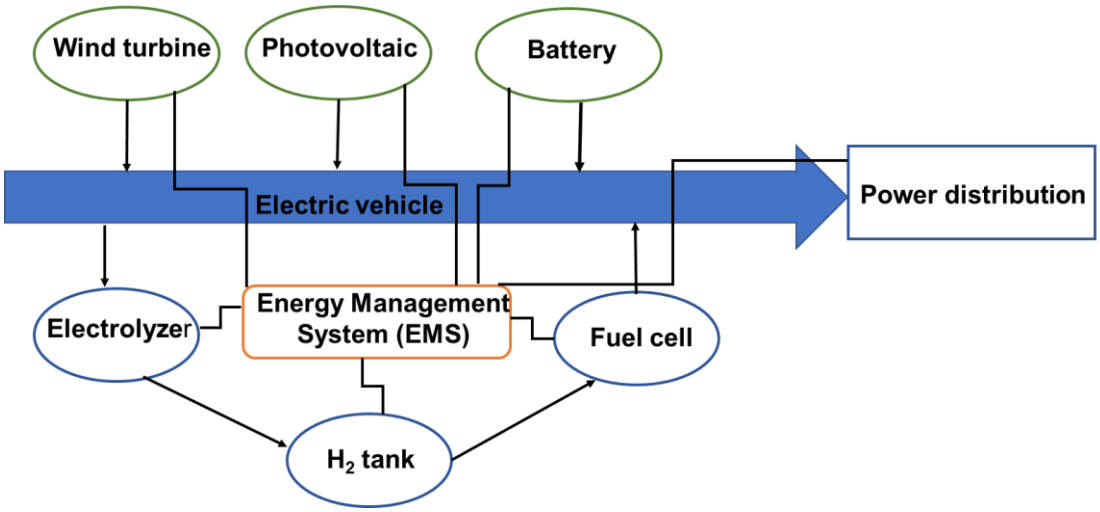
This chapter summarizes the motivation and objectives of this research project, as well as the structure of the dissertation.

1.1 Motivation and Rationale

Electricity is a form of energy which is commonly used in the world today and an essential part of modern technology. Motor vehicles, aircrafts, cellphones, internet, heating system, among others depend on this form of energy to function.

This ever-growing, incessant need of electricity leads to an increase in the consumption of fossil fuels, which has adverse effects on health and environment, causing global warming. Hence, it is imperative that sources of clean energy which are economical and environmentally friendly be developed and commercialized.

The energy management system (EMS) (**Figure 1.1**) comprises of various renewable energy sources that are a sure way to generate large amounts of energy to meet the enormous demands [1]. Amongst these sources, fuel cell (FC) technology has a unique energy impact and is one of the most recommended renewable energy for power generation facilities [2].



Scheme 1.1: Illustration of an energy management system [2].

The alkaline electrolyte membrane fuel cell (AEMFC) is one of the most advanced technology, which has, in recent times attracted great attention due to such intriguing properties like: fast cathodic kinetic, improved electrocatalytic stability and activity, better water (H_2O) management mitigating flooding and the use of non-precious metals as electrocatalysts for cathodic reactions.

This research focuses on the AEMFCs with characteristic improved performances and reduced cost of fabrication. The most common fuels used in the FC technologies are hydrogen (H_2) and small molecular weight alcohols like ethanol (EtOH) and methanol (MeOH). Hydrogen and ethanol fuels have been explored in this research because of their low toxicity, and ease of production from abundant resources.

Alkaline direct ethanol fuel cells (ADEFCs) are among the most renewable, viable and portable electrochemical devices that have been developed in recent times due to the impressive properties of the ethanol fuel like its high theoretical energy density, affordability, easy transportation and storage, and high-octane rating making it possible to use them in internal combustion engine. It is also non-toxic. [3,4]. Moreover, large quantities of ethanol can be produced from agricultural and organic municipal wastes. 90 million liters of

ethanol are produced globally from agricultural and organic domestic wastes every year [5]. The ADEFC tends to reduce greenhouse gas (GHG) emission. Therefore, it is a good alternative to the fossil fuel technology as it is no threat to the the environment and health. The ADEFCs are applicable in portable, stationary, and transportation auxiliary devices.

1.2 Statement of Research Problem

Although Pt is the catalyst that is mostly used for fuel cell technology, the commercialization of the direct ethanol fuel cell (DEFC) has been unsuccessful due to the high cost of using Pt catalyst at both electrodes (anode and cathode), unwanted side reactions with intermediate atoms/anions such as OH^-, causing poor utilization of Pt catalyst, poor tolerance of Pt to carbonaceous species poisoning, the use of carbon (which is prone to corrosion in acidic media) as catalyst support to reduce loading.

Additionally, alcohols are not easily oxidized on platinum or its alloys. There is no platinum-based anode catalyst known to generate power densities that are high enough for the DEFC, except in cases where partially inorganic solid electrolytes are used at certain temperatures [6,7,27,28]. Hence the need to design new platinum-free catalysts for DAFC anodes or catalytic structures that contain only tiny amounts of platinum. Pd-based electrocatalysts are gaining a lot of attention because palladium has been found to be more abundant than platinum and less expensive to use as it efficiently oxidizes many different substrates in alkaline media, where non-noble metals can also be stable and function sufficiently [8,9]. The Pd-non-noble metal compatibility means that the cost of using the membrane electrode assemblies (MEAs) would be less. A decrease in the cost of production can boost the commercialization of DAFCs.

The numerous benefits of alkaline environments, such as the possibility of using less expensive non-noble metals, alcohol oxidation at lower anodic

overpotentials, limited alcohol crossover from the anode side of the cell to the cathode side, less risk of corrosion and less poisoning effects, make it possible for efficient operation of alkaline fuel cells [10-26].

1.3 Research Aims and Objectives

The aim of this research project is to explore the feasibility of using palladium-based nanocomposites - Pd/CB, Pd/OLC, Pd-CeO_2/CB, and Pd-CeO_2/OLC - to develop alcohol fuel cells for the development of power-generating fuel cell materials.

This study involves synthesizing the different palladium-based catalysts and evaluating their physical characteristics – structural and morphological properties - and how they affect the catalytic behaviors of the samples. The electrochemical properties for ethanol oxidation reaction (EOR), as well as oxygen reduction and hydrogen oxidation reactions are also evaluated using cyclic voltammetry (CV), linear sweep voltammetry (LSV), chronoamperometry (CA), and electrochemical impedance spectroscopy (EIS).

The micro direct ethanol gas fuel cell (DEGFC) is designed, fabricated and tested to prove the EOR concept.

1.4 Structure of the Dissertation

Chapter one discusses the rationale behind this research, as well as the aim and objectives.

Chapter two gives a brief overview of the types of fuel cell and their applications.

Chapter three presents the methodology used for the different studies conducted in this research.

Chapter four discusses the physical properties of the nanocomposites and their behaviors toward EOR, while **Chapter five** discusses the behavior of the electrocatalysts towards HOR and ORR.

Finally, **Chapter six** concludes the dissertation and gives suggestions for future directions.

References

1. M. S. H. Nizami, A. N. M. M. Haque, P. H. Nguyen, and M. J. Hossain, “On the application of Home Energy Management Systems for power grid support,” *Energy*, 2019, 188, 1-14. doi: 10.1016/j.energy.2019.116104.

2. P. J. Hall and E. J. Bain, “Energy-storage technologies and electricity generation,” *Energy Policy*, 2008, 36, 4352 – 4355. doi: 10.1016/j.enpol.2008.09.037.

3. K. I. Ozoemena, “Nanostructured platinum-free electrocatalysts in alkaline direct alcohol fuel cells: Catalyst design, principles and applications,” *RSC Advances*. 2016, 6, 89523 – 89550. doi: 10.1039/c6ra15057h.

4. R. Othman, A. L. Dicks, Z. Zhu, “Non-precious metal catalysts for the PEM fuel cell cathode,” *International Journal of Hydrogen Energy*, 2012, 37, 357 – 372. https://doi.org/10.1007/s11814-017-0202-2.

5. S. P. S. Badwal, S. Giddey, A. Kulkarni, J. Goel, S. Basu, “Direct ethanol fuel cells for transport and stationary applications – A comprehensive review” *Applied Energy*, 2015, 145, 80 – 103. 10.1016/j.apenergy.2015.02.002.

6. C. Lamy, A. Lima, V. LeRhun, F. Delime, C. Coutanceau, and J. M. Léger, “Recent advances in the development of direct alcohol fuel cells (DAFC),” in *Journal of Power Sources*, 2002, 105(2), 283-296. doi: 10.1016/S0378-7753(01)00954-5.

7. Peled, V. Livshits, and T. Duvdevani, “High-power direct ethylene glycol fuel cell (DEGFC) based on nanoporous proton-conducting membrane (NP-PCM),” in *Journal of Power Sources*, 2002, 106(1-2), 245-248. doi: 10.1016/S0378-7753(01)01028-X.

8. J. Greeley *et al.*, “Alloys of platinum and early transition metals as oxygen reduction electrocatalysts,” *Nat. Chem.*, 2009, 1(7):552-6. doi: 10.1038/nchem.367.

9. C. Bianchini and P. K. Shen, “Palladium-based electrocatalysts for alcohol oxidation in half cells and in direct alcohol fuel cells,” *Chem. Rev.*, 2009, 109, 9, 4183–4206. doi: 10.1021/cr9000995.

10. A. V. Tripkovi, K. D. Popovi, B. N. Grgur, B. Blizanac, P. N. Ross, and N. M. Markovi, “Methanol electrooxidation on supported Pt and PtRu catalysts in acid and alkaline solutions,” *Electrochim. Acta*, 2002, 47(22-23), 3707-3714. doi: 10.1016/S0013-4686(02)00340-7.

11. J. Prabhuram and R. Manoharan, “Investigation of methanol oxidation on unsupported platinum electrodes in strong alkali and strong acid,” *J. Power Sources*, 1998, 74(1), 54-61. doi: 10.1016/S0378-7753(98)00012-3.

12. A. S. Arico, V. Baglio, and V. Antonucci, *Direct methanol fuel cells*. 2010. https://doi.org/10.1201/9781439833148.ch5

13. J. R. Varcoe, R. C. T. Slade, and E. Lam How Yee, “An alkaline polymer electrochemical interface: A breakthrough in application of alkaline anion-exchange membranes in fuel cells,” *Chem. Commun.*, 2006, 1428-1429. doi: 10.1039/b600838k.

14. J. R. Varcoe and R. C. T. Slade, “An electron-beam-grafted ETFE alkaline anion-exchange membrane in metal-cation-free solid-state alkaline fuel cells,” *Electrochem. commun.*, 2006, 8(5), 839-843. doi: 10.1016/j.elecom.2006.03.027.

15. J. R. Varcoe, R. C. T. Slade, E. L. H. Yee, S. D. Poynton, and D. J. Driscoll, “Investigations into the ex situ methanol, ethanol and ethylene glycol permeabilities of alkaline polymer electrolyte membranes,” *J. Power Sources*, 2007, 173(1), 194-199. doi: 10.1016/j.jpowsour.2007.04.068.

16. T. Xu, “Ion exchange membranes: State of their development and perspective,” *Journal of Membrane Science*, 2005, 263(1-2), 1-29. doi: 10.1016/j.memsci.2005.05.002.

17. J. Fang and P. K. Shen, “Quaternized poly(phthalazinon ether sulfone ketone) membrane for anion exchange membrane fuel cells,” *J. Memb. Sci.*, 2006, 285(1-2), 317-322. doi: 10.1016/j.memsci.2006.08.037.

18. H. Hou, G. Sun, R. He, Z. Wu, and B. Sun, “Alkali doped polybenzimidazole membrane for high performance alkaline direct ethanol fuel cell,” *J. Power Sources*, 2008, 182(1), 95-99. doi: 10.1016/j.jpowsour.2008.04.010.

19. K. Scott, E. Yu, G. Vlachogiannopoulos, M. Shivare, and N. Duteanu, “Performance of a direct methanol alkaline membrane fuel cell,” *J. Power Sources*, 2008, 175(1), 452-457. doi: 10.1016/j.jpowsour.2007.09.027.

20. Yu, E. H., & Scott, K. (2004). Development of direct methanol alkaline fuel cells using anion exchange membranes. *Journal of Power Sources*, 2004, 137(2), 248-256. https://doi.org/10.1016/j.jpowsour.2004.06.004.

21. Y. Xiong, Q. L. Liu, A. M. Zhu, S. M. Huang, and Q. H. Zeng, “Performance of organic-inorganic hybrid anion-exchange membranes for alkaline direct methanol fuel cells,” *J. Power Sources*, 2009, 186 (2), 328-333. doi: 10.1016/j.jpowsour.2008.10.070.

22. É. Agel, J. Bouet, J. F. Fauvarque, and H. Yassir, “The use of a solid polymer electrolyte in alkaline fuel cells,” *Ann. Chim. Sci. des Matériaux*, 2001, 26(4), 59-68. doi: 10.1016/S0151-9107(01)80070-2.

23. H. Bunazawa and Y. Yamazaki, “Influence of anion ionomer content and silver cathode catalyst on the performance of alkaline membrane electrode assemblies (MEAs) for direct methanol fuel cells (DMFCs),” *J. Power Sources*, 2008, 182(1), 48-51. doi: 10.1016/j.jpowsour.2008.03.068.

24. S. Lu, J. Pan, A. Huang, L. Zhuang, and J. Lu, “Alkaline polymer electrolyte fuel cells completely free from noble metal catalysts,” *Proc. Natl. Acad. Sci. U. S. A.*, 2008, 105 (52), 20611-20614. doi: 10.1073/pnas.0810041106.

25. Weaver, M. J. (1997). Modern Aspects of Electrochemistry, No. 29 Edited by J. O’M. Bockris (Texas A&M University), B. E. Conway (University of Ottowa), and R. E. White (University of South Carolina). Plenum Press: New York, 1996. xi + 490 pp. ISBN 0-306-45162-X. *Journal of the American Chemical Society*. https://doi.org/10.1021/ja9656558

26. C. Lamy, C. Coutanceau, and J. M. Leger, “The Direct Ethanol Fuel Cell: A Challenge to Convert Bioethanol Cleanly into Electric Energy,” in *Catalysis for Sustainable Energy Production*, 2009, 1-46. DOI: 10.1002/9783527625413.ch1

27. F. Vigier, S. Rousseau, C. Coutanceau, J. M. Leger, and C. Lamy, “Electrocatalysis for the direct alcohol fuel cell,” in *Topics in Catalysis*, 2006, 40, 111–121. doi: 10.1007/s11244-006-0113-7.

28. E. Antolini, “Catalysts for direct ethanol fuel cells,” *Journal of Power Sources*. 2007, 170(1), 1–12. doi: 10.1016/j.jpowsour.2007.04.009.

CHAPTER 2

LITERATURE REVIEW

2.1 Fuel Cell Technology

A fuel cell (FC) is a renewable/clean energy-generating device that converts the chemical energy in a fuel into electrical energy [1]. All fuel cells have two electrodes - the anode and the cathode. It is at these electrodes that the electrochemical reactions (such reactions that produce electricity from chemical reaction) take place.

An electrolyte is a medium through which protons can move between the electrodes. Therefore, a good electrolyte is one that is a good proton conductor and a good electronic insulator. The electrolyte also physically separates the half-reactions (oxidation and reduction) occurring at the electrodes to prevent mixing of reactants.

A catalyst provides an alternative pathway with lower activation energy thereby making it possible for more particles to have the activation energy required to start a reaction and enhance the speed of the reactions occurring at the electrodes.

While generating energy, fuel cells give out H_2O as a by-product. Therefore, no pollutants are emitted into the air, as opposed to traditional methods that rely on combustion to produce electricity [2].

Unlike most batteries, fuel cells do not require electrical recharging. They rather require a constant supply of the fuel and O_2 [3].

2.2 Types of Fuel Cell

Fuel cells are classified according to the type kind of electrolyte they use, and these electrolytes determine the operational temperature of the fuel cell [7]. PEMFCs and AFCs are classified as the low temperature fuel cells. The phosphoric acid fuel cell (PAFC) employs medium temperature [8], while the molten carbonate fuel cell (MCFC) and the solid oxide fuel cell (SOFC) work with high temperatures. The SOFC and PEMFC use solid electrolytes while PAFC, AFC and MCFC employ liquid electrolytes [7,9].

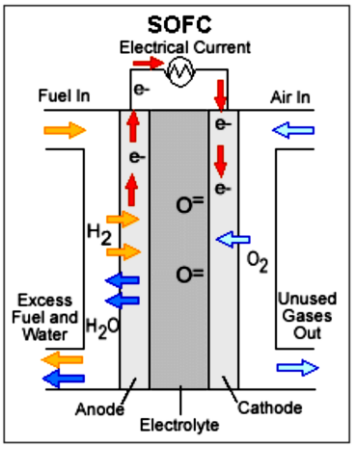
The different types of fuel cell all have slightly different principles of operation. However, they generally have fuel (hydrogen or alcohol) atoms entering the cell through the anode, where the atoms lose their electrons and are ionized. These electrons then flow between the electrodes through a wire (an external circuit), providing electric current to do work. The purity of the fuel used is important for the electrochemical energy conversion [10].

The different types of fuel cells all have their own advantages and disadvantages. The tables below (**Tables 2.1 and 2.2**) present different types of fuel cells, the electrolyte used, their operational temperature range, anode and cathode catalysts and half reactions [7].

2.2.1 Solid Oxide Fuel Cells (SOFC)

SOFCs are solid state devices, operating at temperatures up to 1000°C [11]. SOFCs consist of two electrodes, which are separated by a transition metal-based ceramic such as Zirconium oxide (ZrO_2), Y-stabilized ZrO_2 as electrolytes. By operating at high temperature, SOFCs can use different fuels such as hydrogen and other naturally occurring gases [12,13].

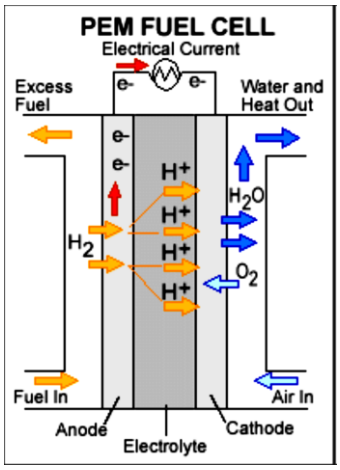
This type of fuel cell has electrical efficiency of up to 60% for stand-alone or 80% if heat and power are being co-generated. One drawback in the applications of SOFC is that the units are limited by the high temperature and they tend to be big and prone to fracture as a result of thermal stress and cycling [14,15].



Scheme 2.1: Solid Oxide Fuel Cell (SOFC) [16].

2.2.2 Proton Exchange Membrane (PEM) Fuel Cell

The PEMFC is simply FC that employs hydrogen as fuel in acidic medium. **Scheme 2.2** represent a typical hydrogen-oxygen PEMFC. PEMFCs are primarily made up of membrane electrode assemblies (MEA) which comprise of the catalyst, electrodes, and electrolyte. Hydrogen is oxidized at the anode, and electrons and protons are generated. This is shown in **Equation 2.1**.



Scheme 2.2: Schematic diagram of the PEMFC [16].

At the anode:

$$2H_2 \rightarrow 4H^+ + 4e^- \qquad \textbf{2.1}$$

The protons formed at the anode flow to the cathode through the PEM. The PEM is electrically insulating, and so the electrons cannot be transferred through it. They therefore get to the cathode through an external circuit, thereby generating electricity. The rate of reaction is measured by the current generated. While this is happening, O_2 (air) enters the cell through the cathode and is then reduced after reacting with the protons and electrons to produce H_2O (water). The half-cell reaction for the reduction of oxygen (ORR) is shown by equation 2.2.

$$O_2 + 4H^+ + 4e^- \rightarrow 2H_2O \qquad \textbf{2.2}$$

The overall reaction:

$$2H_2 + O_2 \rightarrow 2H_2O \qquad \textbf{2.3}$$

This process takes place in every type of fuel cell.

PEMFC are being explored for use in transport, stationary power generation and portable power [17] owing to their potential for high power density. The

polymer that serves as electrolyte membrane must be a separator that supports protons mobility and blocks electrons transport and have low impermeability to gases.

This membrane also plays an important part in PEMFC water management. Water is important during fuel cell operation because the electrolyte membrane requires some moisture to be proton conductive [10]. However, water blocks the flow of the reactants, thus hindering their access to the catalyst layer and leading to low performance of the cell [10,18]. So, excess level of water in the flow channel should be avoided.

Despite the challenges with water management, the PEMFC remains the most promising option among FCs because:

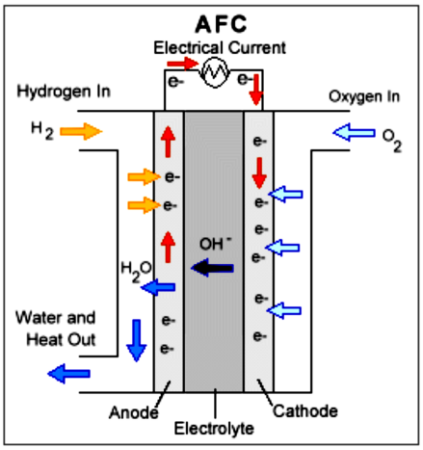
- They can operate at low temperatures (70 - 100°C) and so they can operate instantly without any residual time delays.
- They possess high power density ($\gg$ 100 mW/cm^2).
- There are zero emissions especially when they operate under pure hydrogen [19].

PEMFCs have electrical efficiency of about 50% when operating at temperatures between 60 and 100°C [20]. However, platinum, the most common catalyst for both the anode and cathode has one drawback, which is its high sensitivity to low levels of CO. And so, on exposure to 10 ppm CO concentration, the performance of the device degrades [21].

Fuels for PEMFCs include hydrogen and alcohol because protons are used as charge carriers through the membrane [22].

2.2.3 Alkaline Fuel Cells (AFC)

This is simply FC that employs hydrogen as fuel in alkaline medium. It has been around for a long time and has been used to power electrical space vehicles [23]. AFCs have power efficiencies of up to 60% [24,25]. They work with potassium hydroxide as electrolyte and operate between 60 and 90°C. They employ precious metal at the anode while using platinum or lithiated NiO at the cathode. **Scheme 2.3** shows the working of the AFC [26].



Scheme 2.3: Alkaline Fuel Cells (AFC) [16].

Oxidation of hydrogen occurs at the anode, following **Equation 2.4**:

$$2H_2 + 4OH^- \rightarrow 4H_2O + 4e^- \qquad \textbf{2.4}$$

The electrons flow to the cathode and oxygen is reduced according to **Equation 2.5:**

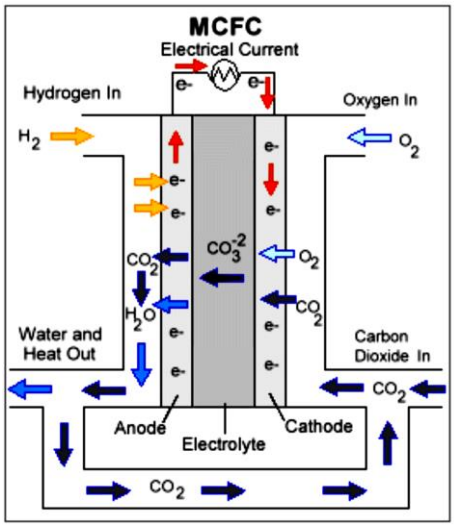
$$O_2 + 2H_2O + 4e^- \rightarrow 4OH^- \qquad \textbf{2.5}$$

Overall reaction:

$$2H_2 + O_2 \rightarrow 2H_2O \qquad \textbf{2.6}$$

2.2.4 Molten Carbonate Fuel Cells (MCFCs)

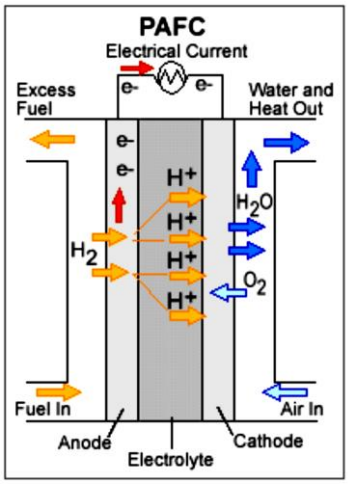
MCFCs operate at temperatures around 650°C with efficiency of up to 60%. The electrolyte used here is molten carbonate salt, which usually contains a mixture of potassium and lithium, or lithium and sodium carbonates, which are kept in a ceramic matrix of $LiAlO_2$ [27-29].



Scheme 2.4: Molten Carbonate Fuel Cells (MCFC) [16].

2.2.5 Phosphoric Acid Fuel Cells (PAFC)

The PAFC is also a high temperature (about 200°C) fuel cell. Its electrolyte is phosphoric acid. PAFCs have electrical efficiency between 40 and 45% but can be up to 80% if the discarded heat is recycled in a co - generation scheme [30,31]. The operation of the PAFC is illustrated in Scheme 2.5.



Scheme 2.5: Phosphoric Acid Fuel Cells (PAFC) [16].

Table 2.1: The different fuel cells and their properties [7].

Fuel Cell	Electrolyte	Operating Temperature	Charge Carrier	Anode Catalyst	Cathode Catalyst	Electrical Efficiency (%)	Fuel Sources
Solid Oxide (SOFC)	Zirconium oxide	650- 1000	O^{2-}	Nickel/ Zirconium oxide	Strontium doped Lanthanum Manganite	50- 60	H_2, CO, Natural gas
Polymer Electrolyte Membrane (PEMFC)	Sulphonated Organic Polymer (hydrated during operation)	70- 100	H^+	Platinum (Pt)	Platinum (Pt)	40- 45	H_2 Reformate with less than 10ppm of CO
Alkaline (AFC)	Aqueous Potassium Hydroxide (30-40%)	60- 90	OH^-	Nickel (Ni) or precious metal	Platinum (Pt) or lithiated NiO	60	H_2 Removal of CO_2 from both gas streams
Molten Carbonate (MCFC)	Solution of Lithium/Sodium/Potassium Carbonate	600- 700	$CO3^{2-}$	Nickel/Chromium Oxide	Nickel Oxide (NiO)	50- 60	H_2, CO, Natural gas
Phosphoric Acid (PAFC)	Phosphoric acid	150- 220	H^+	Platinum (Pt)	Platinum (Pt)	40-45	H_2 Reformate

Table 2.2: Electrochemical reactions of the different fuel cell types [7].

Fuel Cell	Fuel to Anode	Fuel to Cathode	Anode Half Reaction	Cathode Half Reaction	Overall Reaction of The Cell
Solid Oxide (SOFC)	H_2 in hydrocarbon fuel	O_2	$H_2 + O_2\text{-} \rightarrow H_2O + 2e^-$	$½\ O_2 + 2e^- \rightarrow O^{2-}$	$H_2 + ½\ O_2 \rightarrow H_2O$
Polymer Electrolyte Membrane (PEMFC)	H_2	O_2	$H_2 \rightarrow 2H^+ + 2e^-$	$½\ O_2 + 2H^+ + 2e^- \rightarrow H_2O$	$H_2 + ½\ O2 \rightarrow H_2O$
Alkaline (AFC)	H_2	O_2	$2H_2 + 4OH^- \rightarrow 4H_2O + 4e^-$	$O_2 + 2H_2O + 4e^- \rightarrow 4OH^-$	$2H_2 + O_2 \rightarrow 2H_2O$
Molten Carbonate (MCFC)	H_2 in hydrocarbon fuel	O_2	$H_2 + CO_3^{2-} \rightarrow H_2O + CO_2 + 2e^-$	$½\ O_2 + CO_2 + 2e^- \rightarrow CO_3^{2-}$	$H_2 + ½O_2 + CO_2 \rightarrow H_2O + CO_2$
Phosphoric Acid (PAFC)	H_2	O_2	$H_2 \rightarrow 2H^+ + 2e^-$	$½\ O_2 + 2H^+ + 2e^- \rightarrow H_2O$	$H_2 + ½\ O_2 \rightarrow H_2O$

2.3 Fundamental Electrochemical Reactions for Fuel cells

All fuel cells have similar fundamental structure, consisting of two electrodes (cathode and anode), and operate with an electrolyte (which separates the anode and cathode and transports the protons) and connected through an external circuit (which transports the electrons).

2.3.1 Cathode Reaction: Oxygen Reduction Reaction (ORR)

ORR is the reaction that occurs at the cathode. In aqueous solutions, it can follow any of two pathways: (i) the direct 4-electron reduction pathway from O_2 to H_2O (preferable for fuel cells), or (ii) the 2-electron reduction pathway from O_2 to H_2O_2 (preferable in industry) and then from H_2O_2 to H_2O. In non-aqueous aprotic solvents or alkaline solutions, the ORR can also follow the 1-electron reduction pathway from O_2 to O_2^- (superoxide) (used to explore the ORR mechanism) [98].

The ORR kinetics is usually slow and requires a cathode ORR catalyst to enhance the ORR kinetics.

Table 2.3. Thermodynamic electrode potentials ORR reactions [96, 97].

Electrolyte	ORR reactions	Thermodynamic electrode potential at standard conditions, V
Acidic aqueous solution	$O_2 + 4H^+ + 4e^- \rightarrow H_2O$	1.229
	$O_2 + 2H^+ + 2e^- \rightarrow H_2O_2$	0.70
	$H_2O_2 + 2H^+ + 2e^- \rightarrow 2H_2O$	1.76
Alkaline aqueous solution	$O_2 + H_2O + 4e^- \rightarrow 4OH^-$	0.401
	$O_2 + H_2O + 2e^- \rightarrow HO_2^- + OH^-$	–0.065
	$HO_2^- + H_2O + 2e^- \rightarrow 3OH^-$	0.867
Non-aqueous aprotic solvents	$O_2 + e^- \rightarrow O_2^-$	a
	$O_2^- + e^- \rightarrow O_2^{2-}$	b

The solvent in use would determine the thermodynamic potentials for the 1-electron reduction reaction pathway to a superoxide (O_2^-), and its further reduction to O_2^{2-} (peroxide). Therefore, they are not listed in **Table 2.3**.

2.3.2 Anode Reaction: Hydrogen Oxidation Reaction

The global renewable energy demands and the efforts to replace fossil fuel makes it important to develop cleaner and environmentally friendly sources of power for future sustainable energy technology. H_2 fuel is produced from H_2O. It is a clean gas of high purity. Its specific energy is also high (141.86 MJ kg^{-1}) [99–101].

The AMFCs operate in alkaline conditions (unlike the common PEMFCs that operate in acidic conditions), and are attracting great attention, due to such impressive properties as: (i) improved cathodic reaction (ORR) kinetics [102]; reduced corrosion of the Pt catalyst [103]; better management of H_2O flooding and the possibility of using nonprecious metals as electrocatalysts [104,105].

Despite these advantages, the anodic reaction (HOR) is a challenge with AMFCs because of the low dissolution of protons in alkaline conditions or high pH and decreased HOR activity, requiring high overpotential [106,107]. From previous research the kinetics of the HOR is relatively lower to an order of two magnitudes in AMFCs than in PEMFCs [108], even with a high loading of the common Pt electrocatalyst [109].

Pd-based electrocatalysts have recently been reported to show high performance for AMFCs, compared to the Pt-based electrocatalyst. This informed the choice of electrocatalysts used in this work.

As a strategy to reduce the cost of production of AMFCs, Pd nanocatalysts are usually supported on carbon materials. The carbon supports used in this work are carbon black (CB) and onion-like carbon (OLC). Addition of metal oxides (CeO_2) to the nanostructured Pd has been found to enhance electrocatalytic performances of Pd-based electrocatalysts.

2.3.3 Anode Reaction: Alcohol Oxidation Reaction

In fuel cells that use alcohol (ethanol, methanol, 2-propanol etc.) instead of hydrogen, alcohol is oxidized at the anode. And as in hydrogen oxidation, the alcohol is oxidized at the anode, producing electrons (e^-) which flow through the connecting wires (external circuit) to the cathode. The protons (H^+) get to the cathode through the electrolyte membrane.

All the reactions require a catalyst to decrease the reaction barrier and platinum (Pt) is presently the most commonly used catalyst. However, the high cost of using Pt-based catalysts to make fuel cells that are commercially available has prompted research on the use of alternative catalysts, including non-precious metals [95], carbon materials and alloys.

2.3 Direct Alcohol Fuel Cell (DAFC)

The DAFC uses an acidic electrolyte and employs alcohols as fuel. It comprises of two electrodes that are separated by a PEM. All these are collectively called the membrane electrode assembly (MEA) [4].

DAFCs are PEMFCs which use alcohol as the fuel in place of hydrogen and are used to power mobile and portable devices.

2.4 Alkaline Direct Alcohol Fuel Cells (ADAFCs)

ADAFCs are simply FCs that use alcohol as fuel in alkaline medium. The alkaline direct ethanol fuel cell (ADEFCs) and alkaline direct methanol fuel cells (ADMFCs) are examples of these ADAFCs.

2.4.1 Background of the Alkaline Direct Ethanol Fuel Cell (ADEFC)

The ADEFC is an ADAFC that uses ethanol as fuel. Amongst the fuels used in fuel cell technologies, ethanol is becoming more attractive due to its low toxicity, renewability, environmental friendliness, high theoretical energy density of 8 kWh^{-1} kg (gasoline has energy density of 12 kWh^{-1} kg) and ease of large-scale production [1].

The ADEFC was first designed and fabricated about two decades ago. It was used to power Schluckspecht vehicle with output voltage in the range of 20 to 45 V [32]. This was an idea created by a team of researchers at the University of Applied Sciences, Offenburg. Afterwards, different prototypes of the ADEFCS were designed and built for mobile phone charging and electrical appliances [33,34].

2.4.2 Working Principle of Alkaline Direct Ethanol Fuel Cell

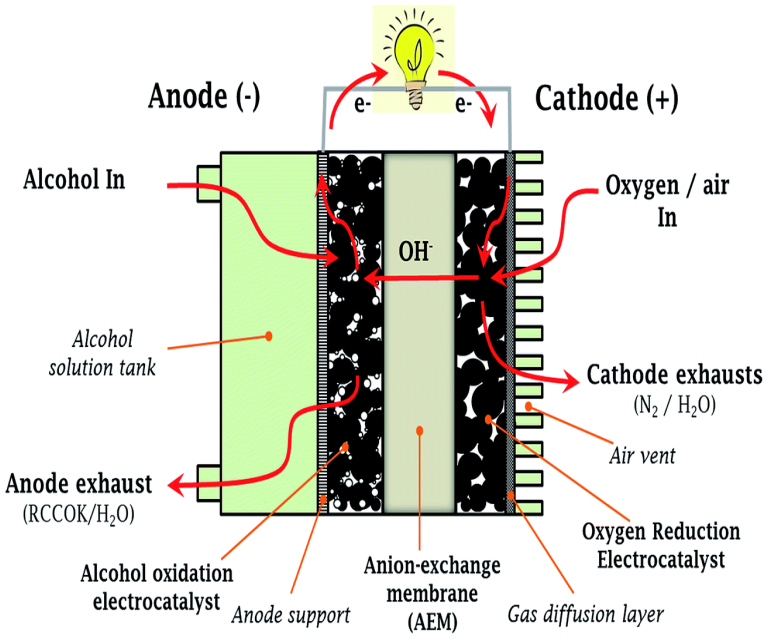
ADEFCs commonly use two Pt electrodes (cathode and anode). Instead of employing the Nafion® MEA as used in the conventional PEMFCs, both electrodes of an ADEFC are separated by an anion-exchange membrane (AEM) [35,36] as illustrated in **Scheme 2.6** [1].

The operation of the ADEFCs follows simple reaction mechanisms at the electrodes and electrolyte media: at the anode, a certain volume of ethanol is oxidized (ethanol oxidation reaction (EOR)) to generate protons (H^+s) and electrons (e^-s), as well as various by-products, mostly acetic acid, as represented in **Equation 2.7 – 2.9**.

The cleaving of C-C bonds requires so much energy thereby obstructing the complete oxidation of ethanol to CO_2 (**Equation 2.7**), while the RDS of the reaction is the production of acetic acid (**Equation 2.9**), because of the abundance of OH^- ions in alkaline conditions.

The protons and electrons at the anode get to the cathode through the AEM and external circuit, respectively. At the cathode, they react with O_2, which is then reduced (ORR) and water is produced. This reaction can occur either directly or serially to produce as given in **Equation 2.10 – 2.12**. The movement of the electrons from the anode to the cathode generate electricity.

The oxidation of ethanol is of major concern in the development of the ADEFC because it is relatively sluggish thereby requiring high loading of noble metal electrocatalysts contributing to the huge cost of fabricating the device.



Scheme 2.6: Alkaline Direct Ethanol Fuel Cell Operation Scheme [1].

Anodic reactions

(Total oxidation pathway)

$CH_3CH_2OH \longrightarrow CO_2 + 12e^- + 12H^+$ **2.7**

(Partial oxidation pathways)

$CH_3CH_2OH \longrightarrow CH_3CHO + 2e^- + 12H^+$ **2.8**

$CH_3CH_2OH \longrightarrow CH_3COOH + 4e^- + 4H^+$ **2.9**

Cathodic reactions

(Direct pathway)

$O_2 + 4e^- + 4H^+ \longrightarrow 2H_2O$ $E^o = 1.230$ V **2.10**

(Series pathways)

$O_2 + 2e^- + 2H^+ \longrightarrow H_2O_2$ $E^o = 0.695$ V **2.11**

$H_2O_2 + 2e^- + 2H^+ \longrightarrow 2H_2O$ $E^o = 0.695$ V **2.12**

2.5 Nanostructured Palladium-based Electrocatalysts

The commercially available FC devices are too expensive and that could be traced to the use of bulk platinum (Pt) electrocatalysts to drive the reactions in acidic conditions. The reaction at the cathode is of major concern in fuel cell devices, as it is extremely sluggish and necessitated the use of high loadings of Pt electrocatalysts [38] as opposed to the anodic reaction, which is about five times faster than the reaction at the cathode, with very little loading of Pt [39]. Moreover, the Pt electrocatalyst is rarely readily available due to scarcity. Nanotechnology is one strategy that has been employed to minimize the cost of the Pt electrocatalyst and MEA for the fabrication of FC devices [40–42]. Nanotechnology has brought about research ideas to reduce the loading of Pt electrocatalysts (*ca.* 20 %). The use of various carbon supports has been reported [43–77].

Another strategy that has been employed in FC technologies is a replacement of the acidic media of operation with alkaline media [37] as electrocatalysts have shown great performance in alkaline media due to the impressive characteristics of alkaline media. Therefore, it became the interest of this project to explore Pd-based materials in alkaline conditions for the electrochemical conversion applications: ADEFC and AMFC devices.

2.5.1 Methods for the Preparation and Deposition of Nanostructured Materials

Different methods have been explored in the preparation and deposition of nanostructured materials. The most common amongst these methods are

electrochemical deposition (ECD), atomic layer deposition (ALD), sol-gel, spray pyrolysis, and solvothermal/hydrothermal processes and microwave-assisted, explained below:

2.5.1.1 Atomic Layer Deposition Method

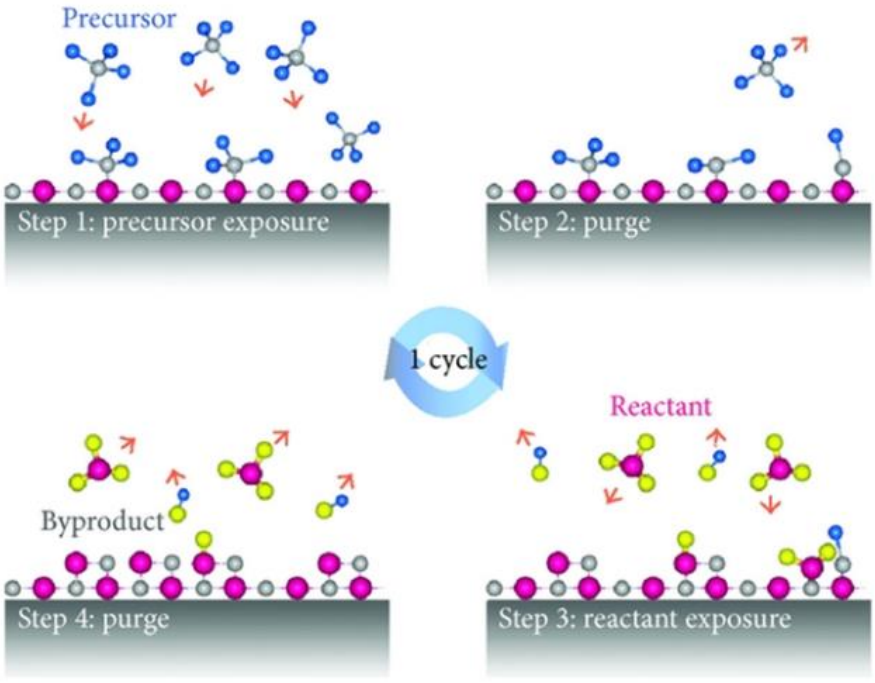
ALD is a method where the chemical species are exposed in a layer-by-layer manner leading to the growth of self-imposed film. There are four important steps required in this process, which are represented in **Scheme 2.7**. These are:

- Exposure of metal precursors.
- The metal precursors, intermediates and by-products are eliminated and purged from the chamber.
- The exposed metal precursor is then reduced with hetero atoms like O, N.
- The precursor materials and by-products molecules are subsequently eliminated or purged from the chamber.

The first stage involves linkage of electron-rich hetero-atom species to the metal precursors. This would surely reduce additional adsorption of the metal precursor when the adsorption sites on the monolayer coverage are passivated or saturated. There are some benefits associated with ALD for the preparation and deposition of nanostructured materials: (i) the sequential and self-limiting surface reaction process of the ALD results in very good step coverage and conformal deposition on high aspect ratio structure [48]; (ii) obtaining high-quality materials at low processing temperature; (iii) excellent reproduction and production of multilayer nanostructured materials in a continuous process; and (iv) possibility of interface modification is allowed because it tends to produce sharp interfaces and superlattices.

However, it has the following limitations: (i) lack of speed which causes only a small fraction of the crystal to be deposited in a single cycle. It is also not economical as some multi-component species cannot be grown or deposited by the ALD (ii) the

size of the reaction chamber restricts the chemical residues from the precursors to the chamber.



Scheme 2.7: Schematic illustration of ALD Method [49].

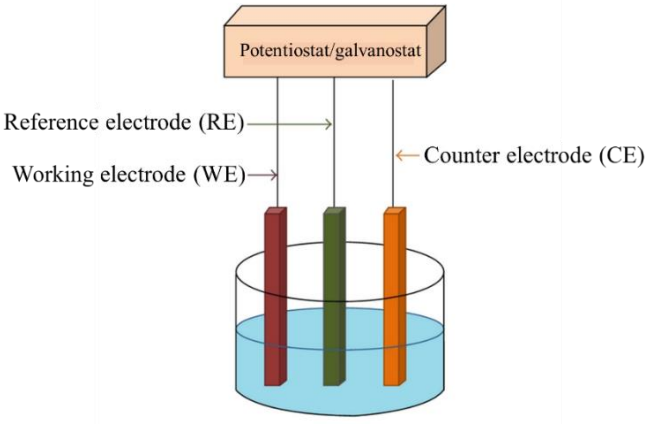
2.5.1.2 Electrochemical Deposition (ECD) Method

The ECD is a method of reducing metal precursors or ions from organic, aqueous, and fused-salt solutions. This is expressed in **Equation 2.13** and illustrated in **Scheme 2.8**.

$$M^{n+}_{solution} + ne^- \longrightarrow M_{lattice} \qquad \textbf{2.13}$$

The ECD process could be achieved using two different methods [50]: (i) an electrodeposition method, which involves using an external power supply to produce electrons; and (ii) an electrodeless deposition method involving a reducing agent in solution as electrons source. The ECD method is employed in this research, as it is one of the simplest and most effective strategies for nanostructured fabrication. It

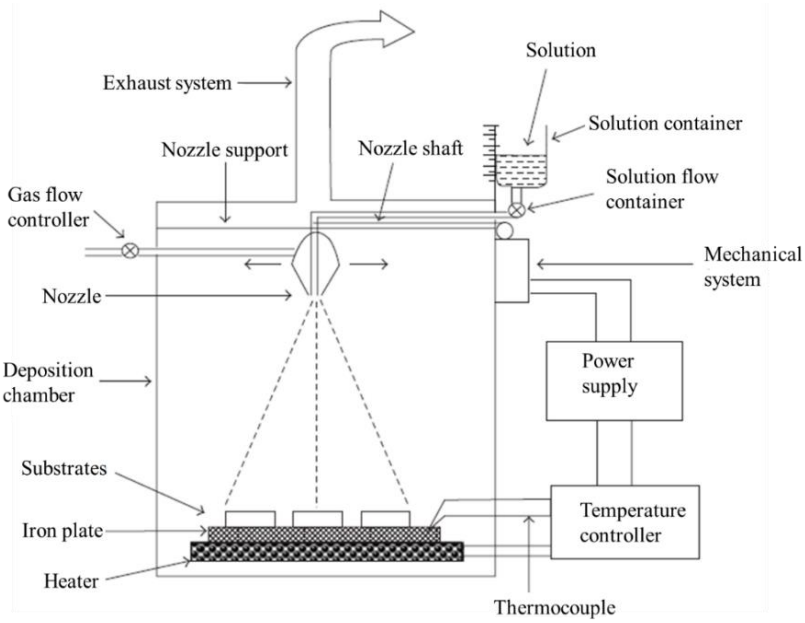
has a tendency to modify and control the morphology and composition of the nanostructured materials.



Scheme 2.8: Schematic illustration of the ECD system [51].

2.5.1.3 Spray Pyrolysis Method

Spray pyrolysis method involves the spraying of a precursor solution onto a heated glass substrate and depositing a processed film onto it by a process called pyrosol technique. In the spray pyrolysis method, the precursor solution is atomized like little droplets of the solution, and then vaporized and sprayed on a substrate, leading to the formation of a dried thermally decomposed precipitate [52], as illustrated in **Scheme 2.9**.

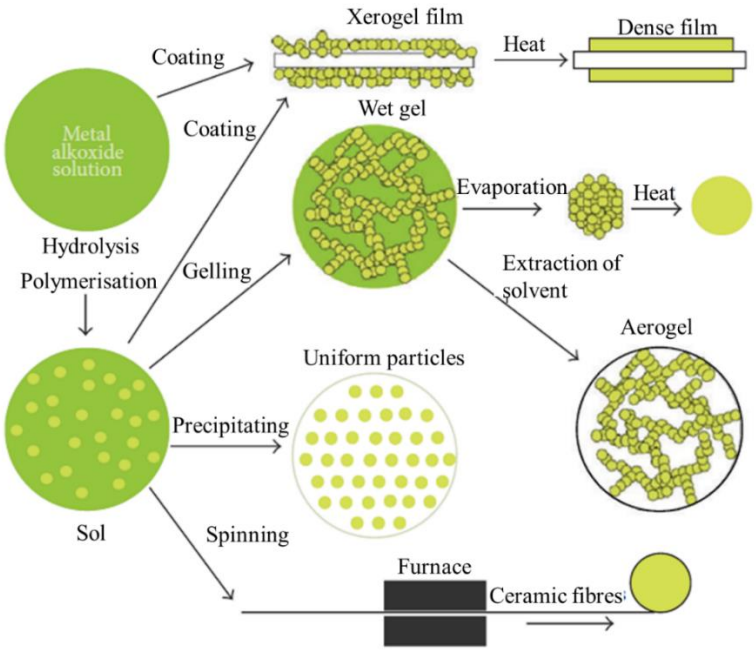


Scheme 2.9: A representation of the spray pyrolysis method [53].

The spray pyrolysis method is dependent on some variables: temperature, temperature gradient, solute concentration, processing time, atomization process, and carrier gases. These factors could influence the expected product. The spray pyrolysis technique has the following characteristics: low cost, no ultra-high vacuum (UHV) system required, the chemical transformation occurs within micron to nano-sized liquid droplets.

2.5.1.4 Sol-Gel Coating Method

This is a wet chemistry method employed in preparing nanostructured materials from a chemical solution with a gel (an integrated network) of precursors for discrete nanoparticles or polymer networks. Metal chlorides and alkoxides are examples of the most used precursors and they can easily undergo many hydrolysis and/or polycondensation reactions [54], as the case may be. A sol-gel is represented in **Scheme 2.10**. The sol-gel is seen as a bridge for preparing nanostructured material because the sol gravitates towards a gel-like diphasic system of liquid and solid, with morphologies that range from discrete particles to a continuous network of polymers.



Scheme 2.10: Schematic illustration of the sol-gel method [55].

2.5.1.5 Hydrothermal/Solvothermal Synthesis Method

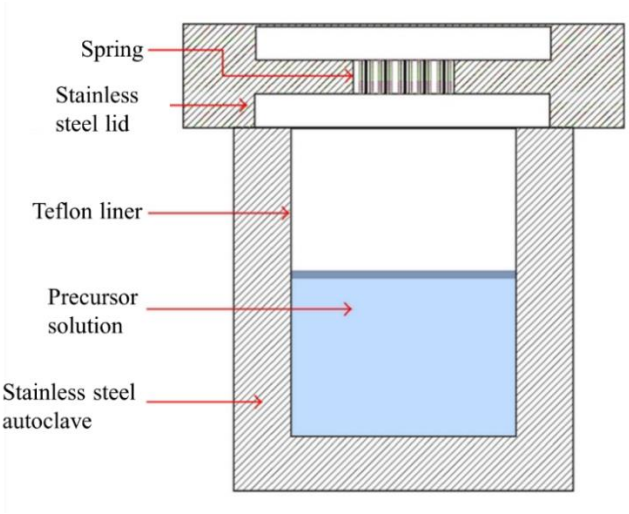
These methods are effective for the systematic and morphologically controlled synthesis of nanostructured materials, performed in a tightly sealed Teflon container and heated to a temperature that exceeds the boiling point of the (non-aqueous or aqueous) solvent and abruptly increased the autogenous pressures [56]. This is illustrated in **Scheme 2.11**. When the solvent used is aqueous, the process is called hydrothermal, while for non-aqueous solvents it is called solvothermal. The solubility and reactivity of the reagents in the hydrothermal/solvothermal process, are elevated when the temperature and pressure are increased, resulting in expected products [57]. The hydrothermal/solvothermal process is commonly employed to control the morphology of well-defined nanostructured materials such as nanostructured Pd supported on carbon.

There are three very important experimental parameters in the hydrothermal/solvothermal process. These are: solvents properties, capping agents and reaction temperature.

- ***Solvents properties*:** The solvothermal process could be influenced by the properties of the solvents such as dielectric constant, polarity and viscosity. The way the solvent interacts with the precursor reagents, intermediates, and final products can affect the reaction kinetics, equilibrium, as well as the expected products. Polar solvents such as H_2O, ethylene glycol (EG), dimethylformamide (DMF), are usually preferred due to their compatibility with most solutes or reagents.
- ***Capping Agents*:** During the preparation of nanostructured materials, facet-specific capping agents are usually applied to aid exposure of their desired facet, thereby enhancing the properties of the products expected from the hydrothermal/solvothermal process. Some common capping agents are acids, solvents, surfactants, polymers.
- ***Reaction Temperature*:** The reaction temperature during the solvothermal/hydrothermal process hugely affects the properties of the expected products. The reaction temperature could vary depending on certain properties of the solvent such as dielectric constant and viscosity. Aqueous solvent could be more active at high temperatures, while organic solvents are usually active at low temperatures. The solubility of solutes in solvents also tend to increase at higher temperature.

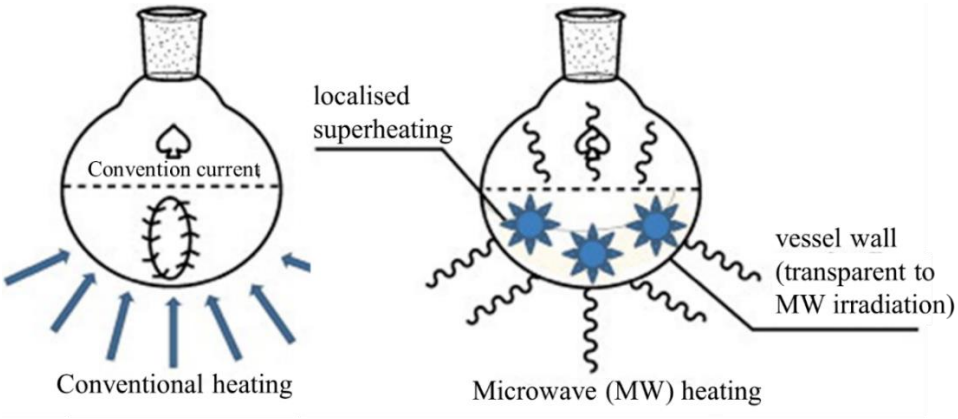
Some advantages of the solvothermal/hydrothermal process are: (i) it increases the solubility of the materials because heat and pressure are applied in the set-up to its critical point; (ii) it greatly improves the chemical activities of the precursors; (iii) ease of production of novel compounds that have characteristic metastable state and specific phase; and (v) substances that have low melting point and high vapour pressure are obtained. However, this method has a few drawbacks such as (i) the need to use expensive autoclave reactor; (ii) the usage of high temperature and

pressure during chemical reactions giving rise to safety issues; (iii) reactions usually take long hours (12 hours or more); and (iv) impossible to notice reaction intermediates [58,59]. Due to the drawbacks of the autoclave, the use of microwave as a viable substitute during solvothermal/ hydrothermal processes is required as microwave-assisted processes are uniform and rapid [60–62].



Scheme 2.11: An illustration of the hydrothermal/solvothermal processes [63].

The microwave-assisted synthesis method (**Scheme 2.12)** operates by aligning dipoles of the precursor materials with an external field via excitation, which is produced by microwave electromagnetic irradiation. The microwave-assisted heating progresses from inward to outward uniformly unlike the conventional autoclave heating process, which progresses from outward to inward.



Scheme 2.12: Comparing the conventional heating process to the microwave-assisted heating [65].

2.6 Electrochemical Techniques

Electrochemistry is one powerful tool that is useful in probing reactions related to electron transfers. Electrochemistry is concerned with the flow of electrons in response to chemical changes, which is the reduction or oxidation of a metal complex [66].

An “electrolyte solution” is prepared by dissolving the supporting electrolyte (an acid or a salt) in a solvent (which is usually water) to minimize the solution resistance.

The concentration of the dissolved salt determines how conductive the electrolyte solution will be. A higher concentration of the supporting electrolyte means a higher proton conductivity.

A good supporting electrolyte has high solubility in the solvent and is inert in the conditions of the experiment. A good solvent is one which is liquid at the applied experimental temperatures, and which completely dissolves the analyte as well as

high concentrations of the supporting electrolyte. It also does not trigger unwanted reactions. [66]

The analyte gets to the surface electrode by these three means of mass transport:

- **Convection**, which is due to mechanical influence such as vibration or stirring.
- **Migration** - If the movement of an ionic solute is caused by the action of an electric field (negative electrodes attract positive ions).
- **Diffusion**, which occurs when there is a concentration gradient of the analyte in the electrochemical cell, such that the analyte moves from higher concentration areas to areas of lower concentration.

To minimize the occurrence of convection, stirring or vibrations are avoided. Migration is reduced by using an electrolyte of high concentration (when compared to the analyte concentration) [67].

2.6.1 Electrodes and Preparation for Use

A three-electrode (also called a half-cell) system is made up of a working electrode (WE), a counter electrode (CE), and a reference electrode (RE). It is the typical setup for common electrochemical experiments like cyclic voltammetry (CV), electrochemical impedance spectroscopy (EIS) and linear sweep voltammetry (LSV). As current flows between the WE and CE, the RE measures the applied potential (E_{app}) with respect to a stable reference reaction.

2.6.1.1 The Working Electrode (WE)

The electrochemical reaction of interest occurs at the WE. Therefore, the electrode's surface must be cleaned properly, and the electrode's surface area precisely measured. The experiment of interest determines what working electrode is used. Different electrode materials vary in their electrochemical responses. For instance,

electron transfer kinetics differ from one electrode type to another; adsorption also occurs strongly on certain electrode material. One good start towards checking for these issues is by first changing the electrode material [68].

The WE must be cleaned (polished) before measurements and the method of polishing the electrode depends on the type of electrode. The GCE or platinum electrode can be cleaned by mechanical polishing and sonicating in ultrapure water to remove particles [69]. To clean remove any left-over adsorbed species, several CV scans should also be performed across a wide potential window in a simple electrolyte [70].

The surface of glassy carbon electrodes gets very reactive once it is activated by polishing and any impurity in the solvent will easily finds its way to the carbon surface of the electrode and alter the voltammograms. The adsorption of these impurities on the electrode can be avoided by treating the solvent with activated carbon [69].

2.6.1.2 Reference Electrode (RE)

The potential of the WE is measured with respect to a reference point using a RE. A potentiostat measures the E_{app} of the WE *vs.* the potential of the RE. Some reference electrodes that are commonly used in aqueous electrolyte are the (Ag|AgCl) electrode, standard hydrogen electrode (SHE) and the standard calomel electrode (SCE).

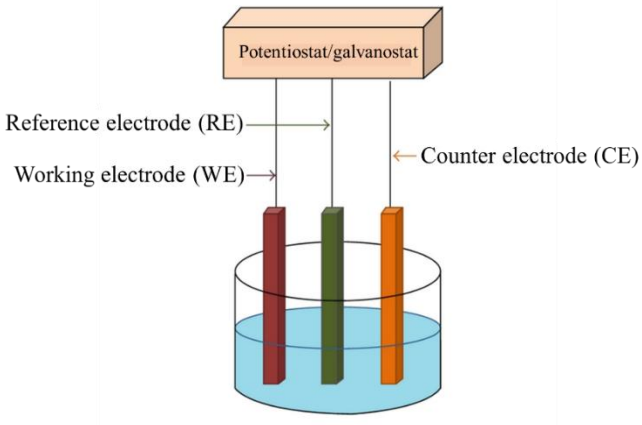
2.6.1.3 Counter Electrode (CE)

At the CE a reaction occurs opposite to that happening at the WE. For instance, when studying an oxidation at the WE, the reaction at the CE would be a reduction. This happens to complete the electrical circuit. The surface area of the CE is greater than the surface area of the WE so that the reaction occurring at the CE does not interfere with /inhibit the reaction at the WE. A platinum wire is commonly used as a CE. But there are others [71].

2.6.2 Cyclic Voltammetry (CV)

This is a standard technique used for determining the redox potential windows for an electroactive species in electrochemistry, and energy conversion and storage devices [72]. It is a direct current (DC) electrochemical technique commonly used for situ measurements of the electrocatalytic properties of various materials in the solid state (as thin films deposited on an electrode) or in solution. CV is used to have a picture the general behaviour of a catalyst material and uses a potentiostat and a three-electrode setup (**Scheme 2.13**).

To perform CV, a potential is applied to a working electrode (WE) at a fixed scan rate (dV/dt). This potential is then swept linearly back and forth through one or more cycles (depending on the required information). The current response obtained is then recorded and plotted against the applied potential [73-76]. The oxidized or reduced molecules leave the surface of the WE and other molecules move to the surface of the WE. As electrons keep flowing to or away from the electrode, current is produced. The current produced is a measure of the electron-transfer happening at the electrode-electrolyte interface.



Scheme 2.13: Schematic representation of a three-electrode electrochemical setup [51].

The CV technique is often used to get information on the presence of intermediates in the redox processes, the reaction reversibility, the electron stoichiometry, diffusion coefficient of the analyte and reduction potential to identify the analyte, and to deduce the analyte's concentration by Nernst's equation (**Equation 2.14a**). The concentration of the unknown analyte is obtained from the calibration curve of current against concentration. The thermodynamics of the reaction is explained by equation **2.14a** and **2.14b**.

$$E^0 = \frac{RT}{zF}\ln\frac{[\text{Anode}]}{[\text{Cathode}]} = 2.303\frac{RT}{zF}\log_{10}\frac{[\text{Anode}]}{[\text{Cathode}]} \qquad \textbf{2.14a}$$

$$E_{1/2} = \frac{E_{pa} + E_{pc}}{2} \qquad \textbf{2.14b}$$

$$\Delta E_p = |E_{pa}| - |E_{pc}| \qquad \textbf{2.15}$$

where E^0 is the overall potential (V), $E_{1/2}$ is the half-wave potential, ΔE_p is the peak-to-peak separation, R is the universal gas constant (8.314 JK^{-1} mol^{-1}), T is absolute temperature (K), F is Faraday's constant (96485 C mol^{-1}), z is the ionic charge across a membrane, E_{pa} is the peak anodic potential (V), E_{pc} is the peak cathodic potential (V), $i_{pa,}$ is the peak anodic current (A) and i_{pc} is the peak cathodic current.

A typical cyclic voltammogram of bare GCE (glassy carbon electrode) in $Fe(CN)_6^{4}/Fe(CN)_6^{3-}$ in KCl (standard redox electrolyte) is shown in **Figure 2.1**.

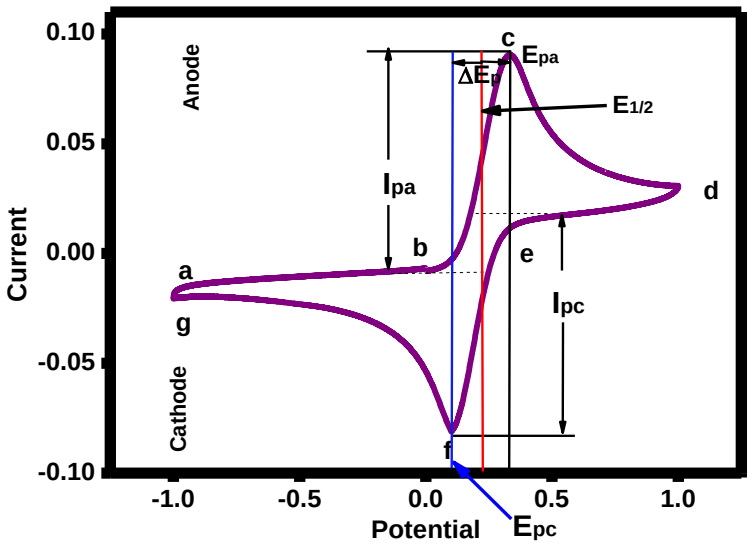


Figure 2.1: Cyclic voltammogram of a single electron redox reaction.

$$M^+ + e^- \rightleftharpoons \mathrm{M} \qquad \textbf{2.16}$$

In a reversible reaction such as the one above, the potential is scanned positively from (a) to (d), giving rise to anodic current (I_{pa}) and resulting in oxidation. The peak current occurring at (c) is called the anodic peak potential (E_{pa}) and is reached after complete oxidation of all of the substrate at the surface of the electrode.

When the switching potential is reached at (d), the potential scans negatively from (d) to (g), giving rise to cathodic peak current (I_{pc}) and causing a reduction.

At point (d), the current is very positive, but then it is swept lower values. At (e) current starts flowing as the voltage reaches a point that allows reduction to occur. At point (f), all the electroactive species at the surface of the electrode have been reduced and a peak (cathodic peak) is formed at the potential at (f). The potential at which the cathodic peak is formed is called the cathodic peak potential (E_{pc}).

The electrode potential E is given by:

$$E = E_i + \nu t \qquad \textbf{2.17a}$$

Where E*i* is the initial potential (V), *v* is the sweep rate (V/s or mV/s) and t is the time (s)

When the potential sweep switches direction, the equation becomes:

$$E = Es - vt \qquad \textbf{2.17b}$$

where E*s* is the switching potential.

For a reversible electrochemical reaction,

- $I_{pa} = I_{pc}$
- The peak potentials E_{pa} and E_{pc} are not influenced by the scan rate v.
- $E_{1/2}$ is positioned halfway between E_{pa} and E_{pc}.
  Therefore, $E_{1/2} = (E_{pa}+E_{pc})/2$.
- I_p is proportional to $v^{1/2}$.
- The separation between E_{pa} and E_{pc} is 59 mV/n for an n-electron couple (n = number of electrons).

If a redox couple fails to fulfil one or more of the above criteria, it is almost certainly not reversible [77].

2.6.3 Electrochemical Impedance Spectroscopy (EIS)

EIS is used to monitor the ionic resistance in a material and to determine both the real impedance (resistance) from the imaginary impedance (capacitance) of a fuel cell. Electrochemical impedance is the study of the overall opposition to current flow in a circuit. Electrochemical impedance is like resistance, but it makes it possible to describe complex circuits that exhibit nonlinear current–voltage relationships (for example, circuits that exhibit inductance, capacitance, or mass diffusion). EIS correlates the different theoretical circuit elements to the actual electrochemical

processes taking place in an electrochemical system, thereby making it possible to fit the frequency, current and voltage data to equivalent circuit models [78-80].

The EIS is carried out either at a fixed potential or at a fixed current, hence its classifications into two: (i) potentiostatic electrochemical impedance spectroscopy (PEIS), which is EIS performed at a fixed potential (OCV, $E_{1/2}$ or biased potential); (ii) galvanostatic electrochemical impedance spectroscopy (GEIS) which is EIS performed at fixed current. Both classes of the EIS are important techniques that allow for the separation of (ionic and electronic) processes, occurring on different timescales, thereby making it easy to probe the diffusion of ions at the electrode-electrolyte interface [81].

The PEIS is employed in this research. EIS parameters such as bulk resistance (R_b), solution resistance (R_s), interfacial resistance (R_{int}), charge transfer resistance (R_{ct}), capacitive (dielectric) or constant phase element (*CPE*) and inductive and diffusive (Warburg, Z_w) properties can be obtained from the EIS signal (the Nyquist plot) by modeling it with the appropriate Voigt electrical equivalent circuit (*EEC).* The information extracted from the circuit helps to explain the reactions that are occuring at the electrode-electrolyte interface [82].

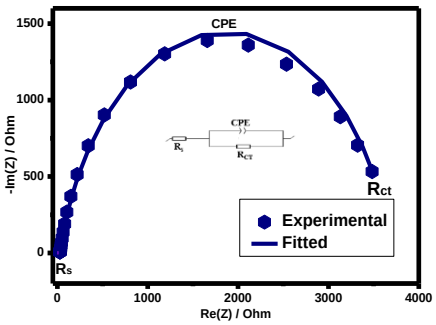
Major EIS parameters are: (i) solution resistance (R_s), which is the resistance of the solution between the WE and RE. When the R_s value is low, it means that the ions migrate with ease within the components of the electrochemical set-up and; (ii) interfacial resistance (R_{int}), which is the Voigt resistive element due to ohmic loss caused by the diffusion of ions of the supporting electrolyte between the electrodes the specific conductance of the electrolytes, the distance between the electrodes, and the WE area; (iii) charge transfer resistance (R_{ct}) which is opposition to the movement of electrons between the electrodes and supporting electrolyte. The smaller the Rct value, the better the electrode; (iv) double-layer capacitance (C_{dl}) which is characteristic of the electrical double-layer at the electrode/electrolyte

interfaces. It explains the tendency of the electrocatalyst to homogeneously and regularly store charge. If a perfect semi-circle is formed from the spectra, C_{dl} is used to define the charge storage system, but if a deformed semi-circle is formed from the spectra, interfacial capacitance (constant phase element, *CPE*) is used. A deformed semi-circle is usually an evidence of inhomogeneity or irregularities at the electrode surfaces. The deviation of the *CPE* (Z_{CPE}) from the C_{dl} is defined according to **Equation 2.18** (the power-law relationship) [83–87]:

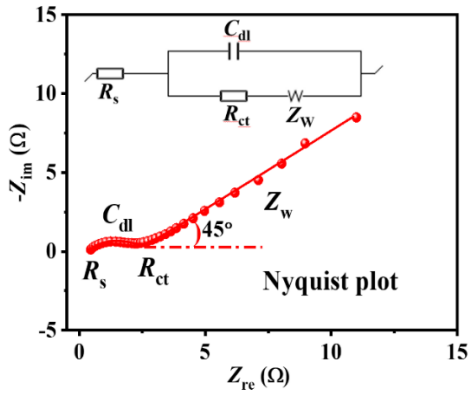
$$Z_{CPE} = [Q\ (j\omega)^{a}]^{-1} \qquad \textbf{2.18}$$

where Q is the non-ideal capacitance of the electrode-electrolyte interface, ω is the radial frequency, and *a* is the ideality factor with values ranging from -1 to +1. The Z_{CPE} is a pure inductor if *a* = -1. It is a pure resistor if a = 0. If *a* = 1, then it is a pure capacitor (C_{dl}). If *a* = 0.5, the Z_{CPE} becomes the Warburg impedance (Z_w) ascribed to the diffusion of the supporting electrolyte ions. Warburg impedance (Z_w) explains the diffusion process in dielectric spectroscopy, which is oscillating linearly at 45º at the low-frequency region of the semi-circle [84,86].

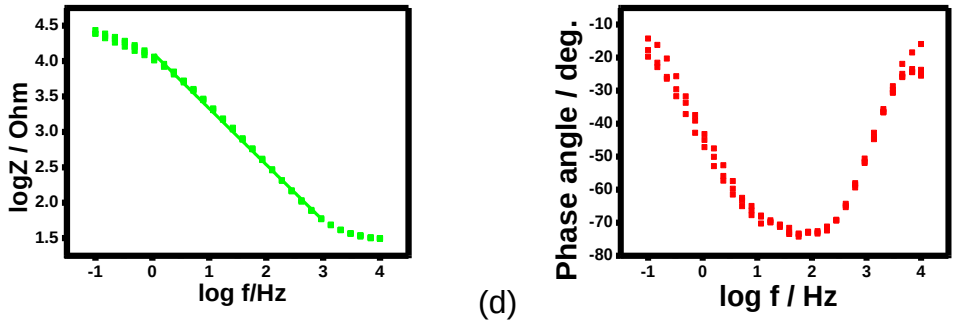
Nyquist plots are shown in **Figure 2.2(a,b)**, with their Voigt *EEC* models and circuit elements (R_s, R_{ct}, C_{dl} and Z_W). The Bode plots (a plot of phase angle *against* the logarithm of frequency and a plot of the logarithm of impedance *against* the logarithm of frequency, **Figure 2.2(c,d)**, give additional information on the phase angle, as well as adsorption and diffusion properties of the analyte on the electrode surface.



(a)



(b)



(c) (d)

Figure 2.2: (a,b) Nyquist plots with their respective Voigt *EEC* models and circuit elements (R_s, R_{ct}, $C_{dl,}$ and Z_{CPE}), and (c,d) typical Bode plots.

2.6.4 Chronoamperometry

Chronoamperometry is a technique employed in the measurement of the current–decay for the diffusion-controlled process occurring at an electrode with respect to time. It is performed by applying a potential step to the WE and recording the current with respect to time. Chronoamperometry tests the kinetics of the electrochemical activity, as well as the stability of the electrocatalysts in an electrochemical system [89,90].

For diffusion-controlled reactions, the current obtained at each point is captured by the Cottrell equation [91,80]:

$$i(t)\frac{nFAD_o^{1/2}C_o}{\pi^{1/2}t^{1/2}} \qquad \textbf{2.19}$$

where n is the number of electrons transferred in the redox reaction, F is the Faraday constant, A is electrode surface area (cm^2), D_o is the diffusion coefficient of the electroactive species, C_o is the bulk concentration of the electroactive species (mol cm^{-3}), and t is time.

Chronoamperometry helps to determine any one of the variables in the Cottrell equation (sample concentration, electrode surface area, or diffusion coefficient) provided the other two variables are given and the contributions from adsorbed material are negligible [92,93].

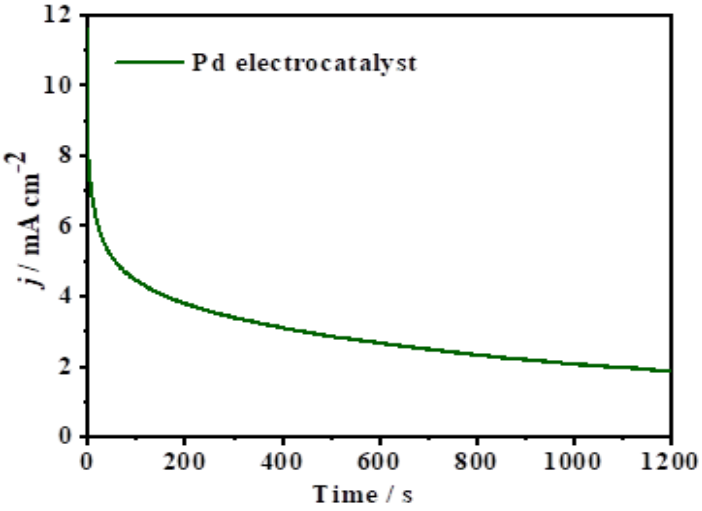
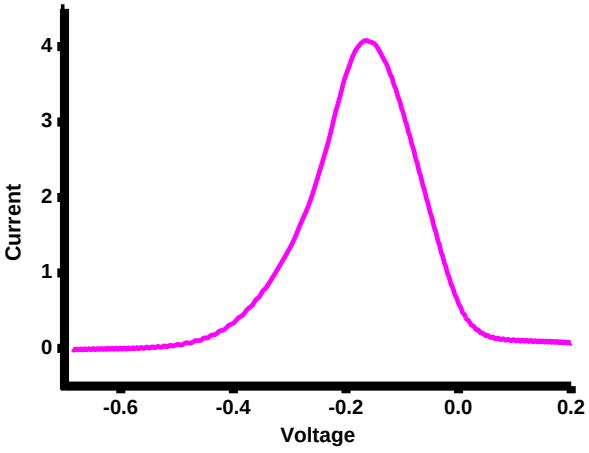


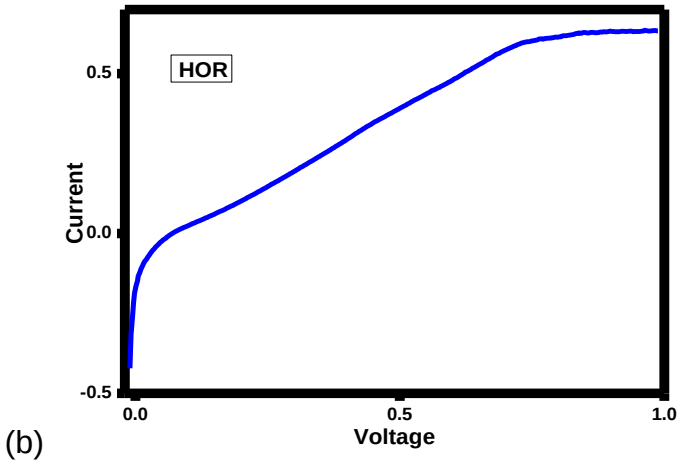
Figure 2.3: A typical CA curve of Pd electrocatalyst at $E_{1/2}$ or OCV for EOR.

2.6.5 Linear Sweep Voltammetry

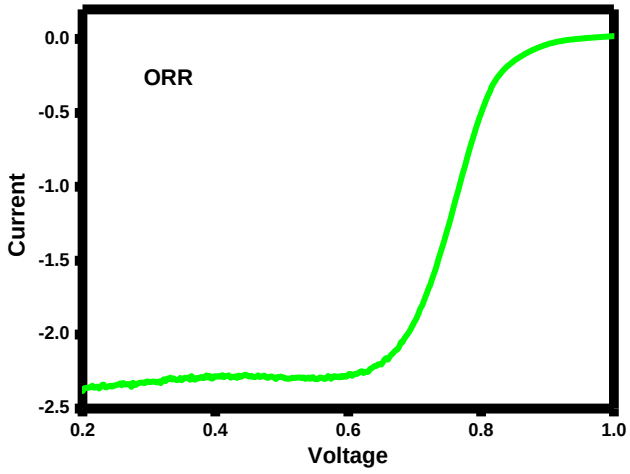
In this type of voltammetry, the current at the WE is measured as the potential is scanned linearly in time between the WE and RE [94].



(a)



(b)



(c)

Figure 2.4: A typical linear sweep voltammogram for (a) EOR (b) HOR (c) ORR

The LSV is also known as a polarization curve and its set-up is as that of the CV. A three-electrode (WE, RE, and CE) configuration is connected to a potentiostat.

From the polarization curves, the kinetic parameters of the electrocatalysts are determined for the different reactions. The kinetic parameters are obtained using the conventional Tafel formula (**Equations 2.20** and **2.21**), whose values are summarized later.

$$\eta = a + b\log j \quad \textbf{2.20}$$

$$b = \frac{2.303RT}{(1-\alpha)nF} \quad \textbf{2.21}$$

where η is the overpotential, a is the Tafel constant, b is the Tafel slope, α is the electron transfer coefficient, R is the universal gas constant, T is the absolute temperature, n is the number of electrons transferred and F is the Faraday constant.

2.7.5 Rotating Disk Electrode (RDE) and Rotating Ring Disk Electrode (RRDE)

The WE used in potentiostatic electrochemical measurements is a modified-GCE without any form of agitation or rotation, but in the case of a few measurements involving potentiodynamic systems, the WE is a modified rotating disk electrode (RDE) that rotates about a fixed axis during the experiment. The rotation agitates the electrolyte and causes the analyte to flow to the electrode [67]. This reduces the diffusion layer thickness of gaseous analytes. Potentiodynamic techniques are usually employed to study the production or consumption of gaseous analytes (such reactions like HOR, ORR, OER, HER). The rotating ring disk electrode (RRDE) (**Figure 2.5b**) is often employed during the ORR to further investigate the mechanism of the potentiodynamic reaction. It operates using the same principle as the RDE (**Figure 2.5a)** but makes use of two working electrodes (the ring and the disk). Both working electrodes are separated by an insulating barrier and are individually connected to the potentiostat to control the system concurrently. The ring which is fixed around the central disk electrode probes intermediate species such as peroxide formation during the ORR. [88]

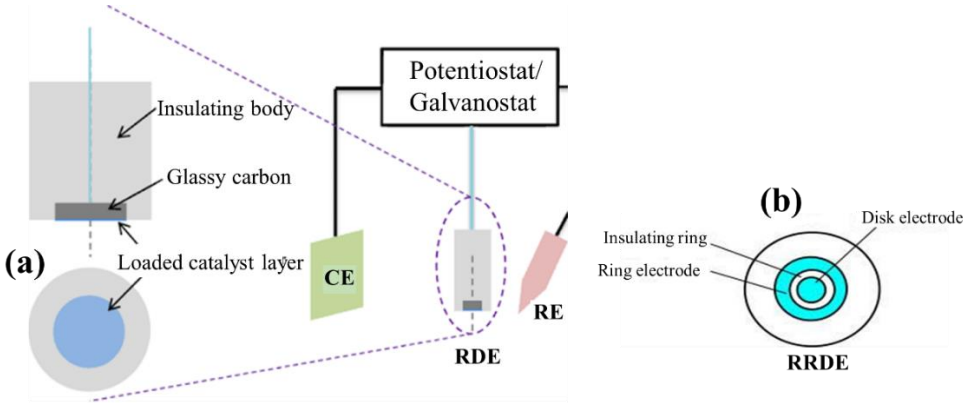


Figure 2.5: Schematic representation of a typical (a) RDE and (b) RRDE

2.7.6 Models Used in Potentiodynamic Experiments.

Kinetic parameters of potentiodynamic reaction are obtained from models such as the Koutecky-Levich and Butler-Volmer equations.

2.7.6.1 Koutecky-Levich (K-L) Equation

The K-L equation is a model used for correcting the mass transport properties of potentiodynamic reactions that used the RDE at different rotation speeds (ω). The K-L model is a straight-line plot of the inverse of current densities (j^{-1}) against the inverse of the square root of scan rates ($\omega^{-1/2}$), as shown in **Figure 2.6a**, following **Equation 2.22**.

The intercept of the plot corresponds to the kinetic-controlled process, while the slope corresponds to the diffusion-controlled process, as shown in **Equation 2.23** and **2.24**.

$$\frac{1}{j} = \frac{1}{j_K} + \frac{1}{j_D} = \frac{1}{j_K} + \frac{1}{B_L \omega^{1/2}} \qquad \textbf{2.22}$$

where j is the mass transfer current density and j_K and j_D are the kinetic and diffusion current densities respectively, B_L is the Levich constant and ω is the rotation speed (rad s^{-1}).

B_L is related to the diffusivity of H_2 gas (D), the number of electrons (n) transferred, and kinematic viscosity of the electrolyte (υ = 0.01 cm^2 s^{-1}) by the equation:

$$B_L = \frac{1}{slope} = 0.62nFC_o D^{2/3}\upsilon^{-1/6} \quad \textbf{2.23}$$

And j_K is related to the heterogeneous electron transfer (K^0) coefficient by:

$$j_K = nFk^0C_o \quad \textbf{2.24}$$

where C_o (1.2 x10^{-6} mol cm^{-3}) is the bulk concentration of O_2 or H_2 gas in 0.1 M KOH.

The ω is obtained in revolution per minute (rpm) and converted to radian per second (rad s^{-1}) using **Equation 2.25**:

$$\text{rad } s^{-1} = \frac{60}{2\pi} \text{ rpm} \quad \textbf{2.25}$$

2.7.6.2 Butler-Volmer (B-V) Equation

The B-V equation is a model employed to investigate the mass transport kinetics of potentiodynamic reactions. It describes the relationship between electric current and the voltage. Therefore, the B-V model is a non-linear plot of the logarithm of current densities (Log j) *vs.* the overpotential (η) which gives curves for the anodic and cathodic contributions as shown in **Figure 2.6b**, following **Equation 2.26**.

The point on the graph where the anodic and cathodic contributions intersect gives the exchange current density.

If either of the anodic or cathodic reaction is in consideration, the B-V equation could collapse to Tafel equation, following **Equation 2.27** and **2.28**, respectively which could be compressed to **Equation 2.20 above**.

$$j = -j_{\mathrm{o}}.e^{\left(\frac{-\alpha.z.F}{RT}.\ \eta\right)} \qquad \textbf{2.26}$$

Simplifying this equation to the anodic and cathodic Tafel equations give:

$$\text{Anodic Tafel:}\quad \eta = \frac{2.303RT}{(1-\alpha_a).z.F} log\, j_{\mathrm{o,s}} - \frac{2.303RT}{(1-\alpha_a).z.F} log\, j_a \qquad \textbf{2.27}$$

$$\text{Cathodic Tafel:}\quad \eta = \frac{2.303RT}{\alpha_{\mathrm{c}}.z.F} log\, j_{\mathrm{o,s}} - \frac{2.303RT}{\alpha_c.z.F} log\, j_{\mathrm{c}} \qquad \textbf{2.28}$$

where η is the overpotential (= working potential – standard potential (0.0 V for RHE)), j_c is the cathodic current density (mA cm^{-2}), and j_a is the anodic current density (mA cm^{-2}); $j_{o,s}$ is the exchange current density (mA cm^{-2}), R is the universal gas constant, T is absolute temperature (K), F is Faraday constant, α_c is the cathodic electron transfer coefficient and α_a is the anodic electron transfer coefficient, while z is the number of electrons involved in electrode reaction (z = 1).

The Ag|AgCl electrode is converted to the reversible hydrogen electrode (RHE) by using **Equation 2.29:**

$$\text{RHE} = E_{\text{Ag|AgCl}} + E^0_{\text{Ag|AgCl}} + 0.0591\text{pH} \qquad \textbf{2.29}$$

where $E_{\text{Ag|AgCl}}$ is the applied potential with respect to the Ag|AgCl reference electrode, $E^0_{\text{Ag|AgCl}}$ is the standard potential of (0.197 V) of the Ag|AgCl electrode and pH is the potential of Hydrogen of the supporting electrolyte.

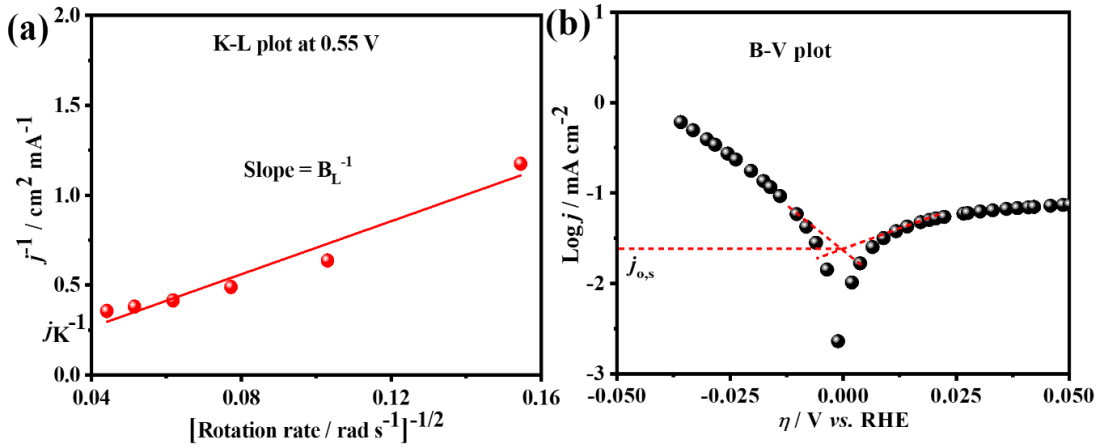


Figure 2.6: (a) Koutecky-Levich plot and (b) Butler-Volmer plot for a potentiodynamic system.

References

1. K. I. Ozoemena, “Nanostructured platinum-free electrocatalysts in alkaline direct alcohol fuel cells: Catalyst design, principles and applications,” *RSC Advances*. 2016, 6, 89523-89550. doi: 10.1039/c6ra15057h.

2. M. Farooque, A. Leo, A. Rauseo, and J. Y. Wang, “Efficient and ultra-clean use of biogas in the fuel cell - the DFC experience,” *Energy. Sustain. Soc.*, 2015, 5(1) doi: 10.1186/s13705-015-0041-0.

3. L. Chen *et al.*, “Platinum nanoparticles encapsulated in nitrogen-doped graphene quantum dots: Enhanced electrocatalytic reduction of oxygen by nitrogen dopants,” *Int. J. Hydrogen Energy*, 2017, 42(49), 29192-29200. doi: 10.1016/j.ijhydene.2017.10.078.

4. K. I. Ozoemena *et al.*, “Fuel cell-based breath-alcohol sensors: Innovation-hungry old electrochemistry,” *Current Opinion in Electrochemistry*. 2018, 10, 82-87. doi: 10.1016/j.coelec.2018.05.007.

5. H. W. Bay, K. F. Blurton, H. C. Lieb, and H. G. Oswin, “Electrochemical measurements of blood alcohol levels,” *Nature*, 1972, 240, 52–53. doi: 10.1038/240052a0.

6. R. A. Rightmire, R. L. Rowland, D. L. Boos, and D. L. Beals, “Ethyl Alcohol Oxidation at Platinum Electrodes,” *J. Electrochem. Soc.*, 1964, 111(2), 242. doi: 10.1149/1.2426092.

7. H.N. Behling, “Fuel cells current technology challenges and future research needs,” Amsterdam. Elsevier, 2013, pp. 8-12

8. H. Sotouchi and A. Hagiwara, “Phosphoric Acid Fuel Cells,” Ohta, T. Energy carriers and conversion systems Vol.2: Encyclopedia of life support systems. Oxford. Eolss Publishers, 2009, pp. 333-339

9. S. Curtin and J. Gangi, Fuel Cell Technologies Market Report.Energy Efficiency and Renewable Energy. US Departement of Energy, 2014.

10. E.C. Kumbur and M.M. Mench, Water Management. In: C K. Dyer, P.T. Moseley, Z.J. Ogumi, D. Rand, and B. Scrosati, Encyclopedia of Electrochemical Power Sources eds. Oxford. Academic Press, 2009, pp. 828-847

11. K. Yang Nam, Perovskite – related and trigonal RBaCo4O7 – B University of Texas Austin, USA, 2011.

12. M. Liu *et al.*, “Enhanced sulfur and coking tolerance of a mixed ion conductor for SOFCs: BaZr0.1Ce0.7y0.2-XYb xO3-δ,” *Science (80-.).*, 2009, 326 (5949), 126-129. doi: 10.1126/science.1174811.

13. C. Zhe, J. H. Wang, Y.M. Choi, L. Yang, M.C. Lin and M. Liu. From Ni – YSZ to Sulfur - tolerant anodes: Electrochemical behaviour, modelling, in situ characterization, and perspectives. Energy Envision Science Perspect Review, 2011, 4, 4380 – 4409.

14. X. Ge, X. Huang, Y. Zhang, Z. Lu, J. Yu, K. Chen, D. Dung, Z. Liu, J Miao and W Su, “Screen-printed thin YSZ films used as electrolytes for solid oxide Fuel Cells," *Journal of Power Sources*, 2006, 159, 1048-1050.

15. D. Sánchez, R. Chacartegui, A. Muñoz, and T. Sánchez, “Thermal and electrochemical model of internal reforming solid oxide fuel cells with tubular geometry,” *J. Power Sources*, 2006, 160, 1074-1087. doi: 10.1016/j.jpowsour.2006.02.098.

16. Y. Wang, K. S. Chen, J. Mishler, S. C. Cho, and X. C. Adroher, “A review of polymer electrolyte membrane fuel cells: Technology, applications, and needs on fundamental research,” *Applied Energy*, 2011, 88, 981-1007. doi: 10.1016/j.apenergy.2010.09.030.

17. F. A. de Bruijn, R. C. Makkus, R. K. A. M. Mallant, and G. J. M. Janssen, “Chapter Five Materials for State-of-the-Art PEM Fuel Cells, and Their Suitability for Operation Above 100°C,” in *Advances in Fuel Cells*, 2007.

18. A. Z. Weber and J. Newman, “Chapter Two Macroscopic Modeling of Polymer-Electrolyte Membranes,” in *Advances in Fuel Cells*, 2007, (1), 48.

19. J. Jia, Q. Li, Y. Wang, Y. T. Cham, and M. Han, “Modeling and dynamic characteristic simulation of a proton exchange membrane fuel cell,” *IEEE Trans. Energy Convers.*, 2009, 24(1), 283-291. doi: 10.1109/TEC.2008.2011837.

20. Z. Belkhiri, M. Zeroual, H. Ben Moussa, and B. Zitouni, “Effect of temperature and water content on the performance of PEM fuel cell,” *Rev. des Energies Renouvelables*, 2011, 14(1), 121 – 130.

21. A. Su, Y. M. Ferng, J. Hou, and T. L. Yu, “Experimental and numerical investigations of the effects of PBI loading and operating temperature on a high-temperature PEMFC,” *Int. J. Hydrogen Energy*, 2012, 37(9), 7710-7718. doi: 10.1016/j.ijhydene.2012.02.004.

22. Y. Shimazaki *et al.*, “Preparation and characterization of long-lived anode catalyst for direct methanol fuel cells,” *J. Colloid Interface Sci.*, 2006, 300, 253 – 258. doi: 10.1016/j.jcis.2006.03.030.

23. M. Alhassan and M. Umar Garba, “Design of an Alkaline Fuel Cell,” *Leonardo Electron. J. Pract. Technol.*, 2006, (9), 99 -106.

24. B. Y. S. Lin, D. W. Kirk, and S. J. Thorpe, “Performance of alkaline fuel cells: A possible future energy system?,” *J. Power Sources*, 2006, 161, 74-483. doi: 10.1016/j.jpowsour.2006.03.052.

25. G. Crawley, Opening doors to fuel cell commercialization, Alkaline Fuel cells (AFC). Fuel Cell Today, 2006, 1-10

26. D. Linden, Handbook of Batteries and Fuel Cells. New York. McGraw Hill, 1984 pp. 41-43

27. J. Larminie, and A. Dicks, Fuel Cells systems explained. Chichester. John Wiley & Sons, 2000, pp. 228-290

28. EG and G Technical services Inc. (2004). Fuel Cell handbook. 7th Ed. Morgantown, West Virginia: National Energy Technology Lab, US Department of Energy.

29. I. Pilatowsky, R. J. Romero, C. A. Isaza, S. A. Gamboa, P. J. Sebastian, and W. Rivera, “Cogeneration Fuel Cell - Sorption Air Conditioning Systems,” *Green Energy Technol.*, 2011, pp 25-34; 55-61. doi: 10.1007/978-1-84996-028-1.

30. N. Sammes, R. Bove, and K. Stahl, “Phosphoric acid fuel cells: Fundamentals and applications,” *Curr. Opin. Solid State Mater. Sci.*, 2004, 8, 372-378. doi: 10.1016/j.cossms.2005.01.001.

31. S.A. Abdulkareem (2009). Design and Development of Proton Exchange Membrane (PEM) from Synthetic Rubber and Carbon nanoparticles for PEM Fuel Cell, (PhD Thesis, School of Chemical and Metallurgical Engineering). University of the Witwatersrand, South Africa

32. S. P. S. Badwal, S. Giddey, A. Kulkarni, J. Goel, and S. Basu, “Direct ethanol fuel cells for transport and stationary applications - A comprehensive review,” *Applied Energy*. 2015, 145, 80 – 103. doi: 10.1016/j.apenergy.2015.02.002.

33. R. Szweda, “In an uncertain world,” *III-Vs Rev.*, 2006, 19(9), 2-48. doi: 10.1016/S0961-1290(06)71885-3.

34. S. K. Kamarudin, F. Achmad, and W. R. W. Daud, “Overview on the application of direct methanol fuel cell (DMFC) for portable electronic devices,” *International Journal of Hydrogen Energy*. 2009, **34**(16), 6902 – 6916. doi: 10.1016/j.ijhydene.2009.06.013.

35. F. Opekar and K. Štulík, “Electrochemical sensors with solid polymer electrolytes,” in *Analytica Chimica Acta*, 1999, **385**(1-3), 151 – 162. doi: 10.1016/S0003-2670(98)00583-2.

36. M. Z. F. Kamarudin, S. K. Kamarudin, M. S. Masdar, and W. R. W. Daud, “Review: Direct ethanol fuel cells,” *Int. J. Hydrogen Energy*. 2013, **38**(22), 9438 – 9453. doi: 10.1016/j.ijhydene.2012.07.059.

37. A. Marshall, B. Børresen, G. Hagen, M. Tsypkin, and R. Tunold, “Hydrogen production by advanced proton exchange membrane (PEM) water electrolysers-Reduced energy consumption by improved electrocatalysis,” *Energy*, 2007, 32(4), 431-436. doi: 10.1016/j.energy.2006.07.014.

38. H. A. Gasteiger, S. S. Kocha, B. Sompalli, and F. T. Wagner, “Activity benchmarks and requirements for Pt, Pt-alloy, and non-Pt oxygen reduction catalysts for PEMFCs,” *Applied Catalysis B: Environmental*. 2005, 56(1), 9-35. doi: 10.1016/j.apcatb.2004.06.021.

39. A. Mahata, A. S. Nair, and B. Pathak, “Recent advancements in Pt-nanostructure-based electrocatalysts for the oxygen reduction reaction,” *Catalysis Science and Technology*. 2019, 9(18), 4835 – 4863. doi: 10.1039/c9cy00895k. **9**,18(2019).

40. S. Litster and G. McLean, “PEM fuel cell electrodes,” *Journal of Power Sources*. 2004, 130(1-2), 61-76. doi: 10.1016/j.jpowsour.2003.12.055.

41. M. S. Wilson, J. A. Valerio, and S. Gottesfeld, “Low platinum loading electrodes for polymer electrolyte fuel cells fabricated using thermoplastic ionomers,” *Electrochim. Acta*, 1995, 40(3), 355-363. doi: 10.1016/0013-4686(94)00272-3.

42. Z. Qi and A. Kaufman, “Low Pt loading high performance cathodes for PEM fuel cells,” *J. Power Sources*, 2003, 113(1), 37-43. doi: 10.1016/S0378-7753(02)00477-9.

43. R. P. Ramasamy, *Encyclopedia of Electrochemical Power Sources*, 2009, 2, *Chapter 227,* 787 – 805 *Elsevier Scientific, UK*.

44. I. Firtina, S. Güner, and A. Albostan, “Preparation and characterization of membrane electrode assembly (MEA) for PEMFC,” *Int. J. Energy Res.*, 2011, 35(2), 146-152. doi: 10.1002/er.1773.

45. E. Slavcheva, G. Topalov, G. Ganske, I. Radev, E. Lefterova, and U. Schnakenberg, “Influence of sputtering pressure on surface structure and oxygen reduction reaction catalytic activity of thin platinum films,” *Electrochim. Acta*, 2010, 55(28), 8992-8997. doi: 10.1016/j.electacta.2010.08.047.

46. M. Kim, J. N. Park, H. Kim, S. Song, and W. H. Lee, “The preparation of Pt/C catalysts using various carbon materials for the cathode of PEMFC,” *Journal of Power Sources*, 2006, 163(1), 93–97.

47. K. L. Huang, Y. C. Lai, and C. H. Tsai, “Effects of sputtering parameters on the performance of electrodes fabricated for proton exchange membrane fuel cells,” *J. Power Sources*, 2006, 156(2), 224-231. doi: 10.1016/j.jpowsour.2005.05.088.

48. S. M. George, “Atomic layer deposition: An overview,” *Chem. Rev.*, 2010, 110(1), 111-131. doi: 10.1021/cr900056b.

49. H. Kim, H. B. R. Lee, and W. J. Maeng, “Applications of atomic layer deposition to nanofabrication and emerging nanodevices,” *Thin Solid Films*. 2009, 517(8), 2563 – 2580. doi: 10.1016/j.tsf.2008.09.007.

50. A. M. Fernandez, M. E. Calixto, P. J. Sebastian, S. A. Gamboa, A. M. Hermann, and R. N. Noufi, “Electrodeposited and selenized (CuInSe2) (CIS) thin films for photovoltaic applications,” *Sol. Energy Mater. Sol. Cells*, 1998, 52(3-4), 426-431. doi: 10.1016/S0927-0248(97)00240-7.

51. M. Paunovic, M. Schlesinger, “Fundamentals of Electrochemical Deposition, 2nd Edition,” *Wiley–Interscience, Hoboken, NJ, USA*, 2006. ISBN: 978-0-471-71221-3.

52. P. S. Patil, “Versatility of chemical spray pyrolysis technique,” *Materials Chemistry and Physics*. 1999, 59(3), 185-198. doi: 10.1016/S0254-0584(99)00049-8.

53. C. D. Lokhande, A. M. More, and J. L. Gunjakar, “Microstructure dependent performance of chemically deposited nanocrystalline metal oxide thin films,”

J. Alloys Compd., 2009, 486(1-2), 570-580. doi: 10.1016/j.jallcom.2009.07.009.

54. W. H. Yen, C. C. Hsieh, C. Y. Hung, H. W. Wang, and M. C. Tsui, “Flexible TiO2 working electrode for dye-sensitized solar cells,” *J. Chinese Chem. Soc.*, 2010, 57(5), 1162-1166. doi: 10.1002/jccs.201000167.

55. A. Cannavale, F. Fiorito, M. Manca, G. Tortorici, R. Cingolani, and G. Gigli, “Multifunctional bioinspired sol-gel coatings for architectural glasses,” *Build. Environ.*, 2010, 45(5), 1233-1243. doi: 10.1016/j.buildenv.2009.11.010.

56. A. Rabenau, “The Role of Hydrothermal Synthesis in Preparative Chemistry,” *Angewandte Chemie International Edition in English*. 1985, 24(12), 1026-1040. doi: 10.1002/anie.198510261.

57. W. Ouyang, R. Alain, P. Santiago K. Cerdan-Gomez, R. Luque, *Photoactive Inorganic Nanoparticles: Surface Composition and Nanosystem Functionality Micro and Nano Technologies*, 2019, Chapter 5, 109 – 138.

58. S. Ito *et al.*, “Fabrication of thin film dye sensitized solar cells with solar to electric power conversion efficiency over 10%,” *Thin Solid Films*, 2008, 516(14), 4613-4619. doi: 10.1016/j.tsf.2007.05.090.

59. C. H. Huang, Y. T. Yang, and R. A. Doong, “Microwave-assisted hydrothermal synthesis of mesoporous anatase TiO 2 via sol-gel process for dye-sensitized solar cells,” *Microporous Mesoporous Mater.*, 2011, 142(2-3), 473-480. doi: 10.1016/j.micromeso.2010.12.038.

60. R. Roy, D. Agrawal, J. Cheng, and S. Gedevanishvili, “Erratum: Full sintering of powdered-metal bodies in a microwave field,” *Nature*. 1999, 399(1), 668-670. doi: 10.1038/45853.

61. S. G. Deng and Y. S. Lin, “Microwave synthesis of mesoporous and microporous alumina powders,” *J. Mater. Sci. Lett.*, 1997, 16(15), 1291-1294. doi: 10.1023/A:1018535227021.

62. K. J. Rao, P. A. Ramakrishnan, and R. Gadagkar, “Microwave Preparation of Oxide Bronzes,” *J. Solid State Chem.*, 1999, 148(1), 100-107. doi: 10.1006/jssc.1999.8378.

63. N. Asim, S. Ahmadi, M. A. Alghoul, F. Y. Hammadi, K. Saeedfar, and K. Sopian, “Research and development aspects on chemical preparation techniques of photoanodes for dye sensitized solar cells,” *International Journal of Photoenergy*. 2014, 2014, 21 doi: 10.1155/2014/518156.

64. O. O. Fashedemi, B. Julies, and K. I. Ozoemena, “Synthesis of Pd-coated FeCo@Fe/C core–shell nanoparticles: Microwave-induced ‘top-down’ nanostructuring and decoration,” *Chem. Commun.*, 2013, 49(20), 2034-2036. doi: 10.1039/c3cc38672d.

65. A. K. Rathi, M. B. Gawande, R. Zboril, and R. S. Varma, “Microwave-assisted synthesis - Catalytic applications in aqueous media,” *Coordination Chemistry Reviews*. 2015, 291, 68-94. doi: 10.1016/j.ccr.2015.01.011.

66. N. Elgrishi, K. J. Rountree, B. D. McCarthy, E. S. Rountree, T. T. Eisenhart, and J. L. Dempsey, “A Practical Beginner’s Guide to Cyclic Voltammetry,” *J. Chem. Educ.*, 2018, 95(2), 197–206. doi: 10.1021/acs.jchemed.7b00361.

67. A. Bard and L. Faulkner, “Allen J. Bard and Larry R. Faulkner, Electrochemical Methods: Fundamentals and Applications, New York: Wiley, 2001,” *Russ. J. Electrochem.*, 2002, 38, 1364–1365. https://doi.org/10.1023/A:1021637209564

68. S. J. Hendel and E. R. Young, “Introduction to Electrochemistry and the Use of Electrochemistry to Synthesize and Evaluate Catalysts for Water Oxidation and Reduction,” *J. Chem. Educ.*, 2016, 93, (11), 1951-1956. doi: 10.1021/acs.jchemed.6b00230.

69. S. Ranganathan, T. C. Kuo, and R. L. McCreery, “Facile preparation of active glassy carbon electrodes with activated carbon and organic solvents,” *Anal. Chem.*, 1999, 71(16), 3574–3580. doi: 10.1021/ac981386n.

70. B. D. McCarthy, D. J. Martin, E. S. Rountree, A. C. Ullman, and J. L. Dempsey, “Electrochemical reduction of brønsted acids by glassy carbon in acetonitrile-implications for electrocatalytic hydrogen evolution,” *Inorg. Chem.*, 2014, 53(16), 8350–8361. doi: 10.1021/ic500770k.

71. C. G. Zoski,”Handbook of electrochemistry [electronic resource],” *Handbook of electrochemistry*, 2007.

72. Y. Li, P. L. Tremblay, and T. Zhang, “Anode catalysts and biocatalysts for microbial fuel cells,” in *Progress and Recent Trends in Microbial Fuel Cells*, 2018, 143 – 165.

73. J. Zhang, H. Zhang, J. Wu, and J. Zhang, “Fuel Cell Degradation and Failure Analysis,” in *Pem Fuel Cell Testing and Diagnosis*, 2013, pp 283-335. DOI: 10.1016/B978-0-444-53688-4.00011-5

74. C. Valero Vidal and A. Igual Muñoz, “Influence of protein adsorption on corrosion of biomedical alloys,” in *Bio-Tribocorrosion in Biomaterials and Medical Implants*, 2013, 187-219. DOI: 10.1533/9780857098603.2.187

75. O. V. Boltalina, “Electronic properties and applications of fluorofullerenes,” In *New Fluorinated Carbons: Fundamentals and Applications Progress in Fluorine*

Science Series. 2017, 1-34. https://doi.org/10.1016/B978-0-12-803479-8.00001-2.

76. P. H. Haumesser, “Copper Electroplating: from Superconformal to Extreme Fill,” in *Nucleation and Growth of Metals*, 2016, 71-106. https://doi.org/10.1016/b978-1-78548-092-8.50004-5

77. D. L. Langhus, “Analytical Electrochemistry, 2nd Edition (Wang, Joseph),” *J. Chem. Educ.*, 2002, 79(10), 1207. https://doi.org/10.1021/ed079p1207

78. C. L. C. Ellis, E. Smith, H. Javaid, G. Berns, and D. Venkataraman, “Ion migration in hybrid perovskites,” in *Perovskite Photovoltaics: Basic to Advanced Concepts and Implementation*, 2018, 163-196. https://doi.org/10.1016/B978-0-12-812915-9.00006-X

79. J. BENAVENTE, “Electrochemical impedance spectroscopy as a tool for electrical and structural characterizations of membranes in contact with electrolyte solutions,” in *Recent Advances in Multidisciplinary Applied Physics*, 2005, 463-471. https://doi.org/10.1016/b978-008044648-6/50074-4

80. K. C. Honeychurch, “Printed thick-film biosensors,” in *Printed Films: Materials Science and Applications in Sensors, Electronics and Photonics*, 2012, 366-409. https://doi.org/10.1533/9780857096210.2.366

81. C. L. C. Ellis, E. Smith, H. Javaid, G. Berns, D. Venkataraman, “Perovskite Photovoltaic, Basic to Advanced Concepts and Implementation,” *Academic Press*, 2018, Chapter 6, 163 – 196.

82. T. Mavrič *et al.*, “Electrochemical Biosensor Based on TiO2 Nanomaterials for Cancer Diagnostics,” in *Advances in Biomembranes and Lipid Self-Assembly*, 2018, 27, 63 – 105.

83. A. S. Adekunle and K. I. Ozoemena, “Electron transfer behaviour of single-walled carbon nanotubes electro-decorated with nickel and nickel oxide layers,” *Electrochim. Acta*, 2008, 53(19), 5774-5782. doi: 10.1016/j.electacta.2008.03.044.

84. J. Pillay and K. I. Ozoemena, “Layer-by-layer self-assembled nanostructured phthalocyaninatoiron(II)/SWCNT-poly(m-aminobenzenesulfonic acid) hybrid system on gold surface: Electron transfer dynamics and amplification of H2O2 response,” *Electrochim. Acta*, 2009, 54(22), 5053-5059. doi: 10.1016/j.electacta.2008.12.056.

85. B. O. Agboola and K. I. Ozoemena, “Self-assembly and heterogeneous electron transfer properties of metallo-octacarboxyphthalocyanine complexes on gold electrode,” *Phys. Chem. Chem. Phys.*, 2008, 10(17), 2399-2408. doi: 10.1039/b800611c.

86. K. I. Ozoemena, N. S. Mathebula, J. Pillay, G. Toschi, and J. A. Verschoor, “Electron transfer dynamics across self-assembled N-(2-mercaptoethyl) octadecanamide/mycolic acid layers: Impedimetric insights into the structural integrity and interaction with anti-mycolic acid antibodies,” *Phys. Chem. Chem. Phys.*, 2010, 12(2), 345-357. doi: 10.1039/b915930d.

87. A. T. Chidembo, K. I. Ozoemena, B. O. Agboola, V. Gupta, G. G. Wildgoose, and R. G. Compton, “Nickel(ii) tetra-aminophthalocyanine modified MWCNTs as potential nanocomposite materials for the development of supercapacitors,” *Energy Environ. Sci.*, 2010, 3(2), 228-236. doi: 10.1039/b915920g.

88. T. J. Schmidt, U. A. Paulus, H. A. Gasteiger, and R. J. Behm, “The oxygen reduction reaction on a Pt/carbon fuel cell catalyst in the presence of chloride

anions," *J. Electroanal. Chem.*, 2001, 508, 41-47. doi: 10.1016/S0022-0728(01)00499-5.

89. O. J. Guy and K. A. D. Walker, "Graphene Functionalization for Biosensor Applications," in *Silicon Carbide Biotechnology: A Biocompatible Semiconductor for Advanced Biomedical Devices and Applications: Second Edition*, 2016, 85-141. https://doi.org/10.1016/B978-0-12-802993-0.00004-6

90. M. M. Tusti *et al.*, "Preparation of PtRu/C electrocatalysts by hydrothermal carbonization using different carbon sources," in *Studies in Surface Science and Catalysis*, 2010, 175, 551-554. doi: 10.1016/S0167-2991(10)75106-5.

91. D. H. Evans and M. J. Kelly, "Theory for Double Potential Step Chronoamperometry, Chronocouloimetry, and Chronoabsorptometry with a Quasi-Reversible Electrode Reaction," *Anal. Chem.*, 1982, 54(11), 1727–1729. doi: 10.1021/ac00248a016.

92. J. S. Yu and Z. X. Zhang, "Double potential-step chronoamperometry and chronocoulometry at an ultramicrodisk electrode: Theory and experiment," *J. Electroanal. Chem.*, 1997, 439(1), 73-80. doi: 10.1016/S0022-0728(97)00258-1.

93. B. Rezaei and N. Irannejad, "Electrochemical detection techniques in biosensor applications," in *Electrochemical Biosensors*, 2019, 11-43. https://doi.org/10.1016/B978-0-12-816491-4.00002-4

94. T. M. Nahir, R. A. Clark, and E. F. Bowden, "Linear-Sweep Voltammetry of Irreversible Electron Transfer in Surface-Confined Species Using the Marcus Theory," *Anal. Chem.*, 1994, doi: 10.1021/ac00087a027.

95. L. Zhang, J. Zhang, D. P. Wilkinson, and H. Wang, “Progress in preparation of non-noble electrocatalysts for PEM fuel cell reactions,” *J. Power Sources*, 2006, 156(2),171–82. doi: 10.1016/j.jpowsour.2005.05.069.

96. E. Yeager, “Dioxygen electrocatalysis: mechanisms in relation to catalyst structure,” *J. Mol. Catal.*, 1986, 38, 5–25. doi: 10.1016/0304-5102(86)87045-6.

97. A. J. Bard and L. R. Faulkner, Fundamentals and Applications. New York: Wiley, 1980. Google Scholar

98. Song C., Zhang J. Electrocatalytic Oxygen Reduction Reaction. In: Zhang J. (eds) PEM Fuel Cell Electrocatalysts and Catalyst Layers. Springer, London. 2008. https://doi.org/10.1007/978-1-84800-936-3_2

99. K. Wong and S. Dia, “Nanotechnology in Batteries,” *J. Energy Resour. Technol. Trans. ASME*, 2017, 139(1). doi: 10.1115/1.4034860.

100. M. Zhou, H. L. Wang, and S. Guo, “Towards high-efficiency nanoelectrocatalysts for oxygen reduction through engineering advanced carbon nanomaterials,” *Chemical Society Reviews*. 2016, 45(5), 1273-1307. doi: 10.1039/c5cs00414d.

101. H. Zhang, M. Jin, and Y. Xia, “Enhancing the catalytic and electrocatalytic properties of Pt-based catalysts by forming bimetallic nanocrystals with Pd,” *Chem. Soc. Rev.*, 2012, 41(24), 8035 – 8049. doi: 10.1039/c2cs35173k.

102. J. S. Spendelow and A. Wieckowski, “Electrocatalysis of oxygen reduction and small alcohol oxidation in alkaline media,” *Phys. Chem. Chem. Phys.*, 2007, 9(21), 2654 – 2675.doi: 10.1039/b703315j.

103. D. P. Tang, J. Pan, S. F. Lu, L. Zhuang, and J. T. Lu, “Alkaline Polymer electrolyte fuel cells: Principle, challenges, and recent progress,” *Sci. China Chem.*, 2010, 53, 357 – 364. doi: 10.1007/s11426-010-0080-5.

104. C. Yang *et al.*, “Activating Ag by even more inert Au: A peculiar effect on electrocatalysis toward oxygen reduction in alkaline media,” *Chem. Commun.*, 2013, 49(94), 11023 – 11025. doi: 10.1039/c3cc46522e.

105. J. Suntivich, H. A. Gasteiger, N. Yabuuchi, H. Nakanishi, J. B. Goodenough, and Y. Shao-Horn, “Design principles for oxygen-reduction activity on perovskite oxide catalysts for fuel cells and metal-air batteries,” *Nat. Chem.*, 2011, 3(7), 546 – 550. doi: 10.1038/nchem.1069.

106. T. E. Sutto, “One-step bulk synthesis of stable, near unit-cell sized oxide nanoparticles and nanoparticle blends using KO2,” *Inorg. Chem.*, 2014, 53(9), 4570 – 4578. doi: 10.1021/ic500252c.

107. S. Henning, J. Herranz, and H. A. Gasteiger, “Bulk-Palladium and Palladium-on-Gold Electrocatalysts for the Oxidation of Hydrogen in Alkaline Electrolyte,” *J. Electrochem. Soc.*, 2015, 162, F178 – F189. doi: 10.1149/2.1081501jes.

108. J. Durst, A. Siebel, C. Simon, F. Hasché, J. Herranz, and H. A. Gasteiger, “New insights into the electrochemical hydrogen oxidation and evolution reaction mechanism,” *Energy Environ. Sci.*, 2014, 7(7), 2255 – 2260. doi: 10.1039/c4ee00440j.

109. W. Sheng, H. A. Gasteiger, and Y. Shao-Horn, “Hydrogen Oxidation and Evolution Reaction Kinetics on Platinum: Acid vs Alkaline Electrolytes,” *J. Electrochem. Soc.*, 2010, 157(11), B1529 – B153. doi: 10.1149/1.3483106.

CHAPTER 3

METHODOLOGY

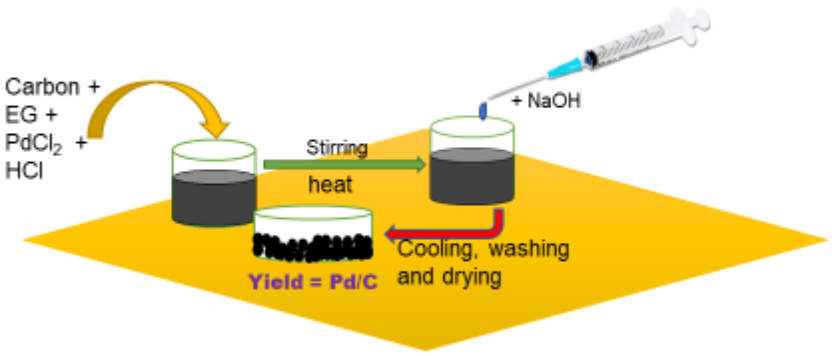
3.1 Synthesis Procedures

The synthesis methods used in this research were adopted from Hamish and *co.* workers [46].

3.1.1 Synthesis of Pd/Carbon (10wt%)

This method was used to synthesize Pd/CB and Pd/OLC. A mixture of the Carbon (250 mg) and EG (ethylene glycol measuring 50 ml) was contained in a three-neck round-bottomed flask (500 ml) and sonicated for 20 minutes. $PdCl_2$ (41.65 mg) was dispersed in a mixture of H_2O (2.083 mL), EG (50 mL) and 0.25 mL HCl (37%). The solution was then added in a dropwise fashion while stirring in a stream of N_2.

After proper stirring, NaOH (5g) was dissolved in H_2O (10 mL) and EG (35 mL) to make an alkaline solution, which was added to the reactor, which was then heated again under a N_2 atmosphere for 3h at 125 °C, and then let to cool to room temperature. The mixture was then filtered leaving behind the desired product, which was then washed with distilled H_2O until a neutral pH and then dried in a vacuum oven at 40 °C. The yield of Pd/CB was 0.77 g and the of Pd/OLC was 0.43 g.



Scheme 3.1: Procedures for synthesis of Pd/C.

3.1.2 Synthesis of Carbon-CeO_2 support (50:50)

A mixture of the Carbon (2g) and a solution of $Ce(NO_3)_3.6H_2O$ (5.05g) in H_2O (125 mL) was stirred for 60 minutes and sonicated for 30 minutes. The pH was then adjusted to 12 with KOH, and it was stirred for 2 hours. The mixture was then filtered leaving behind the desired product, which was then washed with distilled H_2O until a neutral pH and then dried in a vacuum oven at 65°C, and thereafter heated under air in a tube furnace for 2 hours at 250°C. The product was cooled to room temperature under a flow of Ar. The yield of CB-CeO_2 was 2.96g, while the yield of OLC-CeO_2 was 2.51g.

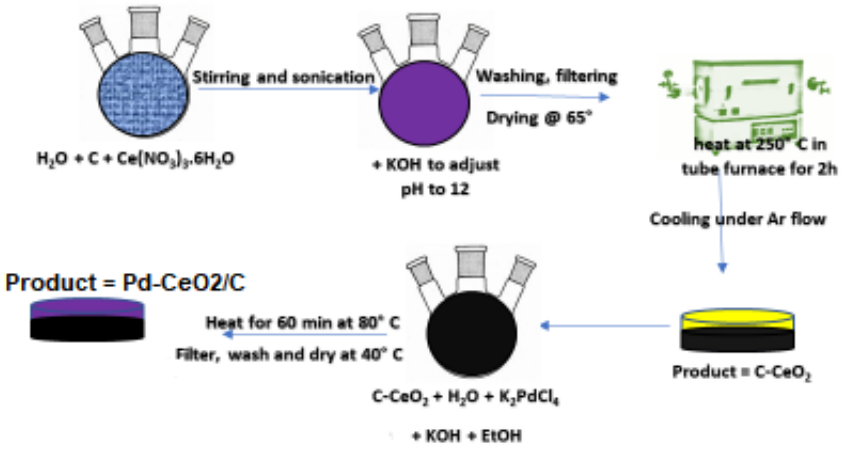
3.1.3 Synthesis of Pd/CeO_2-CB (10wt%Pd)

CB-CeO_2 (250mg) in water (31mL) was vigorously stirred for 30 minutes and sonicated for 20 minutes. A solution of K_2PdCl_4 (86.25mg) in water (3.75mL) was then slowly added (during approx. 1 hour) whilst stirring. This was followed by the addition of an aqueous solution of 2.5M KOH (0.525mL), after which ethanol (50mL) was added. The resulting mixture was heated for 60 minutes at 80°C, after which it was drained, leaving behind the desired product (Pd-CeO_2/CB), which was then

washed several times with distilled water until a neutral pH and dried under vacuum at 65°C. The product (Pd-CeO_2/CB) yield of was 0.49g.

3.1.4 Synthesis of Pd/CeO_2-OLC (10wt%Pd)

A suspension of OLC-CeO_2 (500mg) in water (62.5mL) was vigorously stirred for 30 minutes and sonicated for 20 minutes. A solution of K_2PdCl_4 (172.5mg) in water (7.5mL) was then slowly added (during approx. 1 hour) whilst stirring. This was followed by the addition of an aqueous solution of 2.5M KOH (1.05mL), after which ethanol (50mL) was added.



Scheme 3.2: Procedures for synthesis of Pd-CeO_2/Carbon.

The resulting mixture was heated for 60 min at 80°C, after which it was drained, leaving behind the desired product (Pd-CeO_2/OLC), which was then washed with distilled water until a neutral pH and dried under vacuum at 65°C. The product (Pd-CeO_2/OLC) yield of was 0.93g.

3.2 Material Characterization Methods

3.2.1 Powder X-ray diffraction (structure determination)

Powder X-ray diffraction (PXRD) analysis is particularly helpful in phase identification of components in a prepared sample [1]. A phase is a crystalline solid consisting of a regular, repeating 3-dimensional arrangement of its atoms or molecules [2]. X-ray diffraction can be used to analyze all solid materials (inorganic and organic solids). Since all crystalline materials, even when in a mixture, can interact with X-rays to produce unique diffraction patterns, XRD provides information on the crystal structure of the electrocatalyst.

In this study, powder X-ray diffraction spectroscopy (Bruker D2 Phaser X-ray diffractometer using a Cu Kα source of wavelength, 1.5406 Å) was used to investigate the particle sizes of the electrocatalysts as well as their crystalline structures and crystallographic phases.

The crystallite size of the X-ray diffractograms are calculated using Scherrer's formula, given in **Equation 3.1**.

$$D = \frac{K\lambda}{\beta\ cos\theta} \qquad \mathbf{3.1}$$

Where D is the mean crystallite size, *K* is the Sherrer constant (0.9), λ the wavelength of the x-ray source, *β* is the full-width half maximum (in radians) of the peak in consideration after baseline subtraction in radians, and θ is derived from the peak position (2θ) (in radians).

3.2.2 Raman spectroscopy

Raman spectroscopy is a non-contacting, non-destructive technique employed to obtain both qualitative and quantitative molecular information from a sample. It is

used to characterize a material by its unique vibrational and crystallographic information, which is derived from the material's electronic states and phonon energy dispersion. A Raman spectrum is obtained by exciting a sample with a laser. The inelastic scattering of photons from the vibrations within the molecules is then measured at low wave number resolution. It is performed at room temperature and ambient pressure [18,19,20,26].

Raman spectroscopy is a very useful in the characterization of carbon nanomaterials (their detailed structure and configurations). It is used to obtain the bonding type, domain size, and internal stress in amorphous and nanocrystalline carbon material [21]. The D peak, occurring around 1350 cm^{-1} is associated with nanocrystalline carbon, while the G peak occurring around 1580 cm^{-1} is associated with amorphous carbon (still sp^2 bonded). The peak positions and ratios of peak intensity are different for different carbon materials [22].



Figure 3.1: Bruker Senterra laser Raman spectrometer.

The most prominent Raman spectral features of graphitic materials are the G and G′ bands (located at around 1582 cm^{-1} and 2700 cm^{-1} respectively), and the D and D′ bands (appearing at around 1350 cm^{-1} and 1620 cm^{-1} respectively) [26].

The D peak is due to the breathing modes of six-atom rings and its activation is induced by a defect. The G peak is a doubly degenerate (iTO and LO) phonon mode (corresponding to the E_{2g} phonon) at the Brillouin zone center that is Raman active for sp^2 carbon networks. The presence of the G band in the Raman spectra, suggests that the sample contains sp^2 carbon networks [23,24,25,26]. The D and D' bands are present in defective carbon materials and so cannot be seen for a highly crystalline graphite. The ratio of the I_D/I_G peak is widely used as a measure of structural defects present in graphitic materials [26].

Both the D and G peaks result from vibrations of sp^2-bonded carbon atoms. While the G peak results from in-plane vibrations, the D peak results from out-of-plane vibrations. I_D/I_G ratio is related to the sp^3/sp^2 carbon ratio. If the carbon material is fully oxidized, they are all sp^3. A higher D peak means that the sp^2 bonds are broken; this means that there are more sp^3 bonds and more transition from sp^2 to sp^3 material, and there will be maximum I_D/I_G ratio. If I_D/I_G ratio is higher than pristine material, it means there are defects on carbon material.

The laser Raman spectrometer used in this research was a Bruker Senterra (**Figure 3.1**) fitted with a 50x objective lens for imaging. During the study, the laser excitation wavelength was set to 532 nm and spectral data were evaluated using OPUS 7.1 software. Detailed studies were carried out on the Pd-based products synthesized over the various supported catalysts (C and CeO_2).

3.2.3 Energy dispersive X-ray spectroscopy (EDS)

EDS is employed for the identification of the elements in small samples and the distribution of such elements. [3-8], by focusing a beam of x-rays on the sample to excite the electronic structure of its atoms. This excitation produces X-rays which

have wavelengths and energies that are characteristic of the elements (different elements absorb a specific amount of energy to get excited). The data produced is then shown in the form of a spectrum, histogram, peak patterns and map images. [5-7].

3.2.4 Scanning electron microscopy (SEM)

SEM was used to collect images of the samples. These images reveal information about the morphology and surface properties of each catalyst material [7, 9 ,10,11]. It is a technique commonly used in the field of nanotechnology to visualize and examine nanoparticles and nanocomposites more closely.

The procedure involves fixing a carbon tape to a SEM sample holder, and the sample (powdered) is sprinkled onto the carbon surface. A thin layer of platinum, gold, or carbon coating is then sputtered (≈100 Å) on the sample to ensure that the surface is conductive. This is a requirement for conductive samples. The sample is then examined in a SEM chamber.

Here, a fine beam of electrons is focused into a small probe which is used to scan over a sample. The interaction between the beam and the sample creates an emission of electrons and photons. The signals (back-scattered electrons, secondary electrons, transmitted electrons) emitted by the sample are observed on the detectors. The final product of the interaction of beams is the sample's image [10-13].

A scanning electron microscope employs two image monitors. One monitor is used to observe the specimen and the other one is connected to a photo camera and is used to take images of the specimen [13].

3.2.5 Transmission electron microscopy (TEM) analysis

TEM is usually employed in the examination of the morphology of nanomaterials [7]. It helps to examine the microstructure of nanoparticles and nanocomposites. TEM

employs a nanometer-size electron probe with which it uniquely identifies and quantifies the structures of individual nanocrystals in a sample [14,16]. The image generated from the sample - electron is viewed on an imaging device [7].

Transmission electron microscopy (TEM) and SEM are similar, but for the difference that the beam passes through the sample during TEM [15]. While SEM studies the extrinsic structural morphology of the prepared Pd-based catalysts, TEM is used to generate high resolution images (up to 0.5 nm) of the samples from a high-powered beam of electrons accelerated at 120kV in order to examine their intrinsic structural properties. The source of the electrons here is the field emission or thermionic sources after which a series of lenses facilitate their collection and focus into the optical path.

The optical quality of the lenses determines the resolution of the electron microscope. However, these lenses can be affected by factors such as stigmation as well as spherical and chromatic aberration.

TEM analysis reveals certain properties of materials, such as crystallinity, diameter measurements, grain arrangement, particle size phase transitions, and structural morphology. It also reveals the finest details of internal structure and the data extrapolations from a series of reaction products can be used to determine a step-by-step mechanism of the reaction process.

HRTEM, which is an improvement to TEM makes it possible to obtain information on the crystallographic structure of materials from images. With HRTEM, high phase contrast images as small as a crystal cell can be acquired. [17].

In this research, a FEI Tecnai T12 transmission electron microscope to examine the prepared Pd-based catalysts. About 1 mg of each sample was dispersed over 5mL of ethanol in a glass vial and sonicated for 20 min for a homogeneous mixture. A drop of this homogenous mixture was then deposited all over a copper grid (Structure Probe, Inc. (SPI) carbon copper grid (200 mesh) and allowed to dry. The

copper grid was then positioned on the exchange rod of the instrument's sample holder, which was then inserted into the TEM chamber for analysis.

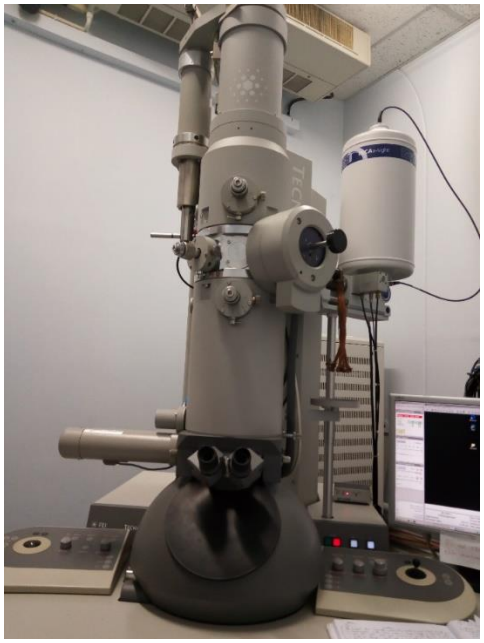


Figure 3.2: FEI Tecnai T12 Transmission Electron Microscope.

3.2.6 Thermogravimetric analysis (TGA)

TGA is concerned with the monitoring the weight changes of a material while the temperature is changed over time under a controlled temperature atmosphere [27]. This technique is used to analyze how thermally stable a nanocomposite is [28] and as well as their fraction of volatile components by recording changes in weight while heating the materials at a constant rate. It is performed with a ThermoGravimetric Analyser (TGA) or thermobalance. This technique may be carried out in vacuum, inert gas atmospheres, ambient air, oxidizing/reducing gases, carburizing or corrosive gases, vapors of liquids or "self-generated atmosphere", as well as constant, controlled or high vacuum pressure.

TGA basically involves heating a sample and measuring its weight as it is heated or cooled in a furnace. Usually, the sample is loaded in a specialized alumina crucible

supported by an instruments' precision balance that measures its mass loss/gain against temperature or time. From the measurements, we can get information about the extent of catalytic metal residue, decarboxylation, decomposition, oxidation, pyrolysis, solvent water as well as weight percentage ash.

The thermal stability of each pd-based sample was studied with the help of a Perkin Elmer Thermogravimetric analyzer (TGA)/Differential Thermogravimetric analysis (DTGA) 6000.



Figure 3.3: Thermal analyzer used for the TGA.

3.2.7 Brunauer-Emmett-Teller (BET) surface area analysis

The specific surface area (SSA) is a parameter measured on solid materials as the total surface area of a material per unit of mass. It is usually measured in $m^2\ kg^{-1}$ or $m^2\ g^{-1}$ and tells the area covered by the material per given mass.

Brunauer-Emmett-Teller (BET) analysis is employed to get this information, which is important for determining the reaction surfaces of a material. Although the SSA can

be determined by different other measurement methods such as gas permeability and calculation from the particle size distribution, these methods, unfortunately, are unable to measure the deep texture of the particles' surface and the fine structure of the material's surface. These factors make the BET analysis more reliable. Brunauer-Emmett-Teller surface area analysis makes use of nitrogen gas being adsorbed on the surfaces of powdered solids, where the volumes adsorbed are measured at a constant temperature (-195 ºC) and the lowest relative pressure.

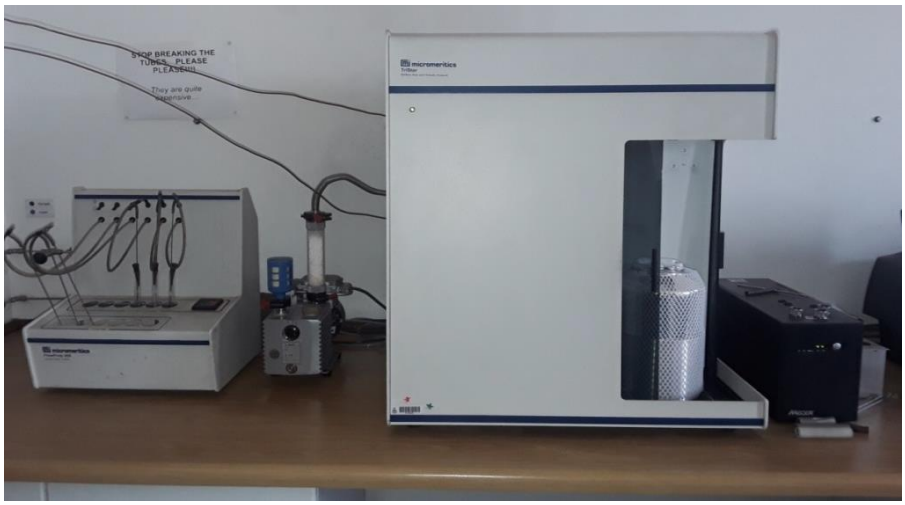


Figure 3.4: The micromeritics RS232 Brunauer -Emmett-Teller (BET) surface area analyzer.

3.2.8 X-ray Photoelectron Spectroscopy (XPS) / Electron Spectroscopy for Chemical Analysis (ECSA)

XPS is a surface-sensitive analytical technique that provides information on quantitative atomic composition and chemistry. It identifies elements in a sample, as well as their chemical states [29,31].

This technique works by irradiating the specimen's surface with x-ray of constant energy, hv, in vacuum (normally better than 10−7 Pa) and determining the kinetic energy spectrum of the photoelectrons (of low energy usually between 50 eV and

2000 eV) emitted from the surface of the sample. The energy given off by these electrons is typical of the atom being bombarded, thus allowing for the identification of elements [29,30,31].

The parameters involved in the XPS experiment are related by the equation:

$$E_B = hv - E_K – W \qquad \textbf{3.2}$$

where hv is the photon energy, E_K is the kinetic energy of the electron, and W is the spectrometer work function. The quantities on the right are known or measurable, and so it is easy to calculate the binding energy of the electron [30].

3.2.9 X-ray Absorption Spectroscopy (XAS)

Synchrotron based methods are used to study the physico-chemical and structural properties of various materials. The synchrotron is a very efficient technique for performing imaging and advanced spectroscopy on various materials as it attains a high photon flux, small source size and low divergence, adapting to the heterogeneity and great complexity of the materials under study.

The x-ray absorption spectroscopy (XAS) technique scans the incident x-ray photon energy in a narrow region around an absorption edge and measures the variation in the absorption coefficient (**Figure 3.5**). This variation in the absorption coefficient is physically related to the excitation cross-section of the core electrons into the vacuum continuum or unoccupied electronic states [32]. The absorption edge is characteristic of the element and the synchrotron energy can be tuned to probe the vicinity of the element in the 3D space.

(a) The *pre-edge* and *edge* regions are restricted to a few eV around the edge (**Figure 3.5, *right***).

(b) The structure above the edge within (30-50eV) is called *XANES* (X-ray Absorption Near Edge Structure) or *NEXAFS* (Near Edge X-ray Absorption Fine Structure) [34, 35]. It can provide information on the local electronic and geometric structure.

(c) The structure extending up to 1000 eV from the XANES region (as in **Figure 3.5** ***right***), is called *EXAFS* (Extended X-ray Absorption Fine Structure) and contains information on the local geometric structure around a given atomic species. [34, 36–41].

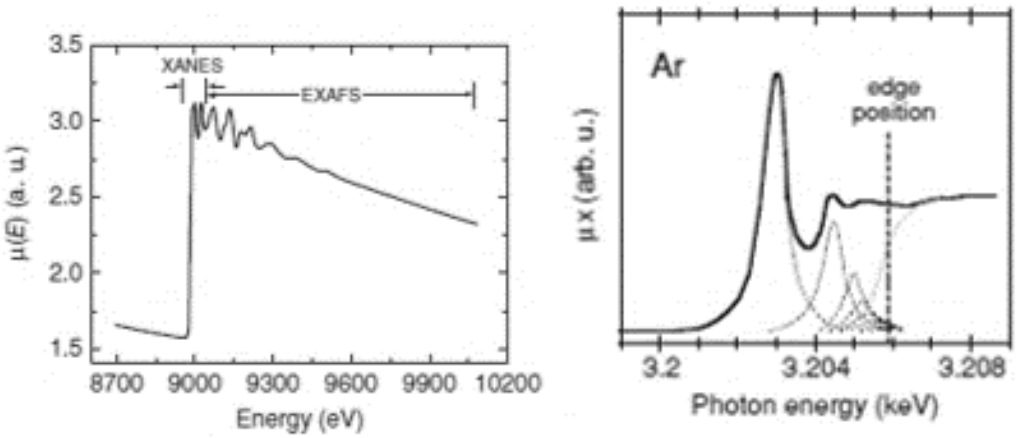


Figure 3.5 ***Left***: XAFS K-edge signal of crystalline copper (indicating the XANES and EXAFS region) [32] and ***Right***: Argon [33]

3.3 Electrochemical Measurements

Electrochemical measurements were used to examine the electrochemical performances of the synthesized electrocatalysts. The experiments were performed in the laboratory under room temperature and ambient pressure except stated otherwise. Two different cells were fabricated for the electrochemical measurements: (i) **three-electrode** configuration for half-cell tests; and (ii) **two-electrode** configuration for full cell tests.

3.3.1: Three-Electrode Configuration

In the three-electrode configuration (**Figure 3.8**) for half-cell reactions, the WE (GCE of 3.0 mm, 0.071 cm^2 or 5.0 mm, 0.196 cm^2) modified with the electrocatalysts ink), counter electrode (Pt wire) and reference electrode (AglAgCl, saturated 3.0 M KCl) are used in aqueous electrolyte.

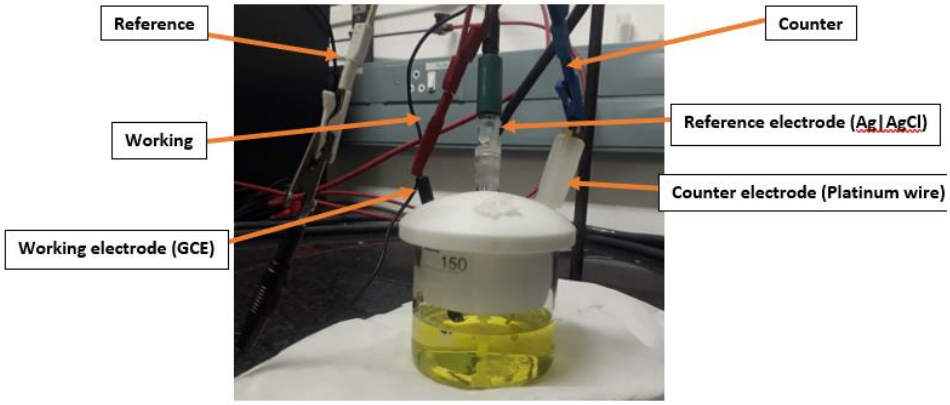


Figure 3.6: A three-electrode configuration for half-cell reactions

3.3.2: Two-electrode configuration for full cell test

The full cell tests involved a 3D-printed cell set-up fabricated with two-electrode configuration: the WE (the cathode) and the CE (the anode), with the reference wire connected to the counter wire. A Cu foil is used as a current collector.

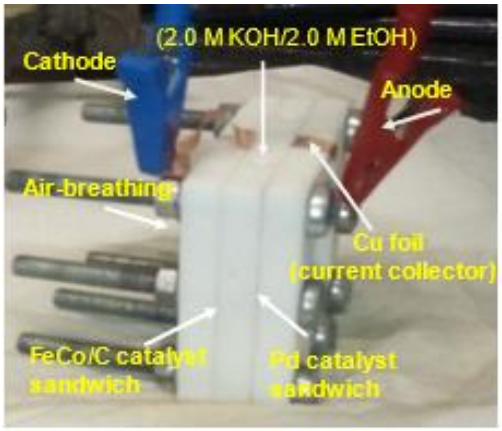


Figure 3.7: A two-electrode 3D-printed cell

3.4 DFT Simulation

The Density Functional Theory (DFT) was performed for the electrodes. All the DFT calculations in this project were carried out on BIOVIA Materials Studio, using *ab initio* DFT. The COMPASS was employed in the simulation. It is the state-of-the-art forcefield and the first *ab initio* high quality forcefield to merge parameters for both organic and inorganic materials that have been previously found in different forcefields, and the first to enable accurate and simultaneous prediction of the characteristics of different molecules under different conditions of temperature and pressure [68,69].

Layers of 3x3 supercells of Pd and CeO_2 were modeled and the top surfaces of the modeled atoms were used as adsorption sites [42]. The energy window and energy difference were set to 100 kcal mol^{-1} and 0.00 kcal mol^{-1} respectively. The adsorption energy, which is a measure of the stability of the gas-solid adsorption complex was calculated for each electrode. Smaller adsorption energy translates to better stability of the adsorption complex [45].

References

1. R. Heimann and R. Heimann, “X-Ray Powder Diffraction (XRPD),” in *The Oxford Handbook of Archaeological Ceramic Analysis*, 2016. https://doi.org/10.1093/oxfordhb/9780199681532.013.19

2. J. Lodge and J. P. Lodge, “X-Ray Powder Diffraction,” in *Methods of Air Sampling and Analysis*, 2018. https://doi.org/10.1201/9780203747407-31

3. S. Ebnesajjad, *Surface treatment of materials for adhesive bonding*. 2013. https://doi.org/10.1016/C2013-0-12914-5

4. A. F. Ismail, K. C. Khulbe, and T. Matsuura, “RO Membrane Characterization,” in *Reverse Osmosis*, 2019, 57-90. https://doi.org/10.1016/b978-0-12-811468-1.00003-7

5. J. Bergström, *Mechanics of Solid Polymers: Theory and Computational Modeling*. 2015. https://doi.org/10.1016/C2013-0-15493-1

6. N. Mehrban and J. Bowen, “Monitoring biomineralization of biomaterials in vivo,” in *Monitoring and Evaluation of Biomaterials and their Performance In Vivo*, 2017, 81-110. https://doi.org/10.1016/B978-0-08-100603-0.00005-5

7. M. Nasrollahzadeh, S. M. Sajadi, M. Sajjadi, and Z. Issaabadi, “An Introduction to Nanotechnology,” in *Interface Science and Technology*, 2019, 28, 1-27. https://doi.org/10.1016/B978-0-12-813586-0.00001-8

8. O. D. Neikov and N. A. Yefimov, “Powder Characterization and Testing,” in *Handbook of Non-Ferrous Metal Powders*, 2019, 3-62. https://doi.org/10.1016/b978-0-08-100543-9.00001-4

9. A. Ul-Hamid, *A Beginners' Guide to Scanning Electron Microscopy*. 2018. https://doi.org/10.1007/978-3-319-98482-7

10. S. Rajeshkumar, L. V. Bharath, and R. Geetha, "Broad spectrum antibacterial silver nanoparticle green synthesis: Characterization, and mechanism of action," in *Green Synthesis, Characterization and Applications of Nanoparticles*, 2019, 429-444. https://doi.org/10.1016/b978-0-08-102579-6.00018-6

11. S. Spiegelberg, "Characterization of Physical, Chemical, and Mechanical Properties of UHMWPE," in *UHMWPE Biomaterials Handbook*, 2009, 355-368. https://doi.org/10.1016/B978-0-12-374721-1.00024-9

12. S. Ebnesajjad and P. R. Khaladkar, "Failure Analysis of Fluoropolymer Parts," in *Fluoropolymer Applications in the Chemical Processing Industries*, 2018, 357-400. https://doi.org/10.1016/b978-0-323-44716-4.00010-5

13. A. Singer, Z. Barakat, S. Mohapatra, and S. S. Mohapatra, "Nanoscale Drug-Delivery Systems," in *Nanocarriers for Drug Delivery*, 2019, 395-419. https://doi.org/10.1016/b978-0-12-814033-8.00013-8

14. S. Bhattacharya, "Electrical Transport Properties of Ion-Conducting Glass Nanocomposites," in *Glass Nanocomposites: Synthesis, Properties and Applications*, 2016, 181-214. https://doi.org/10.1016/B978-0-323-39309-6.00008-0

15. S. Ebnesajjad, "Surface and Material Characterization Techniques," in *Surface Treatment of Materials for Adhesive Bonding*, 2014, 39-75. https://doi.org/10.1016/b978-0-323-26435-8.00004-6

16. S. J. Pennycook *et al.*, “Seeing inside materials by aberration-corrected electron microscopy,” *Int. J. Nanotechnol.*, 2011, 8(10-12), 935 - 947. doi: 10.1504/IJNT.2011.044438.

17. J. M. Herrera-Ramirez, R. Perez-Bustamante, and A. Aguilar-Elguezabal, “An overview of the synthesis, characterization, and applications of carbon nanotubes,” in *Carbon-Based Nanofillers and Their Rubber Nanocomposites: Carbon Nano-Objects*, 2018, 47-75. https://doi.org/10.1016/B978-0-12-813248-7.00002-X

18. J. Gomes, J. Batra, V. R. Chopda, P. Kathiresan, and A. S. Rathore, “Monitoring and control of bioethanol production from lignocellulosic biomass,” in *Waste Biorefinery: Potential and Perspectives*, 2018, 727-749. https://doi.org/10.1016/B978-0-444-63992-9.00025-2

19. D. D. Le Pevelen, “NIR FT-raman,” in *Encyclopedia of Spectroscopy and Spectrometry*, 2016, 98-109. https://doi.org/10.1016/B978-0-12-409547-2.12150-X

20. P. S. Goh, A. F. Ismail, and B. C. Ng, “Raman Spectroscopy,” in *Membrane Characterization*, 2017, 31-46. https://doi.org/10.1016/B978-0-444-63776-5.00002-4

21. P.R. Chalker, Characterization of diamond and diamond-like films, in: R.E. Clausing (Ed.), Diamond and Diamond-like Films and Coatings, Plenum Press, New York, 1991, pp. 127–150.

22. P. K. Chu and L. Li, “Characterization of amorphous and nanocrystalline carbon films,” *Mater. Chem. Phys.*, 2006, 96(2-3), 253-277. https://doi.org/10.1016/j.matchemphys.2005.07.048

23. TUINSTRA F and KOENIG JL, “RAMAN SPECTRUM OF GRAPHITE,” *J. Chem. Phys.*, 1970 53(3), 1126. https://doi.org/10.1063/1.1674108

24. A. Ferrari and J. Robertson, “Interpretation of Raman spectra of disordered and amorphous carbon,” *Phys. Rev. B - Condens. Matter Mater. Phys.*, 2000, 61(20). https://doi.org/10.1103/PhysRevB.61.14095

25. A. C. Ferrari and J. Robertson, “Resonant Raman spectroscopy of disordered, amorphous, and diamondlike carbon,” *Phys. Rev. B - Condens. Matter Mater. Phys.*, 2001, 64(7). https://doi.org/10.1103/PhysRevB.64.075414

26. M. A. Pimenta, G. Dresselhaus, M. S. Dresselhaus, L. G. Cançado, A. Jorio, and R. Saito, “Studying disorder in graphite-based systems by Raman spectroscopy,” *Physical Chemistry Chemical Physics*. 2007,9, 1276-1290. https://doi.org/10.1039/b613962k

27. W. M. Groenewoud, “Chapter 2 - Thermogravimetry,” in *Characterisation of Polymers by Thermal Analysis*, 2001, 61-76. https://doi.org/10.1016/B978-044450604-7/50003-0

28. S. Bandyopadhyay-Ghosh, S. B. Ghosh, and M. Sain, “The use of biobased nanofibres in composites,” in *Biofiber Reinforcements in Composite Materials*, 2015, 571-647. https://doi.org/10.1533/9781782421276.5.571

29. R. W. Welker, “Size Analysis and Identification of Particles,” in *Developments in Surface Contamination and Cleaning: Detection, Characterization, and Analysis of Contaminants*, 2012, 179-213. https://doi.org/10.1016/B978-1-4377-7883-0.00004-3

30. H. Konno, “X-ray Photoelectron Spectroscopy (XPS),” *Zairyo-to-Kankyo*, 1993, 42(1), 27-36. https://doi.org/10.3323/jcorr1991.42.27

31. D. M. Mattox, “Substrate (‘Real’) Surfaces and Surface Modification,” in *Handbook of Physical Vapor Deposition (PVD) Processing*, 2010, 25-72. https://doi.org/10.1016/b978-0-8155-2037-5.00002-2

32. S. Quartieri, “X-Ray Absorption Spectroscopy (XAS, EXAFS, XANES),” in *The Encyclopedia of Archaeological Sciences*, 2018, 1-6. https://doi.org/10.1002/9781119188230.saseas0613.

33. P. Fornasini, “Introduction to x-ray absorption spectroscopy,” in *Synchrotron Radiation: Basics, Methods and Applications*, 2015, pp 181-211. https://doi.org/10.1007/978-3-642-55315-8_6.

34. H. Baumgartel, “EXAFS, SEXAFS, XANES: X-Ray Absorption - Principles, Applications, Techniques of EXAFS, SEXAFS and XANES. Von D. Koningsberger und R. Prins. John Wiley & Sons Ltd., Chichester 1988. 673 S., Abb., Tab., Formeln. ISBN 0-471-87547-3,” *Nachrichten aus Chemie, Tech. und Lab.*, 1988, 36(6), 650-650. doi: 10.1002/nadc.19880360617.

35. J. Stöhr, *NEXAFS Spectroscopy* (Springer, Berlin, 1992)

36. G. Bunker, *Introduction to XAFS* (Cambridge University Press, Cambridge, 2010)

37. S. J. Gurman, “Interpretation of EXAFS Data,” *J. Synchrotron Radiat.*, 1995, 2, 56-63. doi: 10.1107/s0909049594009179.

38. T. M. Hayes and J. B. Boyce, “Extended X-Ray Absorption Fine Structure Spectroscopy,” *Solid State Phys. - Adv. Res. Appl.*, 1983, 37, 173-351, doi: 10.1016/S0081-1947(08)60667-0.

39. P. A. Lee, P. H. Citrin, P. Eisenberger, and B. M. Kincaid, “Extended x-ray absorption fine structure its strengths and limitations as a structural tool,” *Rev. Mod. Phys.*, 1981, 53, 769-806. doi: 10.1103/RevModPhys.53.769.

40. D. E. Sayers, E. A. Stern, and F. W. Lytle, “New technique for investigating noncrystalline structures: Fourier analysis of the extended x-ray-absorption fine structure,” *Phys. Rev. Lett.*, 1971, 27, 1204-1207. doi: 10.1103/PhysRevLett.27.1204.

41. B.K. Teo, *EXAFS: Basic Principles and Data Analysis* (Springer, Berlin, 1986)

42. E. D. Wang, J. B. Xu, and T. S. Zhao, “Density functional theory studies of the structure sensitivity of ethanol oxidation on palladium surfaces,” *J. Phys. Chem. C*, 2010, 114(23), 10489–10497, doi: 10.1021/jp101244t.

43. H. Sun, “Compass: An ab initio force-field optimized for condensed-phase applications - Overview with details on alkane and benzene compounds,” *J. Phys. Chem. B*, 1998, *102*, 7338–7364. doi: 10.1021/jp980939v.

44. M. J. McQuaid, H. Sun, and D. Rigby, “Development and validation of COMPASS force field parameters for molecules with aliphatic azide chains,” *J. Comput. Chem.*, 2004, 25(1), 61–71. doi: 10.1002/jcc.10316.

45. S. Gautier, S. N. Steinmann, C. Michel, P. Fleurat-Lessard, and P. Sautet, “Molecular adsorption at Pt(111). How accurate are DFT functionals?,” *Phys. Chem. Chem. Phys.*, 2015, 17, 28921–28930.doi: 10.1039/c5cp04534g.

46. H. A. Miller *et al.*, “Highly active nanostructured palladium-ceria electrocatalysts for the hydrogen oxidation reaction in alkaline medium,” *Nano Energy*, 2017, 33, 293 – 305. doi: 10.1016/j.nanoen.2017.01.051.

CHAPTER 4

RESULTS AND DISCUSSION

4.1 Materials Characterization

4.1.1 XRD spectroscopy of the electrocatalysts

The patterns obtained from the XRD measurements of the Pd catalysts confirmed successful synthesis of the catalysts. **Figure 4.1a** shows the XRD patterns of the CB/CeO_2 and OLC/CeO_2 powder and **Figure 4.1b** shows the XRD patterns of Pd/CB, Pd/OLC, Pd-CeO_2/CB and Pd-CeO_2/OLC.

The hexagonal carbon structure was observed at 2θ values of 24.3°, 25.6°, 25.9° and 26.1° for Pd/CB, Pd-CeO_2/CB, Pd/OLC and Pd-CeO_2/OLC, respectively.

The peaks due to palladium are recorded at 2θ ≈ 40°, 47°, 68°, 82° and 86° which are in good accordance with the FCC (face centred cubic) structure of the crystal planes Pd(111), Pd(200), Pd(220), Pd(311) and Pd(222) respectively. The diffraction patterns of ceria are observed at 2θ = 28.7°, 32.7°, 47.3°, 56.2°, 69.1°, 77.7° and 88.4°. These results agree with XRD patterns of Pd/C and Pd-CeO_2/C that have been reported in literature [20, 22].

The diffraction peaks of the Pd-CeO_2/CB and Pd-CeO_2/OLC are broader than their carbon-only supported counterparts. This may suggest that with the addition of ceria, the particle sizes of the Pd are reduced.

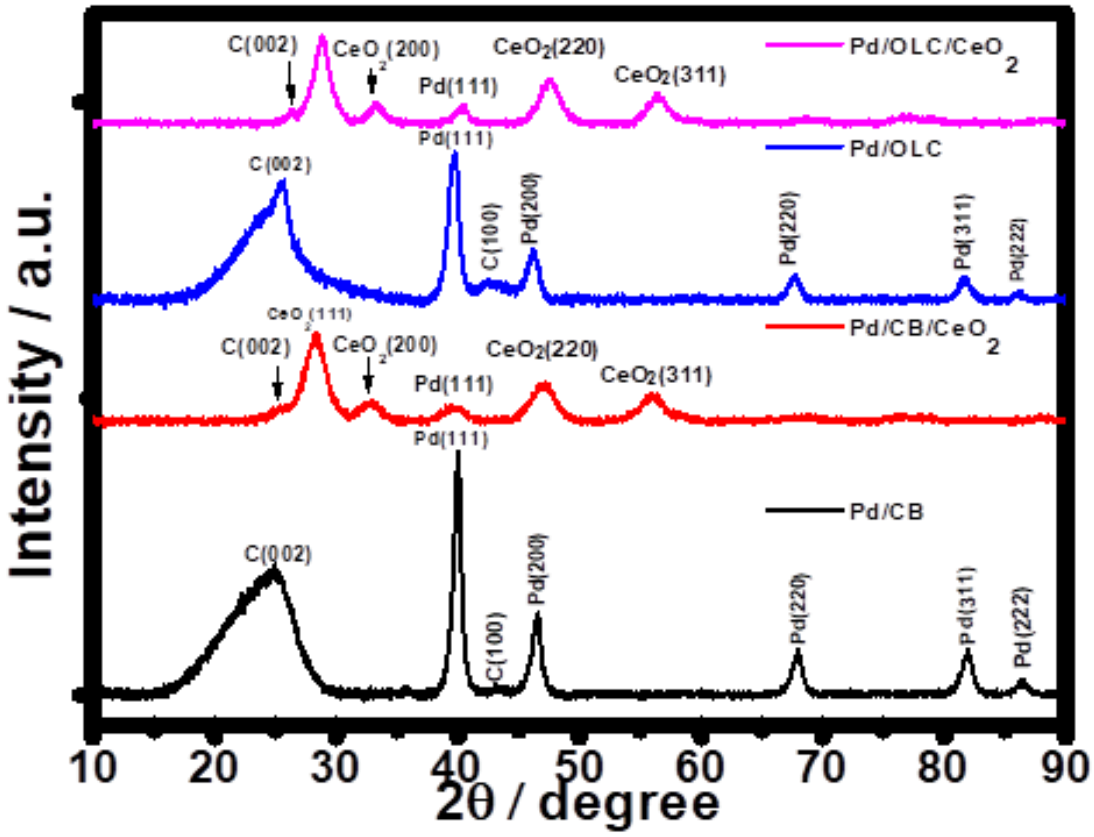


Figure 4.1: XRD patterns of the Pd/CB, Pd-CeO_2/CB, Pd/OLC and Pd-CeO_2/OLC nanocatalysts.

The lattice parameters (lattice spacing (*d* / Å), and crystallite sizes (D / nm)) of the electrocatalysts at 2θ of *ca.* 40º were calculated following Scherrer's equation (**Equation 3.1**) and summarized in **Table 4.1**, where the crystallite size of the electrocatalysts containing CeO_2 are observed to be reduced. Deformations (strain) in materials are due to dislocations. The dislocation density (δ) and micro-strain (*ε*) were obtained by using **Equation 4.1** and **4.2** respectively.

$$\delta = \frac{1}{D^2} \qquad \textbf{4.1}$$

$$\varepsilon = \frac{\beta}{4\tan\theta} \qquad \textbf{4.2}$$

Where β is the FWHM.

Larger dislocation density and micro-strain are observed for the catalysts containing CeO_2 nanoparticles than the ones without CeO_2, suggesting that the catalysts containing CeO_2 nanoparticles possess more surface defects [25].

Table 4.1: Lattice parameters of the Pd -based electrocatalysts at 2θ of *ca.* 40º.

Lattice parameters	Pd-based Electrocatalysts			
	Pd/CB	Pd-CeO_2/CB	Pd/OLC	Pd-CeO_2/OLC
2θ / º	39.953	39.707	39.650	40.317
d / Å	2.254	2.268	2.271	2.235
D / nm	8.790	4.304	7.973	6.750
Micro strain ε	0.661	1.358	0.734	0.796
Dislocation density δ (nm^{-2})	0.012	0.053	0.015	0.0190

4.1.2 Raman spectroscopic analysis of the nanocatalysts

The Raman spectra (**Figure 4.2**) of the nanocatalysts showed two peaks between 1000 cm^{-1} (corresponding to the D band) and 2000 cm^{-1} (corresponding to the G band). The peak positions and intensity ratios (I_D/I_G) are given in **Table 4.2**. The peaks are ascribed to the D band for disorder induced by C–C vibration band and the G band for C=C graphite carbon vibration frequency of the carbon material with sp^2 orbital structure. The D band is due to out-of-plane vibrations attributed to the sp^3-bonded carbon atoms, while the G band is due to in-plane displacement of sp^2-bonded carbon atoms [1-3].

The I_D/I_G intensity ratios were used to quantify the degree of crystallinity/disorder on the materials. The I_D/I_G values of Pd/CB, Pd-CeO_2/CB, Pd/OLC and Pd-CeO_2/OLC, which can be used as references for the degree of graphitization, are recorded as 3.31, 3.31, 1.56 and 2.24, respectively. A reduction in the I_D/I_G ratio confirms increased graphitization. This suggests better graphitization in Pd/OLC [4].

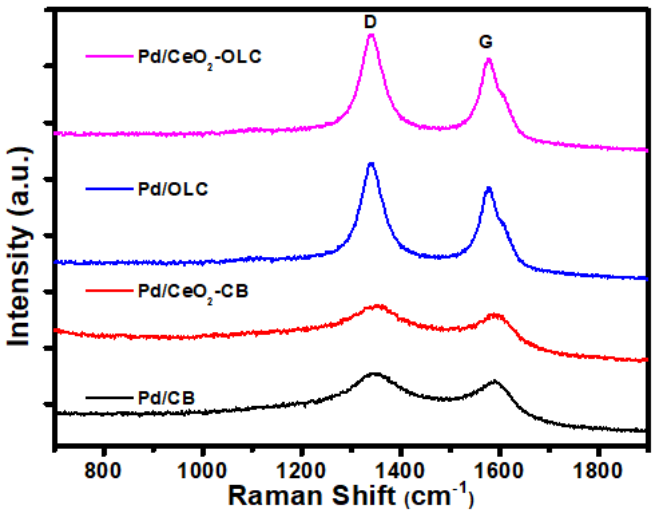


Figure 4.2: Raman spectra of the nanocatalysts.

Table 4.2: Summary of the Raman data for the nanocatalysts.

	D band		G band		
Sample	***Raman intensity (Area under the peak)***	***Raman shift λ^{-1} (cm^{-1})***	***Raman intensity (Area under the peak)***	***Raman shift λ^{-1} (cm^{-1})***	***I_D/I_G ratio***
Pd/OLC	116100.44	1341.30	74357.47	1580.58	1.56
Pd/CB	154942.24	1349.72	46800.28	1584.12	3.31
Pd/CeO_2 -OLC	34768.63	1343.16	15547.53	1580.69	2.24
Pd/CeO_2 -CB	154942.24	1349.72	46800.28	1584.12	3.31

4.1.3 Chemical composition and particle morphology analyses

The EDS spectra of the as-prepared nanomaterials (Pd/CB, Pd/OLC, Pd-CeO_2/CB and Pd-CeO_2/OLC) contained different elements with different ratios and were identified. The results (**Figure 4.3**) confirm the presence of carbon by displaying a peak due to carbon (C). The peaks due to cerium (Ce) and oxygen (O) are visible in the results for the catalyst that contain CeO_2 as support. The copper (Cu) peaks are due to the sample holder (copper grid) employed in the study.

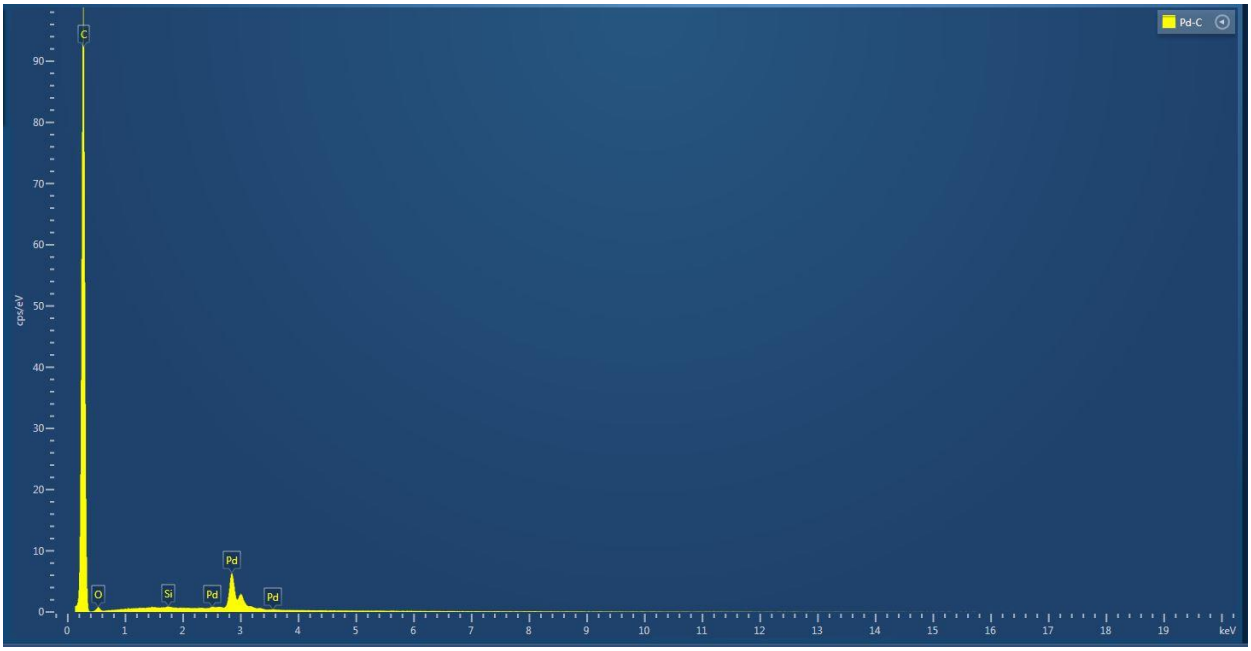


Figure 4.3(a). EDS spectrum of Pd/CB

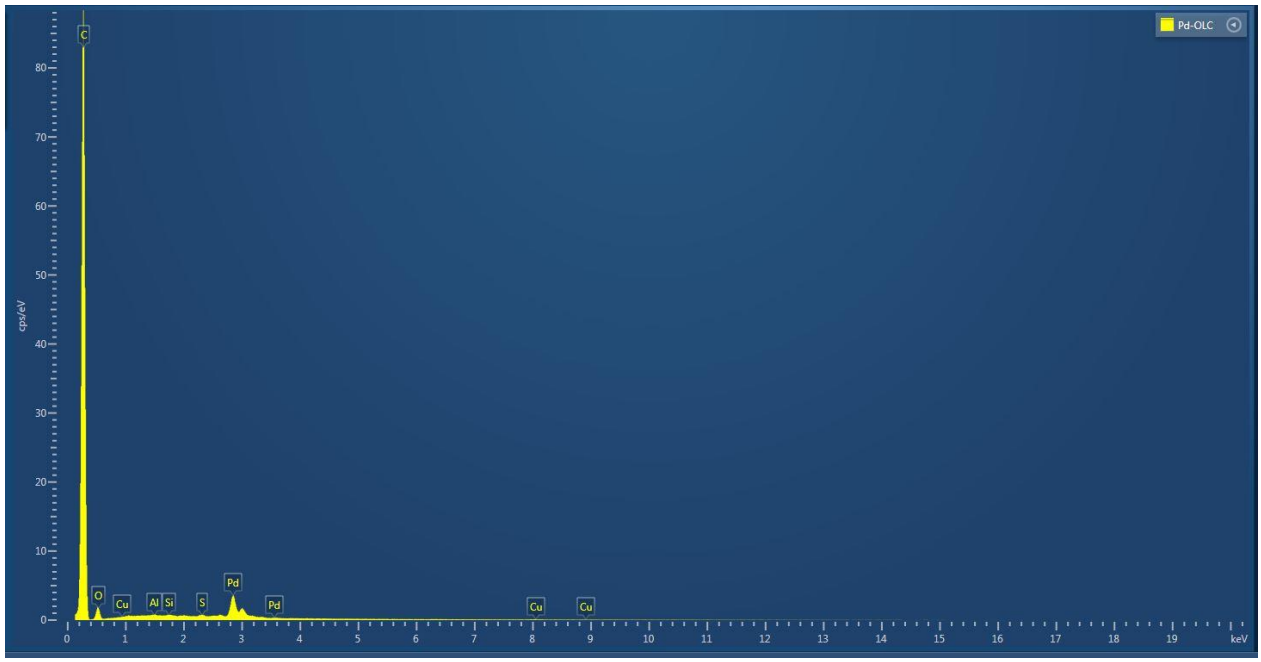


Figure 4.3(b). EDS spectrum of Pd/OLC

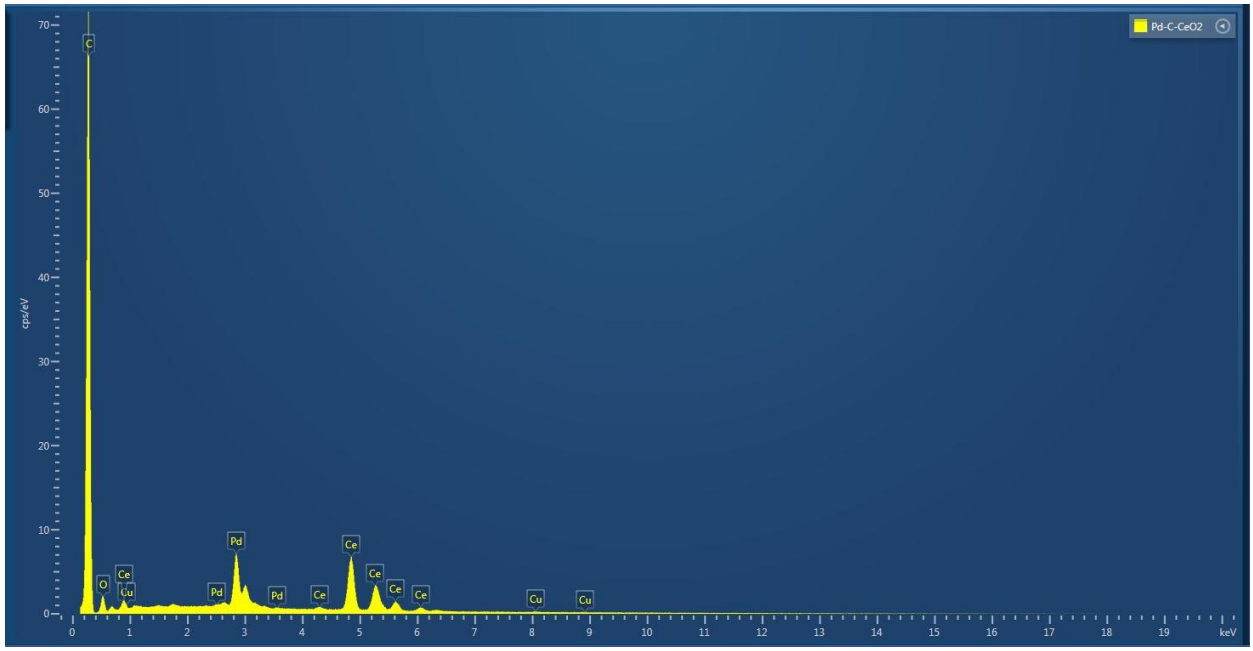


Figure 4.3(c). EDS spectrum of Pd-CeO_2/CB

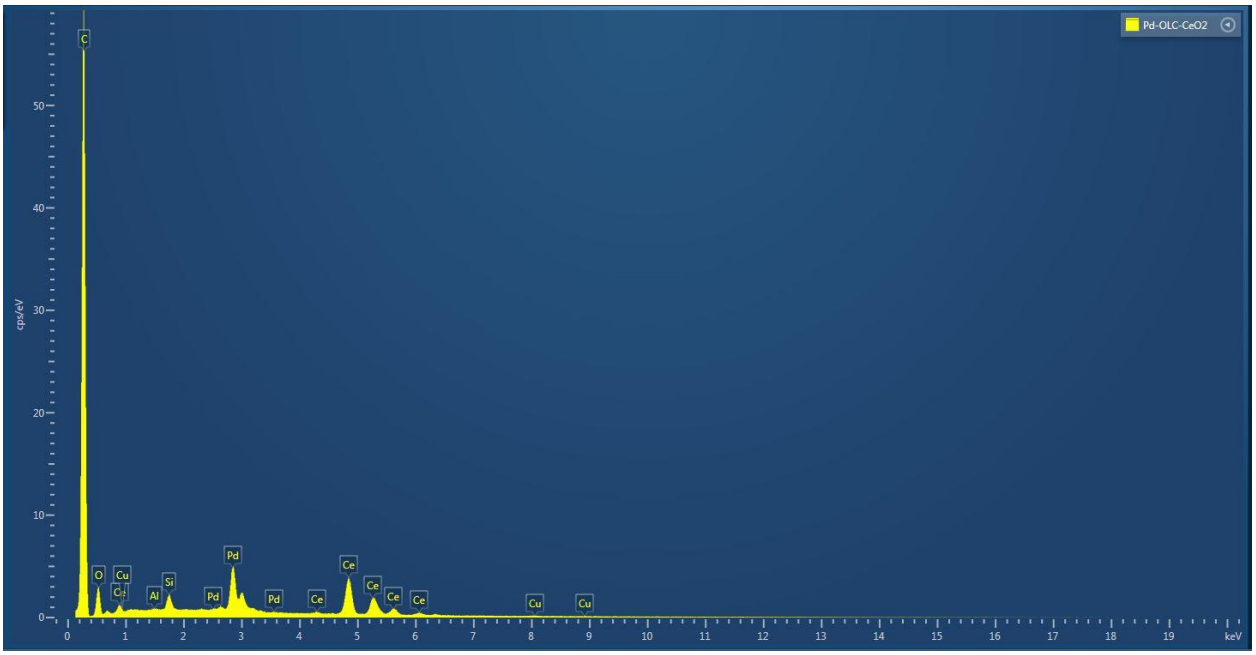


Figure 4.3(d). EDS spectrum of Pd-CeO_2/OLC

The SEM images show that the particles are spherical. The materials supported on OLC exhibit smaller particle sizes when compared to the materials supported on CB, leading to larger surface to volume ratio and thus larger surface areas. This suggests that the nano-sized structure of the OLC allows for better dispersibility of the catalysts.

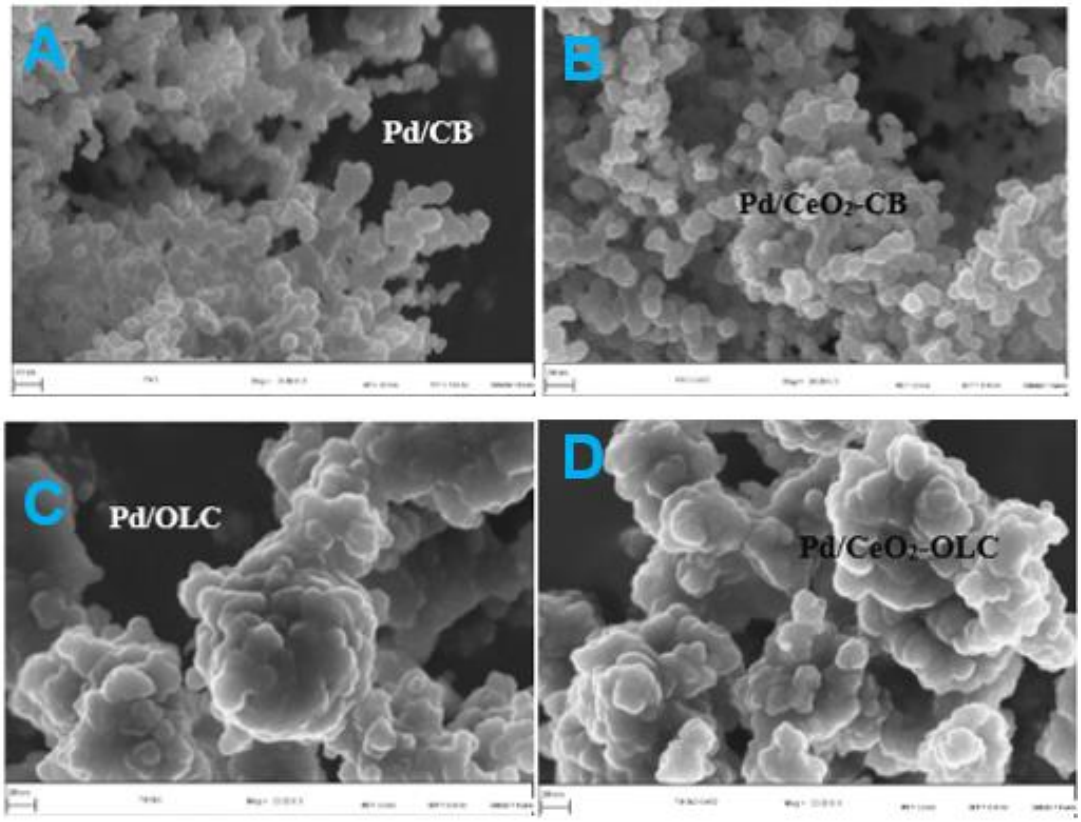


Figure 4.4: SEM images of (A) Pd/CB (B) Pd-CeO_2/CB (C) Pd/OLC and (D) Pd-CeO_2/OLC.

From the TEM images (at 500 nm), the mean particle sizes of the Pd/CB, Pd-CeO_2/CB, Pd/OLC and Pd-CeO_2/OLC were calculated to be 51.5 nm, 49.9 nm, 7.5 nm and 6.2 nm, respectively. The particle size distribution of each nanocatalyst is represented in **Figure 4.6**.

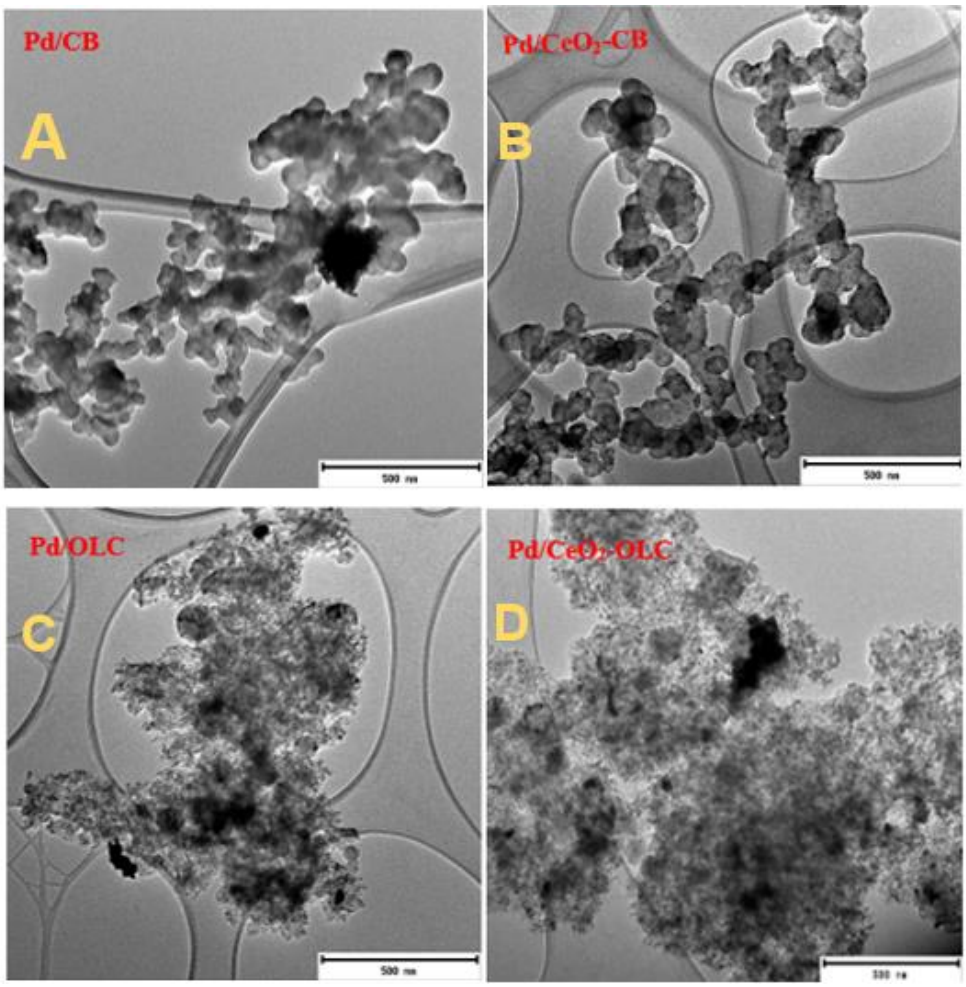


Figure 4.5: TEM images of (A) Pd/CB (B) Pd-CeO_2/CB (C) Pd/OLC and (D) Pd-CeO_2/OLC.

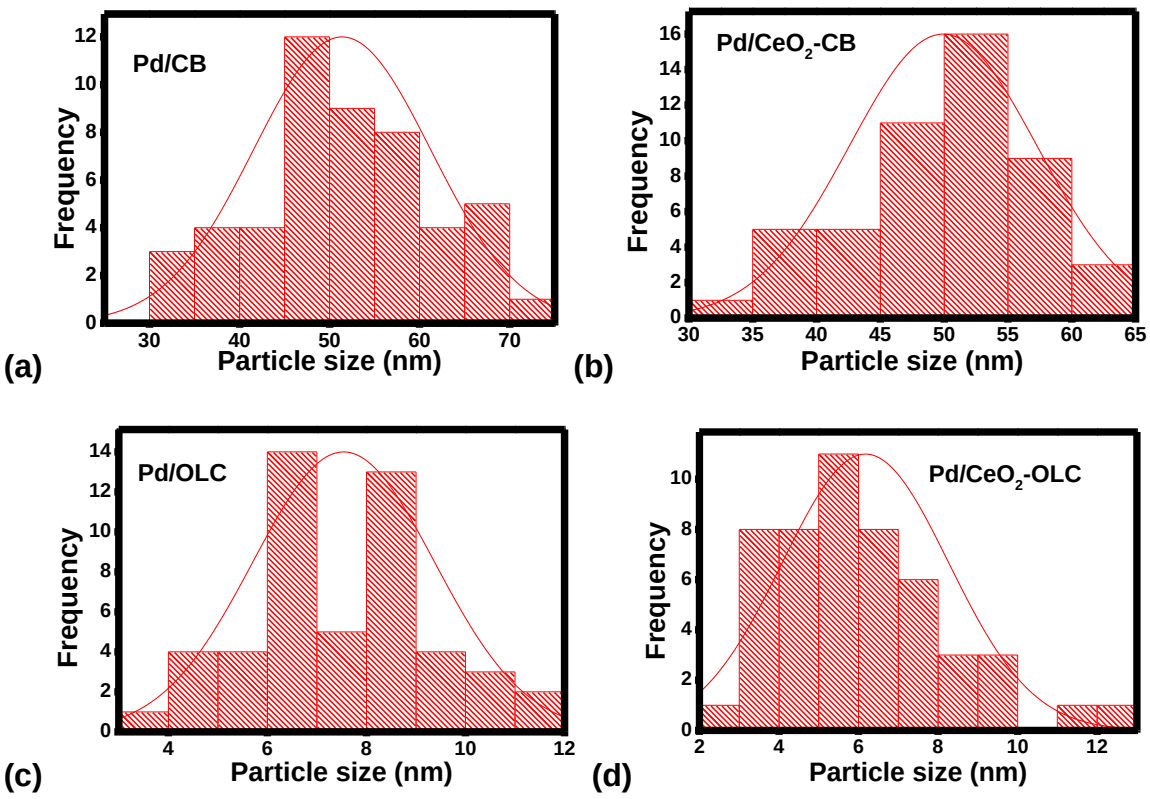


Figure 4.6: The particle size distribution of the nanocatalysts. (a) Pd/CB (b) Pd-CeO_2/CB (c) Pd/OLC (d) Pd-CeO_2/OLC.

4.1.4 High Resolution Transmission Electron Microscopy (HRTEM)

The HRTEM images of the samples are shown in **Figure 4.5** and the lattice fringes (obtained from ImageJ®) corresponding to Pd are determined to be 0.231 nm, 0.231 nm, 0.336 nm and 0.334 nm for Pd/CB, Pd/OLC, Pd-CeO_2/CB and Pd-CeO_2/OLC, which suggests that the lattice fringes expand with the addition of CeO_2. These d-spacing values are inconsistent with the d-spacing values from the XRD data. However, it is well-known that the HRTEM is more reliable for determining lattice spacing.

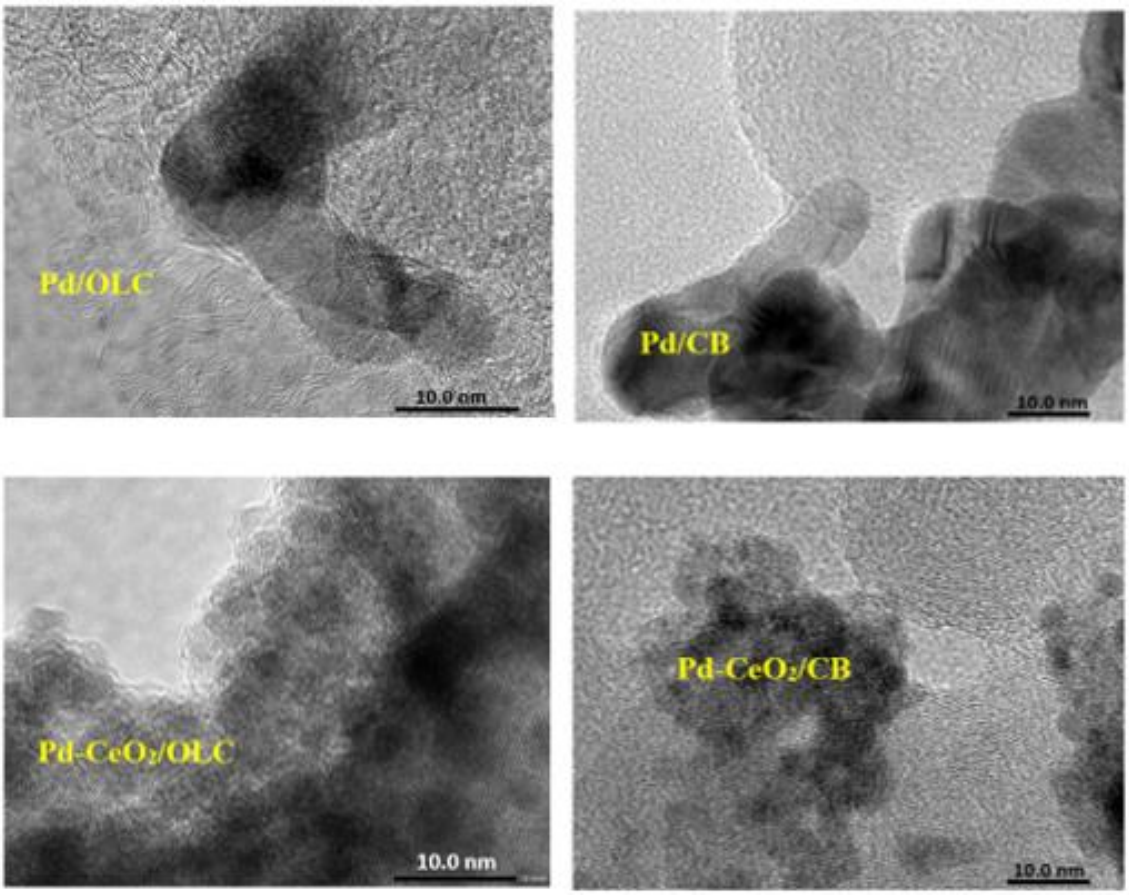


Figure 4.7: HRTEM images of the samples.

4.1.5 Thermogravimetric analysis of the nanocatalysts

From the thermal stability analysis of the nanomaterials studied, it was noted that the onset decomposition temperatures of Pd/CB, Pd-CeO_2/CB, Pd/OLC and Pd-CeO_2/OLC were at 516 °C, 380 °C, 457 °C and 252 °C, respectively (**Figure 4.8a**), and the first order derivative peaks were centered at 585 °C, 528 °C, 536 °C and 447 °C respectively (**Fig. 4.8b**).

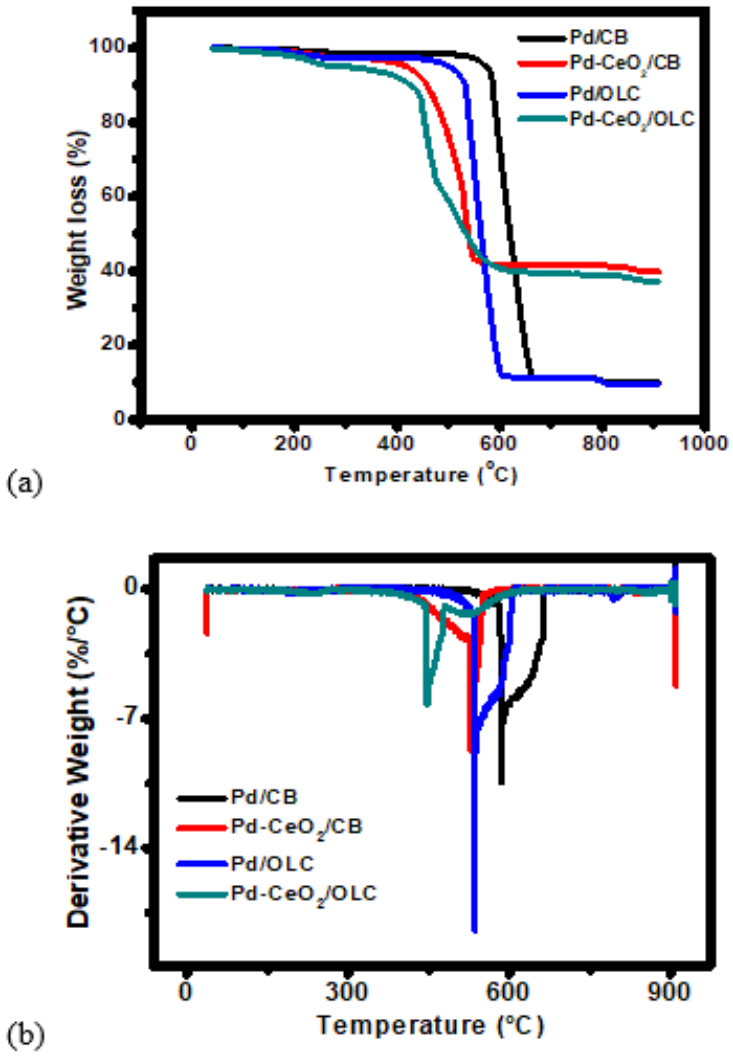


Figure 4.8: (a) TGA of the nanocatalysts; and the (b) Derivative Thermogravimetry (DTGA).

Pd/CB and Pd/OLC were observed to retain 10% of their weight, which accounts for the 10wt% Pd loading while Pd-CeO_2/CB and Pd-CeO_2/OLC retain ca. 40% of their weights which accounts for 10wt% Pd and Ce (C and O_2 burn off in inert environment).

4.1.6 Evaluation of surface area and pore volume of the samples

The surface area and pore volume of the nanocatalysts were investigated by BET analysis and are summarized in **Table 4.3** for the different catalysts.

Pd-CeO_2/OLC is observed to have the largest surface area, suggesting that it has a large amount of surrounding materials in contact and thus increases the interactions.

From the results, Pd-CeO_2/OLC also has the largest pore volume as compared to the other catalysts. Porosity is important for selective permeability, which is a property desired in the development of ion-exchange membrane.

Table 4.3: BET surface areas and porosity of the electrocatalysts

Electrocatalysts	Pore size / nm	Pore volume / cm3 g^{-1}	BET area / m^2 g^{-1}
Pd/CB	138.65	0.055	30.57
Pd-CeO_2/CB	59.71	0.089	87.07
Pd/OLC	2.53	0.225	357.73
Pd-CeO_2/OLC	2.47	0.230	373.53

4.1.7 X-Ray Absorption Spectroscopy (XAS)

Athena code was used to extract the EXAFS oscillations and Arthemis software was used in the analysis [21]. The amplitude reduction factor (S_0^2) and the photoelectron energy origin correction (ΔE_0) were found for the Pd foil and fixed for the samples as 0.8 and -6, respectively. The local environment of the Pd atoms were determined using the phase shift and amplitude functions of two Pd−O contributions and one Pd−Pd contribution.

The Pd-O contributions were calculated using a PdO with a tetragonal structure (CIF Collection Code 257583) and PdO with a cubic structure (CIF Collection Code

77650). The Pd-Pd contribution was calculated using a metallic Pd structure (CIF Collection Code 257579).

As a first attempt the coordination numbers (N_i), distances (R_i) and Debye-Waller factor (σ_i^2) of each path were adjusted freely and independently. However, the results for the σ_i^2 were very similar. Considering the N_i and σ_i^2 are strongly correlated parameters we opted to use the same σ_i^2 for all the paths but continue adjusting it freely. In addition, a second model was tested using a second Pd-Pd contribution instead of the longer Pd-O contribution in the second shell. This attempt was made to test the presence of small PdO particles in addition to the metallic particles. The model did not represent the data.

Table 4.4: Fit results of the EXAFS data.

	Pd-O contributions				Metallic Pd	
Sample	CN (Pd-O) 4*	R (Å) 2.04*	CN (Pd-O) 6*	R (Å) 2.83*	CN (Pd-Pd) 12*	R (Å) 2.78*
Pd/OLC	1.7 ± 0.6	2.04 ± 0.03	7 ± 2	3.02 ± 0.03	5 ± 1	2.76 ± 0.005
Pd-CeO_2/CB	1.7 ± 0.4	2.05 ± 0.02	8 ± 2	3.04 ± 0.02	4 ± 1	2.77 ± 0.01
Pd-CeO_2/OLC	1.7 ± 0.5	2.04 ± 0.02	8 ± 2	3.04 ± 0.001	6 ± 1	2.76 ± 0.01

CN, coordination number; R, bonding length; σ_i^2 0.001 ± 0.001.

The range used to transform the EXAFS oscillations ($k^2\ \chi(k)$) was 3-12 and the interval where the fit was performed was 1-3 Å. **Table 4.4** and **Figure 4.9A** present the fit results. **Figure 4.9B** presents the Pd/OLC fit and the contributions.

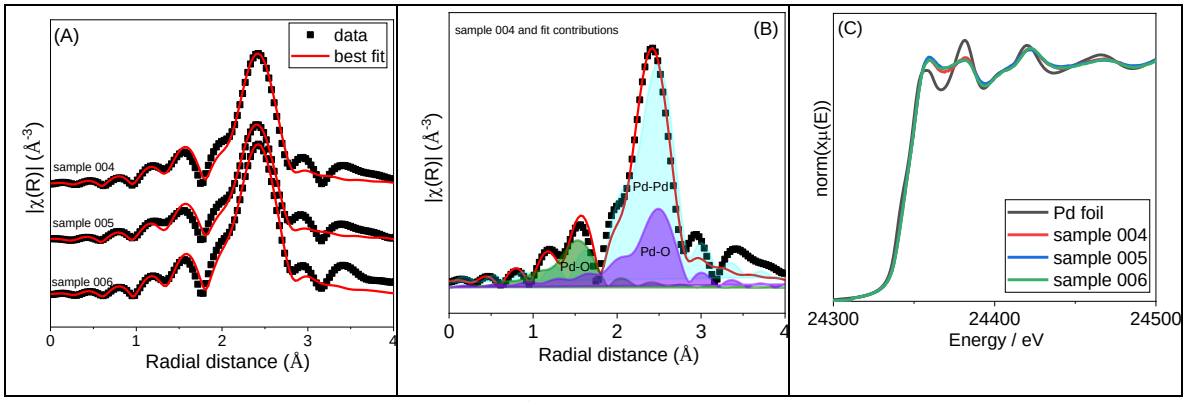


Figure 4.9. (A) Fourier transform of k^2-weighted spectrum (not phase corrected) and best fit for the samples Pd/OLC (sample 004), Pd-CeO_2/CB (sample 005) and Pd-CeO_2/OLC (sample 006). (B) Fourier transform, best fit and fit contributions for the sample Pd/OLC. (C) Normalized XANES spectra at Pd K-edge for all the samples and metallic reference.

All the samples are very similar with only a small difference in the Pd-Pd contribution. All the samples present, coordination numbers for the Pd-Pd contribution are much smaller than what is expected for metallic bulk Pd (12). The Pd particles dispersion increases in the order: Pd-CeO_2/OLC > Pd/OLC > Pd-CeO_2/CB.

The Pd-O contributions are very similar and indicate the presence of highly dispersed Pd species in addition to the small Pd particles. From the EXAFS analysis it is not possible to distinguish scattering from O, C and N. Thus, the Pd-O contributions could be in fact for example a Pd–C and Pd–O contributions. These contributions could come from an interaction with the carbon support, oxidation from the air or the reaction.

From the XANES results (**Figure 4.9C**) we can observe that the samples are very similar to Pd^0 but with damped oscillations, characteristic of nanomaterials.

4.1.8 X-ray Photoelectron Spectroscopy (XPS)

The chemical state of Pd and the atomic percentage of Pd^{2+} in the nanocomposites influence the performance of the catalyst [27,28].

A wide survey of the nanocatalysts (**Figure 4.10**) reveal the following constituent elements: Pd, Ce, O and C. To further investigate the chemical environments of the constituent elements, the high-resolution spectrum of each element was deconvoluted into two or more spectra.

The deconvoluted C1s spectra of the nanocatalysts (**Figure 4.11**), confirm the chemical environments of the carbon support. Pd/CB has C-C (sp2), C-O, C=O, O-C=O and C-C (sp3) bonds at 284.1, 286.1, 287.1, 288.7 and 285 eV, respectively and the Pd-CeO_2/CB has C-C (sp2), C-O, and C-C (sp3) bonds at 284.1, 285.7 and 285 eV, respectively.

Pd/OLC has C-C (sp2), C-O, C=O, O-C=O and C-C (sp3) bonds at 284.1, 285.79, 287.9, 288.80 and 285 eV, respectively whereas the Pd-CeO_2/OLC has C-C (sp2), C-O, C=O, O-C=O and C-C (sp3) bonds at 284.19, 285.79, 288.04, 288.80 and 285 eV, respectively.

The deconvoluted O 1*s* spectra of the nanocatalysts are shown in **Figure 4.12**. O 1s peaks can be seen at binding energies of 530.5, 532 and 533.2 for Pd/CB, attributed to metal oxide bonds, organic C-O bonds and C=O organic bonds, respectively. For Pd-CeO_2/CB, peaks can be seen at 529.8 eV, 531.9 eV, and 533.5 eV corresponding to metal oxide bonds, C-O organic bonds, organic and C=O bonds, respectively.

O 1s peaks can be seen at binding energies at 531.9 and 533.1 for Pd/OLC, attributed to the C-O organic bonds and organic C=O bonds, respectively. For Pd-CeO_2/OLC, O 1s peaks can be seen at 529.6 eV, 531.59 eV, 533.19 eV and 534.8

eV corresponding to metal oxide bonds, organic C=O bonds, C-O organic bonds, and organic O, respectively.

From the Pd 3d spectra (**Figure 4.13**), Pd/CB has peaks at 335.1 and 340.4 eV correspond to Pd(0) $3d_{5/2}$ and $3d_{3/2}$. The peak at 335.9 eV corresponds to Pd(II) $3d_{5/2}$ [29], while peaks at 337.7 and 342.8 eV are attributed to PdO_2 $3d_{5/2}$ and $3d_{3/2}$ satellite peaks, respectively.

For Pd-CeO_2/CB, the peaks corresponding to Pd(0) $3d_{5/2}$ and $3d_{3/2}$ are seen at 335.1 and 340.4 eV. While the peak at 336 eV is attributed to Pd(II) $3d_{5/2}$, the peaks at 337.5 and 342.7 are attributed to PdO_2 $3d_{5/2}$ and $3d_{3/2}$ satellite peaks, respectively.

For Pd/OLC, peaks corresponding to Pd(0) $3d_{5/2}$ and $3d_{3/2}$ are observed at 335.0 and 340.0 eV, peaks at 336.6 and 341.8 eV correspond to Pd(II) $3d_{5/2}$ and $3d_{3/2}$, respectively, and those at 338 and 343.2 eV are attributed to PdO_2 $3d_{5/2}$ and $3d_{3/2}$, satellite peaks respectively.

For Pd-CeO_2/OLC, the peaks at 335.2 and 340.4 eV are assigned to Pd(0) $3d_{5/2}$ and $3d_{3/2}$, while those at 337.4 and 342.6 eV are attributed to PdO_2 $3d_{5/2}$ and $3d_{3/2}$ satellite peaks, respectively.

From the spectra of Ce 3d in Pd-CeO_2/CB and Pd-CeO_2/OLC (**Figure 4.14**), the O1, O2, O3, O4, O5, O6 and O7 Ce (3d) signals are found at 882.4, 885.6, 898.8, 901.2, 903.4, 907.8 and 917.2 eV (for Pd-CeO_2/CB), and 882.4, 886, 898.6, 901, 903.4, 907.6 and 917 eV (for Pd-CeO_2/OLC).

The signals corresponding to Ce^{4+} $3d_{3/2}$ and Ce^{4+} $3d_{5/2}$ are observed at O7, O3 and O4, with binding energies of (917.2 eV) and (898.8 & 901.2 eV) respectively (for Pd-CeO_2/CB), and (917 eV) and (898.6 & 903.4 eV) respectively (for Pd-CeO_2/OLC). The oxygen vacancies (Ce^{4+}) may make for better dispersion of nanoparticles and also favor the catalysis [30].

The O5 and O1 energy levels of Ce^{3+} $3d_{3/2}$ and Ce^{3+} $3d_{5/2}$ are at 903.4 and 882.4 eV for both Pd-CeO_2/CB and Pd-CeO_2/OLC. Two extra satellite peaks O6 and O2 are shown at 907.8 eV (Pd-CeO_2/CB) and 907.6 (Pd-CeO_2/OLC) on the Ce^{3+} $3d_{3/2}$, and 885.6 eV (Pd-CeO_2/CB) and 886 eV (Pd-CeO_2/OLC) on the Ce^{3+} $3d_{5/2}$. These results are found to agree with previously reported spectra [59–63].

The valence band spectra of the Pd/CB, Pd/OLC, Pd-CeO_2/CB and Pd-CeO_2/OLC are represented in **Figure 4.15**. The d-band width of Pd/CB and Pd/OLC is 1.04 eV and 3.26 eV respectively. The d-band width increases to 3.60 eV and 9.00 eV for Pd-CeO_2/CB and Pd-CeO_2/OLC respectively. The broadening of the d-band suggests more compressive strain on the Pd lattice, causing an increase in the overlap of the electronic states between the metal atoms [31,32].

The constituent elements and their atomic content are summarized in **Table 4.5 (a-e)**.

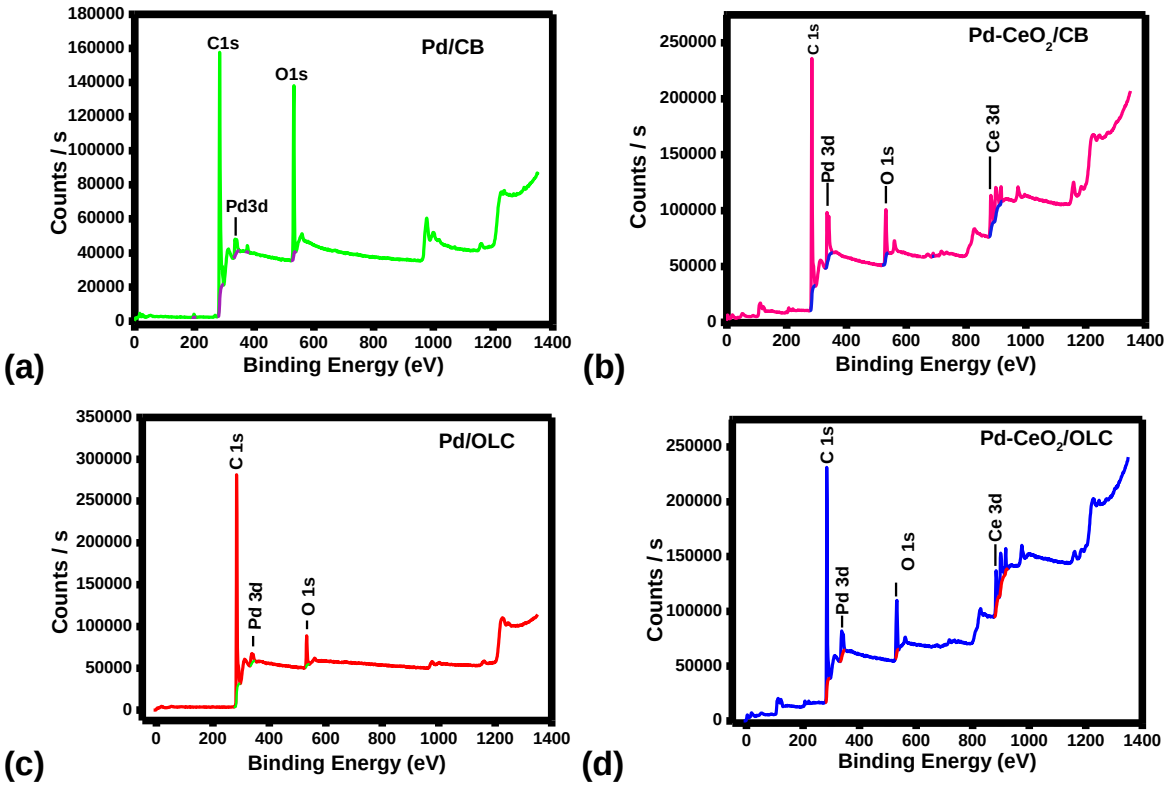


Figure 4.10: XPS of the (a) Pd/CB, (b) Pd-CeO_2/CB, (c) Pd/OLC and (d) Pd-CeO_2/OLC nanocatalysts.

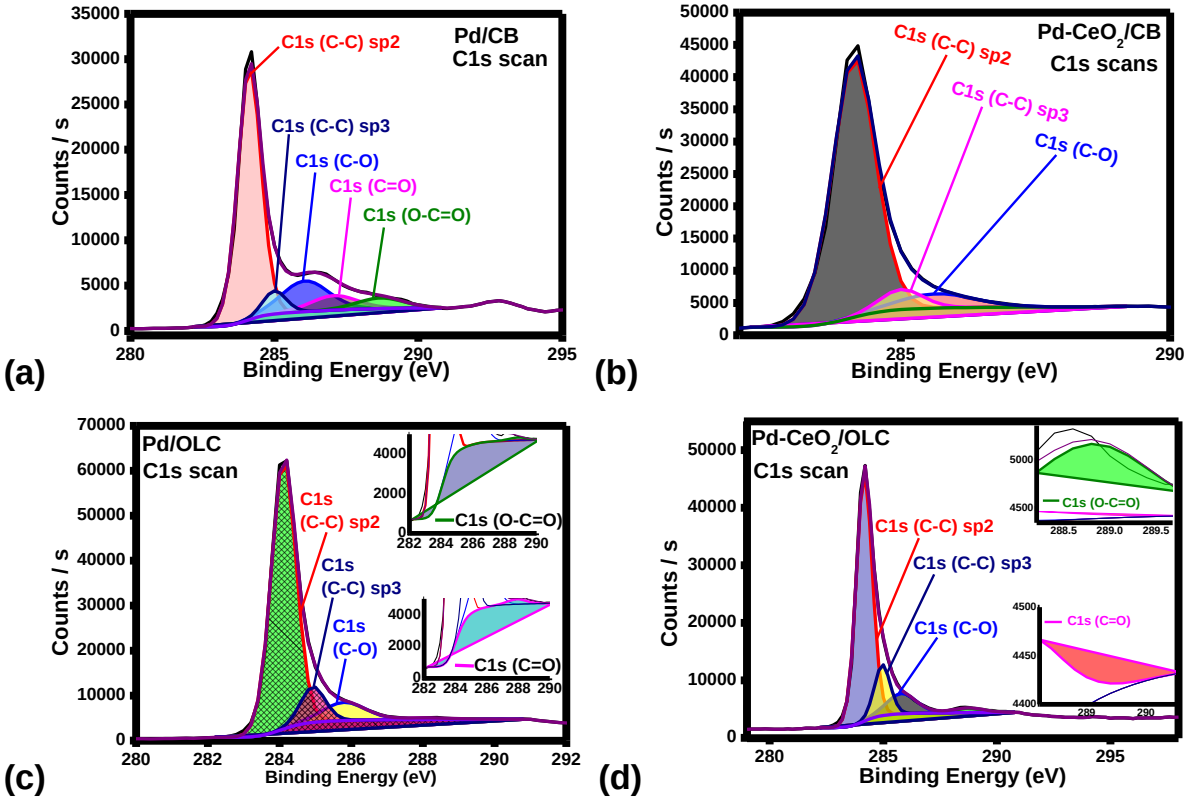


Figure 4.11: XPS C 1s scans of the (a) Pd/CB (b) Pd-CeO_2/CB (c) Pd/OLC and (d) Pd-CeO_2/OLC nanocatalysts.

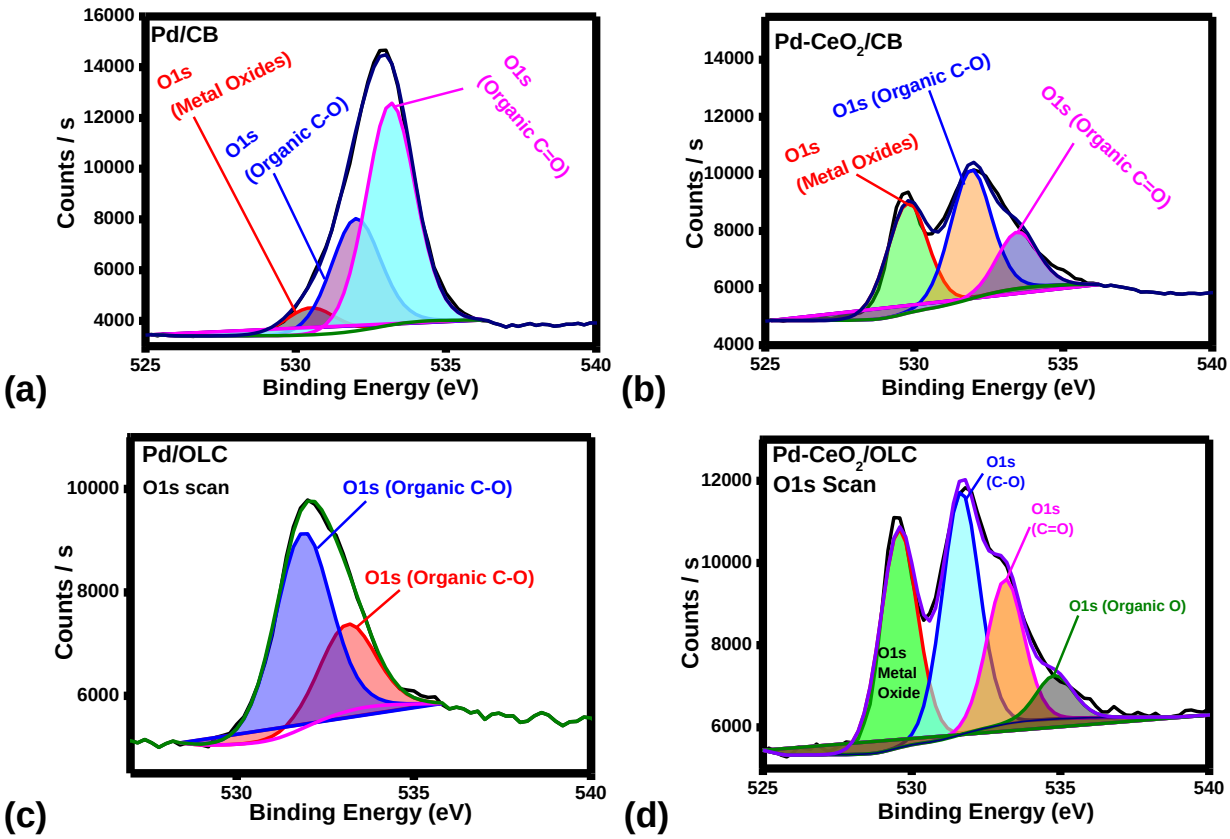


Figure 4.12: XPS O 1s scans of the (a) Pd/CB (b) Pd-CeO_2/CB (c) Pd/OLC and (d) Pd-CeO_2/OLC nanocatalysts.

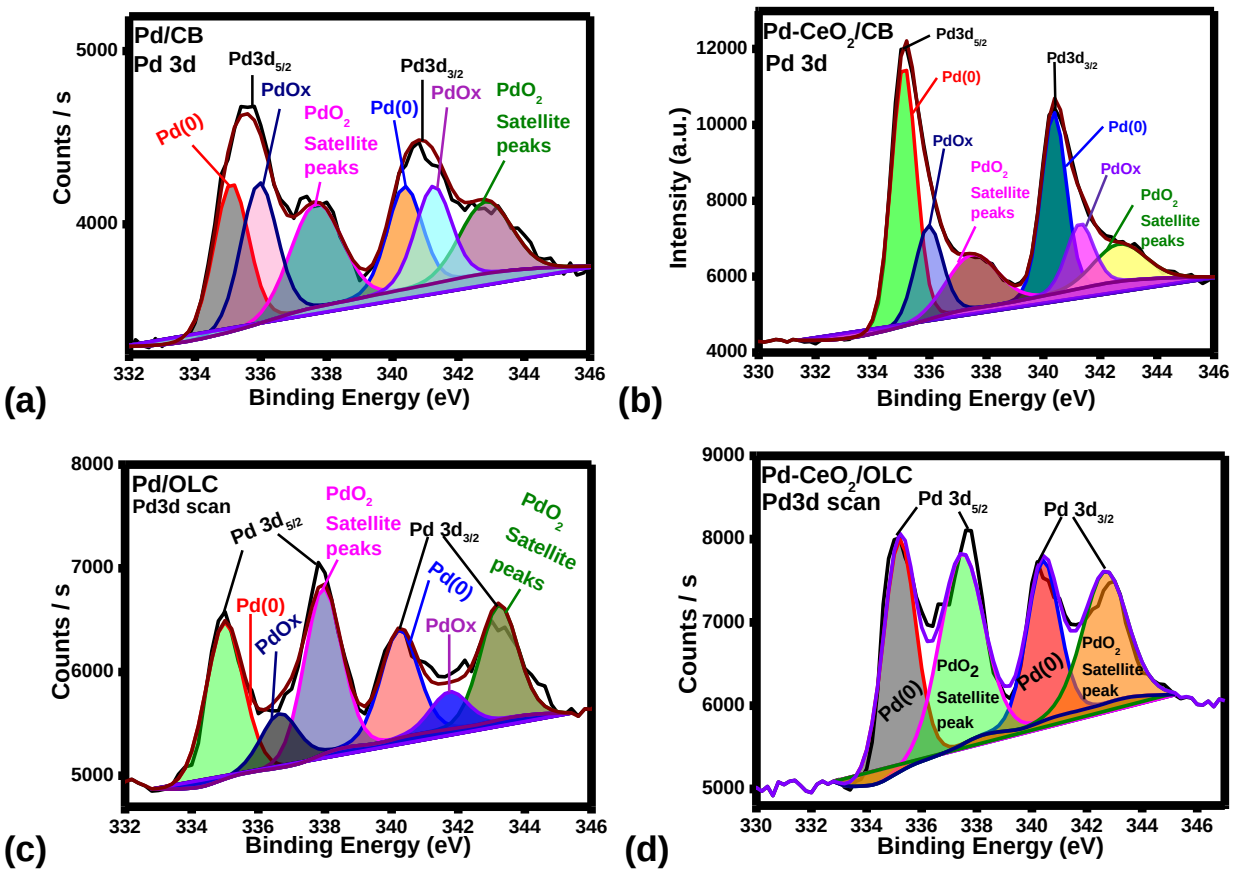


Figure 4.13: XPS Pd 3d scans of the (a) Pd/CB (b) Pd-CeO_2/CB (c) Pd/OLC and (d) Pd-CeO_2/OLC nanocatalysts.

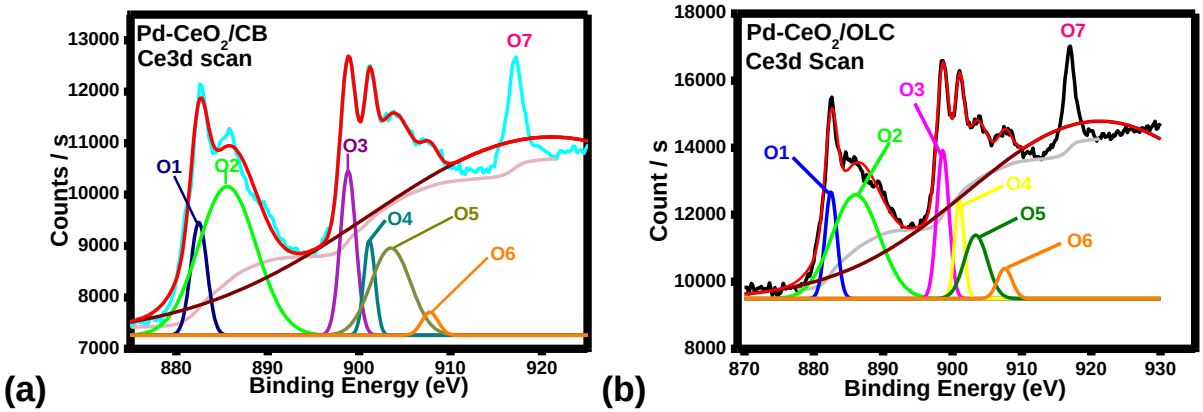


Figure 4.14: XPS Ce 3d scans of the (a) Pd-CeO_2/CB and (b) Pd-CeO_2/OLC nanocatalysts.

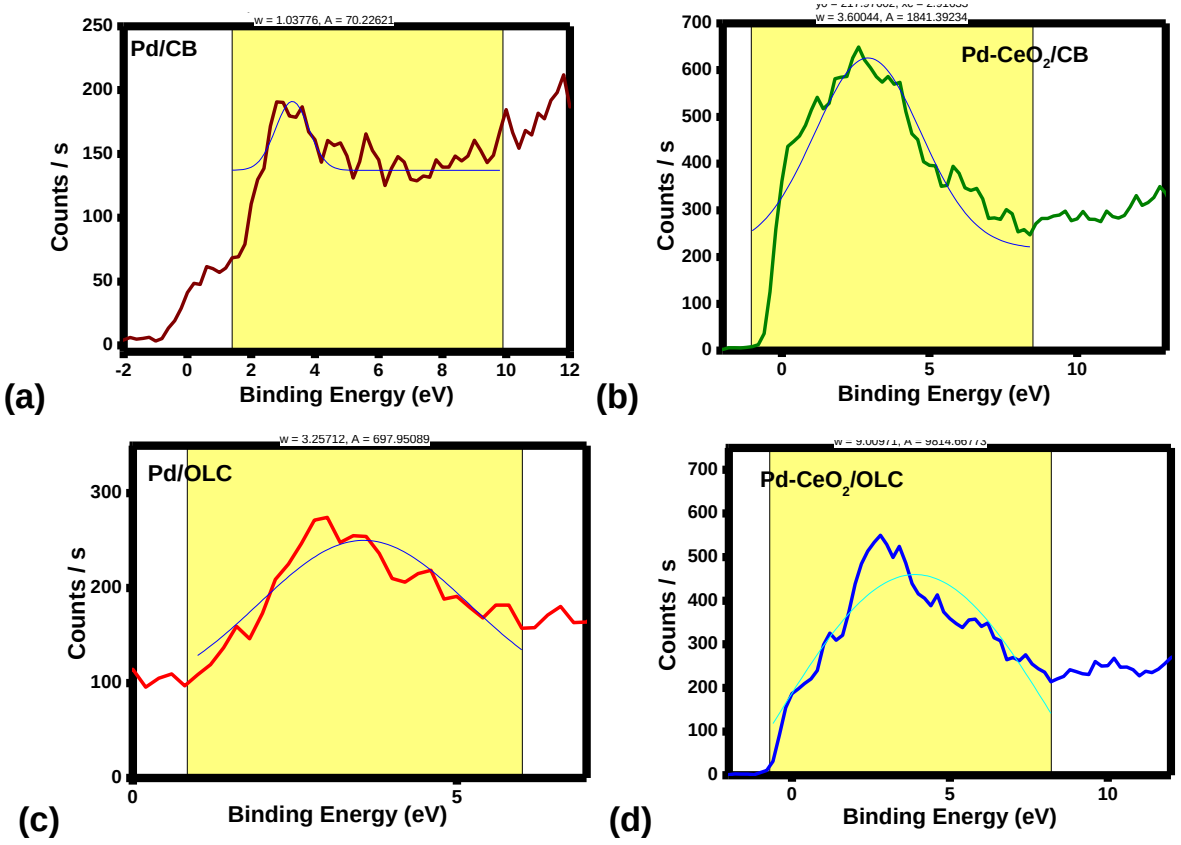


Figure 4.15: Valence band spectra of the (a) Pd/CB (b) Pd-CeO_2/CB (c) Pd/OLC and (d) Pd-CeO_2/OLC nanocatalysts.

Table 4.5 a: XPS atomic percentage of each constituent element.

Samples	Atomic %			
	Pd 3d	Ce3 d	C1s	O1s
Pd/CB	0.5	-	79.9	18.1
Pd-CeO_2/CB	2.2	1.3	85.4	10.7
Pd/OLC	0.6	-	93.5	5.9
Pd-CeO_2/OLC	1.2	1.6	84.6	12.6

Table 4.5 b: Elemental identification of Pd/CB

Name	Peak BE	FWHM eV	Atomic %	Q
C1s (C-C) sp2	284.1	1	50.6	1
C1s (C-C) sp3	285	1	4.6	1
C1s (C-O)	286.1	1.9	12.4	1
C1s (C=O)	287.1	1.9	5.8	1
C1s (O-C=O)	288.7	1.9	4.3	1
Pd3d5 (Pd)	335.1	1.3	0.2	1
Pd3d5 (PdOx)	335.9	1.3	0.2	1
Pd3d5 (PdO_2; Satellite peaks)	337.7	1.8	0.2	1
Pd3d3 (Pd)	340.4	1.3	0.2	1
Pd3d3 (PdO_2; Satellite peaks)	342.8	1.8	0.2	1
O1s (Metal Oxides)	530.5	1.9	1.4	1
O1s (Organic C-O)	532	1.9	6	1
O1s (Organic C=O)	533.2	1.9	11.9	1

Table 4.5 c: Elemental identification of Pd-CeO_2/CB

Name	Peak BE	FWHM eV	Atomic %	Q
C1s (C-C) sp2	284.1	0.9	69.9	1
C1s (C-C) sp3	285	1	5.4	1
C1s (C-O)	285.7	1.7	6.8	1
Pd3d5 (Pd)	335.1	1	1.2	1
Pd3d5 (PdOx)	336	1.1	0.5	1
Pd3d5 (PdO_2; Satellite peaks)	337.5	2.1	0.5	1
Pd3d3 (Pd)	340.4	1	1.2	1
Pd3d3 (PdO_2; Satellite peaks)	342.7	2.1	0.5	1
O1s (Metal Oxides)	529.8	1.6	4.3	1
O1s (Organic C-O)	531.9	1.6	5	1
O1s (Organic C=O)	533.5	1.6	2.2	1
Ce3d (CeO2)	883	6.5	1.9	1

Table 4.5 d: Elemental identification of Pd/OLC

Name	Peak BE	FWHM eV	Atomic %	Q
C1s (C-C) sp2	284.1	0.8	73.6	1
C1s (C-C) sp3	284.9	0.8	9.7	1
C1s (C-O)	285.1	1.4	8.7	1
C1s (C=O)	287.9	1.4	0.7	1
C1s (O-C=O)	288.8	1.4	0.3	1
Pd3d5 (Pd)	335.0	1.3	0.3	1
Pd3d5 (PdOx)	336.6	1.3	0.1	1
Pd3d5 (PdO_2; Satellite peaks)	337.9	1.3	0.3	1
Pd3d3 (Pd)	340.2	1.3	0.3	1
Pd3d5 (PdOx)	341.97	1.3	0.1	1
Pd3d3 (PdO_2; Satellite peaks)	343.2	1.3	0.3	1
O1s (Organic C-O)	531.9	1.9	3.9	1
O1s (Organic C=O)	533.1	1.9	1.7	1

Table 4.5 e: Elemental identification of Pd-CeO_2/OLC

Name	Peak BE	FWHM eV	Atomic %	Q
C1s (C-C) sp2	284.2	0.8	58.3	1
C1s (C-C) sp3	285	0.8	12.0	1
C1s (C-O)	285.8	1.5	8.9	1
C1s (C=O)	287.9	1.5	0.3	1
C1s (O-C=O)	288.8	1.5	2.0	1
Pd3d5 (Pd)	335.2	1.4	0.6	1
Pd3d5 (PdO_2; Satellite peaks)	337.4	1.9	0.6	1
Pd3d3 (Pd)	340.4	1.4	1.4	1
Pd3d3 (PdO_2; Satellite peaks)	342.6	1.9	0.6	1
O1s (Metal Oxides)	529.6	1.5	4.8	1
O1s (Organic C-O)	531.6	1.5	5.3	1
O1s (Organic C=O)	533.1	1.5	3.2	1
O1s (Organic O)	534.8	1.5	1.0	1
Ce3d (CeO2)	882.7	2.8	1.9	1

4.1.9 Electrode Surface Coverage Analysis

The surface coverage analysis of the bare GCE and electrocatalyst-modified GCE was performed in a solution of 0.1 M KCl containing 3 mM $Fe(CN)_6]^{4-}$/$[Fe(CN)_6]^{3-}$ solution.

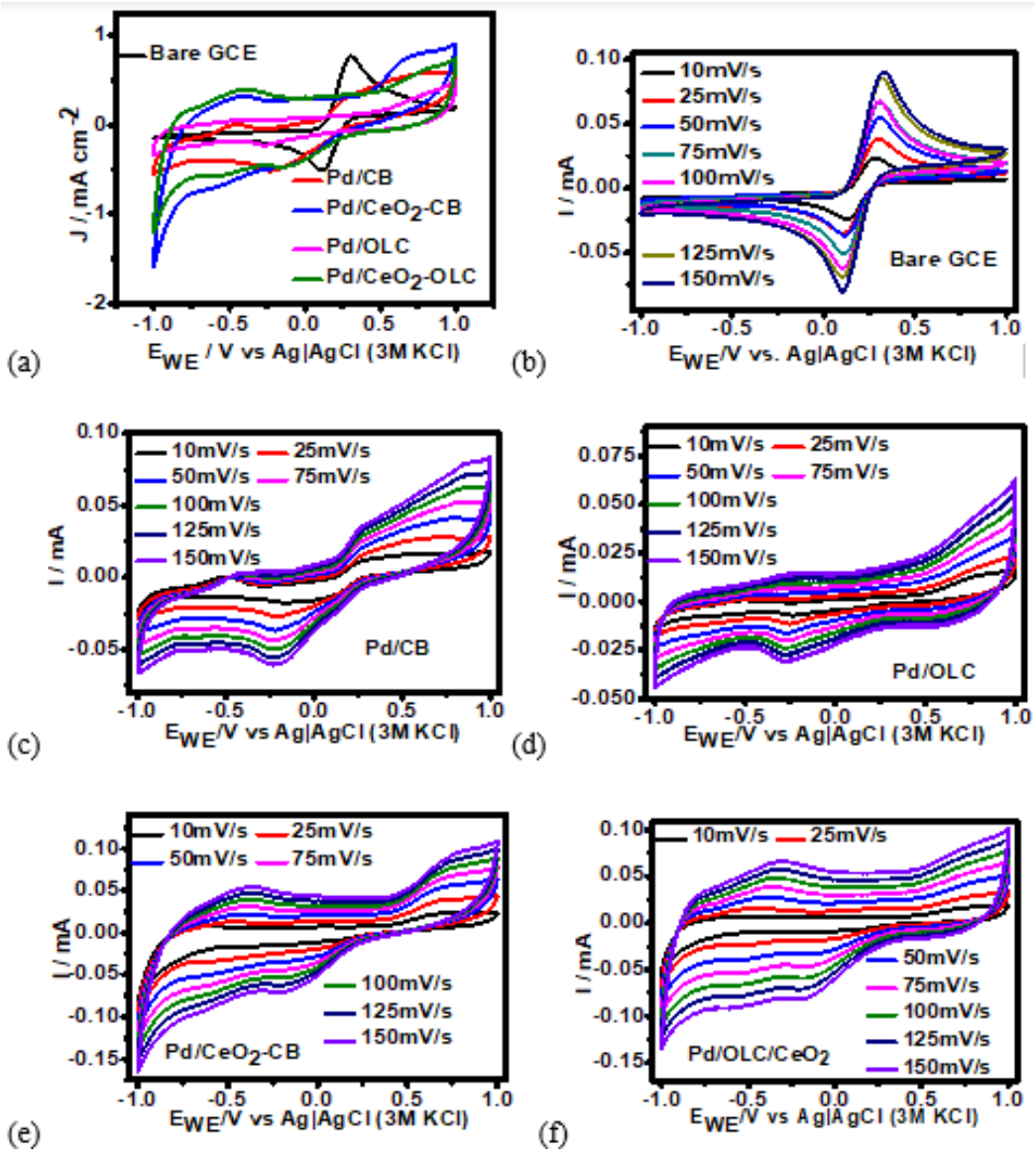


Figure. 4.16: Cyclic voltammograms of the bare and modified GCE.

In **Figure 4.16a** the CVs of the bare and modified GCE are compared. The bare GCE clearly showed the $Fe(CN)_6]^{4-}/[Fe(CN)_6]^{3-}$ redox process at an equilibrium potential ($E_{1/2}$) of about 0.19 V. The value of the peak separation potential (ΔEp) (≈ 191.5 mV) exceeds the theoretical 59.8 mV for a fast one-electron transport. The anodic to the cathodic peak ratios (I_{pa}/I_{pc}) for the electrodes are ≈ 1, which is an indication that the electrochemical process is reversible.

Unlike the unmodified GCE, there was no significant electrochemical response observed after scanning the GCE modified with each of Pd/CB, Pd/OLC, Pd-CeO_2/CB and Pd-CeO_2/OLC in the ferri/ferro solution. This indicates that the activity of the modified GCE had been lost completely due to the existence of palladium complex - mainly in the form of Pd^{IV} complexes - on the GCE surface [5], making it difficult to determine the electron transfer rate at the modified electrodes.

The electrodes were also studied at different scan rates (**Figure 4.16 b-f**). The redox peaks increased with increasing scan rates.

4.2 Ethanol Oxidation Reaction (EOR)

The EOR was performed using a three-electrode (half-cell) system comprising of a GCE (diameter = 3 mm) as the WE, platinum wire as the CE (to generate applied potentials at the working electrode), and Ag|AgCl electrode (3 M KCl) as the RE (to monitor the current generated at the working electrode).

The GCE was cleaned by proper polishing on a polishing pad using alumina (Al_2O_3) slurry followed by ultrasonic stirring in ethanol and acetone.

The catalyst ink was prepared by dispersing the powder (1 mg) in ethanol (1 mL) and adding 100uL of Nafion (5 wt%) to increase the adhesion of the catalyst material on the glassy carbon electrode. The mixture was sonicated for 30 minutes to obtain a homogeneous mixture. The catalyst ink (12 uL) was then deposited on the GCE in

a dropwise fashion and allowed to dry, producing an electrocatalyst loading of 0.00144 mg cm^{-2}.

The following catalyst-modified GCE electrodes were studied: (1) Pd/CB (2) Pd-CeO_2/CB (3) Pd-CeO_2/OLC (4) Pd/OLC catalysts. The electrochemical behaviour of each catalyst was investigated using CV, LSV, CA, and EIS.

4.2.1 Cyclic Voltammetry (CV)

CV was performed on each of the the Pd/CB, Pd/OLC, Pd-CeO_2/CB and Pd-CeO_2/OLC electrodes in pure N_2-saturated 0.5M KOH. The voltammograms are shown in **Figure 4.17**. Hydrogen adsorption/desorption peaks and Palladium Oxide (PdO) reduction peaks are observed between (-0.4 and -1.00 V) and (-0.26 and -0.35 V) vs Ag|AgCl (3 M KCl), respectively for all the electrocatalysts [8,9,13].

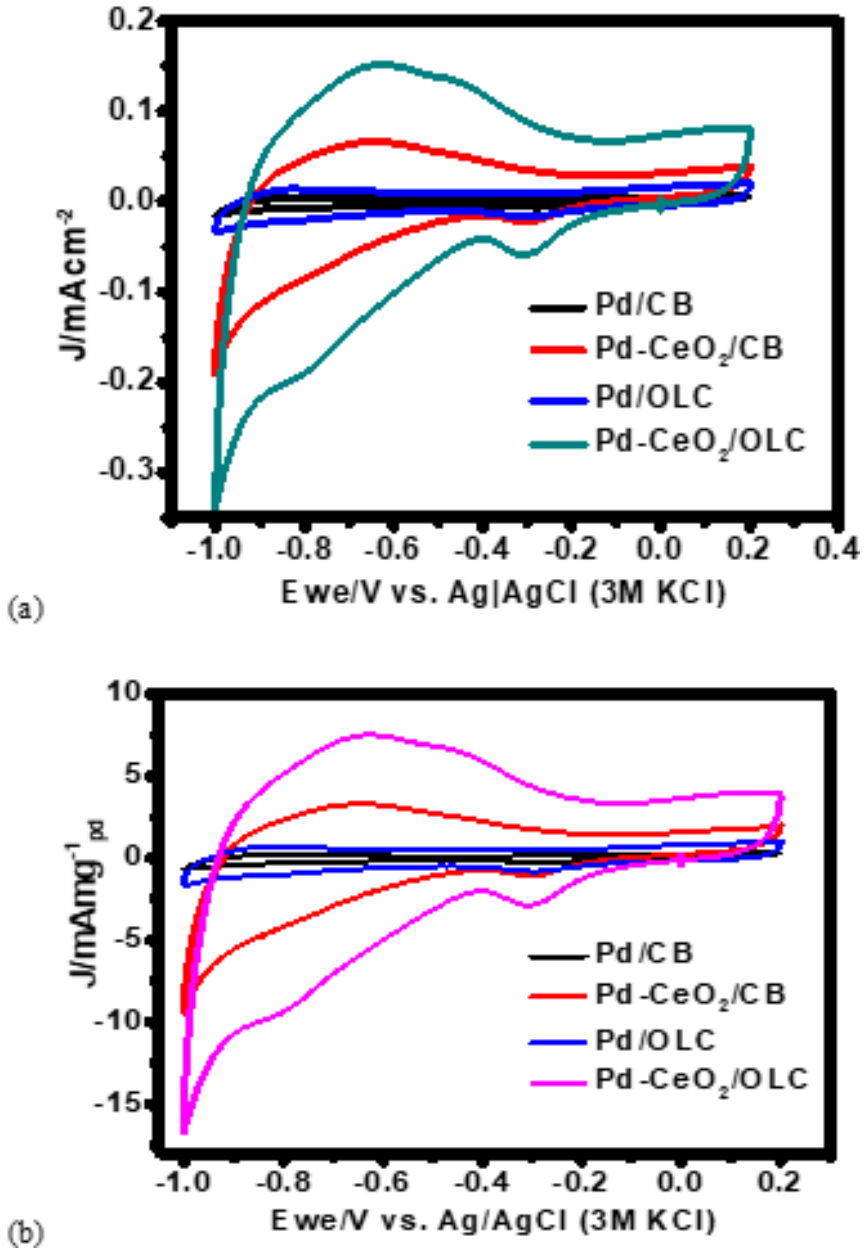


Figure 4.17: Cyclic voltammograms of Pd/CB, Pd/OLC, Pd-CeO_2/CB and Pd-CeO_2/OLC (a) Specific activity (b) Mass activity.

The current densities of the hydrogen adsorption/desorption peaks are much higher for the electrocatalysts on CeO_2 support than those supported on carbon alone.

Pd−CeO_2/OLC shows the highest PdO reduction peak around -0.30 V vs Ag/AgCl electrode.

The PdO reduction peaks of the catalysts containing CeO_2 shift to a more positive potential, which is an indication that less energy is needed to reduce PdO in the presence of CeO_2, which is possibly due to the attraction of Pd to metal oxides like CeO_2, which provide more oxygen to the Pd and PdO active sites [9]. The electrochemical active surface area $(ECSA)_{PdO}$ was estimated by integrating the PdO reduction peaks to find the Coulombic charge of each catalyst and then following the proposed method of Rand and Wood [19] (**Equation 4.3**).

$$ECSA = \frac{Q}{S.l} \qquad \textbf{4.3}$$

where ***Q*** is the coulombic charge (0.1662, 0.4054, 0.4498, and 0.8718 mC for Pd/CB, Pd-CeO_2/CB, Pd/OLC, and Pd-CeO_2/OLC, respectively), ***S*** is the coulombic constant for monolayer of Pd (0.424mC cm^{-2}), and ***l*** is the electrocatalyst loading (~ 1.0 µg(Pd)). The $ECSA_{PdO}$ values for the catalysts are recorded in **Table 4.6**.

The $ECSA_{PdO}$ of Pd/OLC, Pd-CeO_2/CB, and the Pd/CB catalysts are 88.404, 76.678, and 32.666 $m^2 g_{Pd}^{-1}$, respectively. In comparison, Pd−CeO_2/OLC shows the highest $ECSA_{PdO}$ of 171.344 $m^2\ g_{Pd}^{-1}$, which is 1.94, 2.23, and 5.25 times higher than that of Pd/OLC, Pd-CeO_2/CB, and Pd/CB respectively. The high $ECSA_{PdO}$ of Pd−CeO_2/OLC shows that more catalytic active sites of Pd are exposed after combining with the OLC/CeO_2 heterostructure. The difference in the values of the BET and ECSA is because while BET probes the entire surface area available to N_2 gas, including the meso- and macropores, the active surface area results from the chemical reaction between the electrode and electrolyte and would be different.

The electrocatalysts were then explored for EOR using CV in 0.5 M ethanol/0.5 M KOH at a sweep rate of 50 mV s^{-1} (**Figure 4.18**), giving rise to two peaks (arising from the forward and backward scans), typical of ethanol oxidation. The peak arising

from the forward scan is attributed to the oxidation of the carbonaceous species adsorbed onto the electrocatalyst surface, while the reverse oxidation peak from the backward scan shows the re-oxidation of the carbonaceous species to CO_2 or CH_3COOH [9].

The peak currents were normalized over the ECSA and loading of catalyst to obtain the specific activity and mass activity, respectively. The forward peak current density of mass activity (658.53 mA mg^{-1}) on Pd -CeO_2/OLC is about 3.59 times that of Pd/OLC (183.28 mA mg^{-1}), 5.44 times that of Pd-CeO_2/CB (120.93 mA mg^{-1}) and 15.38 times that of Pd/CB (42.83 mA mg^{-1}).

The onset potential gives information regarding the ease of electrocatalysis. A more negative value (i.e., an earlier onset potential) indicates easier electrocatalysis [6]. The onset potential of the EOR of each electrocatalyst is recorded in **Table 4.6**. Addition of CeO_2 to Pd-carbon catalysts is observed to significantly enhance the onset potential (shifting it to a more negative value) and significantly increase the EOR current densities.

The onset potential (E_{onset} [V]) and peak separation (ΔE_p [V]) from the cyclic voltammograms decrease as follows: Pd/CB (@0.626V, 0.095V) > Pd/OLC (@0.652V,0.094V) > Pd-CeO_2/CB (@0.656V,0.088V) > Pd-CeO_2/OLC (@-0.692V, 0.067V). This suggests that the CeO_2 in Pd-CeO_2/CB and Pd-CeO_2/OLC noticeably improve the EOR performance.

From the voltammograms, it is clearly observed that the Pd/CeO_2-OLC showed the best ethanol oxidation activity (lower overpotential and higher current response) in this research.

The forward peak current density (*j*f) gives information about the catalyst's maximum current generation; and the *j*f/*j*b gives information about the tolerance ability of the catalyst to carbonaceous species accumulated (a higher *j*f/*j*b value signifies better tolerance of the catalyst to poisoning) [7].

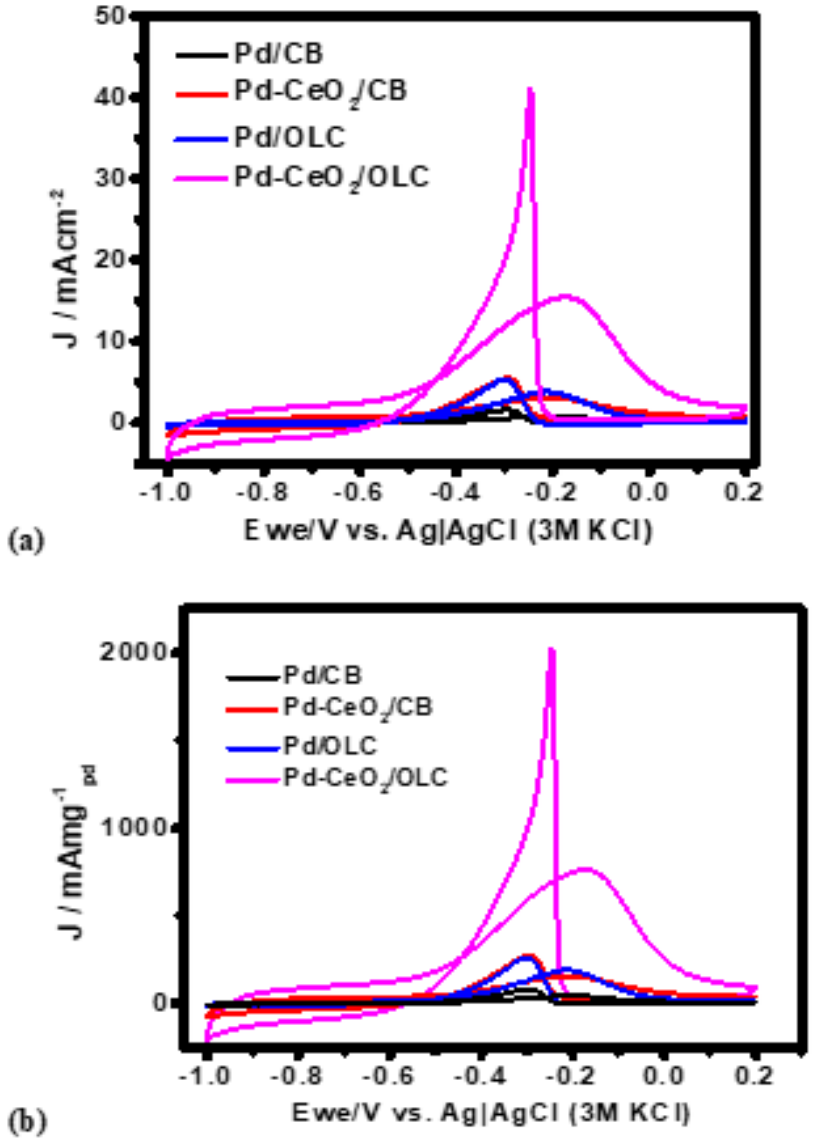


Figure 4.18: Cyclic voltammograms of the EOR of the electrocatalysts (a) Specific activity (b) Mass activity

Table 4.6: EOR data obtained at the Pd/CB, Pd-CeO_2/CB, Pd/OLC and Pd-CeO_2/OLC electrodes.

Specific Activity							**Mass Activity**	
Sample	***ECSA*** $(cm^2\ mg^{-1})$	E_{onset} **(V)**	ΔE_p **(V)**	J_f (mA/cm^2)	J_b (mA/cm^2)	J_f/J_b	J_f (mA/mg_{Pd})	J_b (mA/mg_{Pd})
Pd/CB	32.665	-0.626	0.095	0.864	1.660	0.521	59.903	109.538
Pd/CeO_2-CB	76.678	-0.656	0.088	2.440	5.199	0.469	239.934	345.551
Pd/OLC	88.404	-0.652	0.094	3.693	5.406	0.683	243.037	352.706
Pd/CeO_2-OLC	171.344	-0.692	0.067	12.975	39.666	0.327	845.991	2 624.063

Table 4.7: Electrocatalytic properties of the Pd-CeO_2/OLC electrocatalyst towards EOR in alkaline media compared to other works (*n/a* not available).

Electocatalyst	**Electrolyte**	**ECSA (cm^2/mg)**	**E_{onset} (V)**	**ΔE_p (V)**	**J_f (mA/cm^2)**	**J_f/J_b**	**Ref**
Pd-CeO_2/OLC	0.5 M KOH + 0.5 M EtOH	171.344	-0.692	0.067	12.975	0.33	This work
Pd/SnO_2/MOFDC	0.25 M EtOH/0.25 M KOH	962.0	− 0.650	0.084	7.303	0.80	[9]
Pd/Ni/CeO/C	1.00 M EtOH/1.00 M KOH	*n/a*	− 0.40	*n/a*	3.3	0.80	[64]
MWCNT/$PdSn_{mix}$	0.50 M EtOH/0.50 M KOH	604	− 0.50	0.250	6.87	0.65	[65]
Pd/Cu/graphene	1.00 M EtOH/1.00 M KOH	202.2	− 0.58	0.220	1.94	2.98	[66]

Figure 4.19 shows CVs obtained at different scan rates. The forward ethanol oxidation peak current density is observed to be directly proportional to the scan rate.

The plot of the current density against the square root of the scan rates (**Figure 4.20**) gives linear plots, which is an indication of a diffusion-controlled interaction between the electrocatalysts and ethanol.

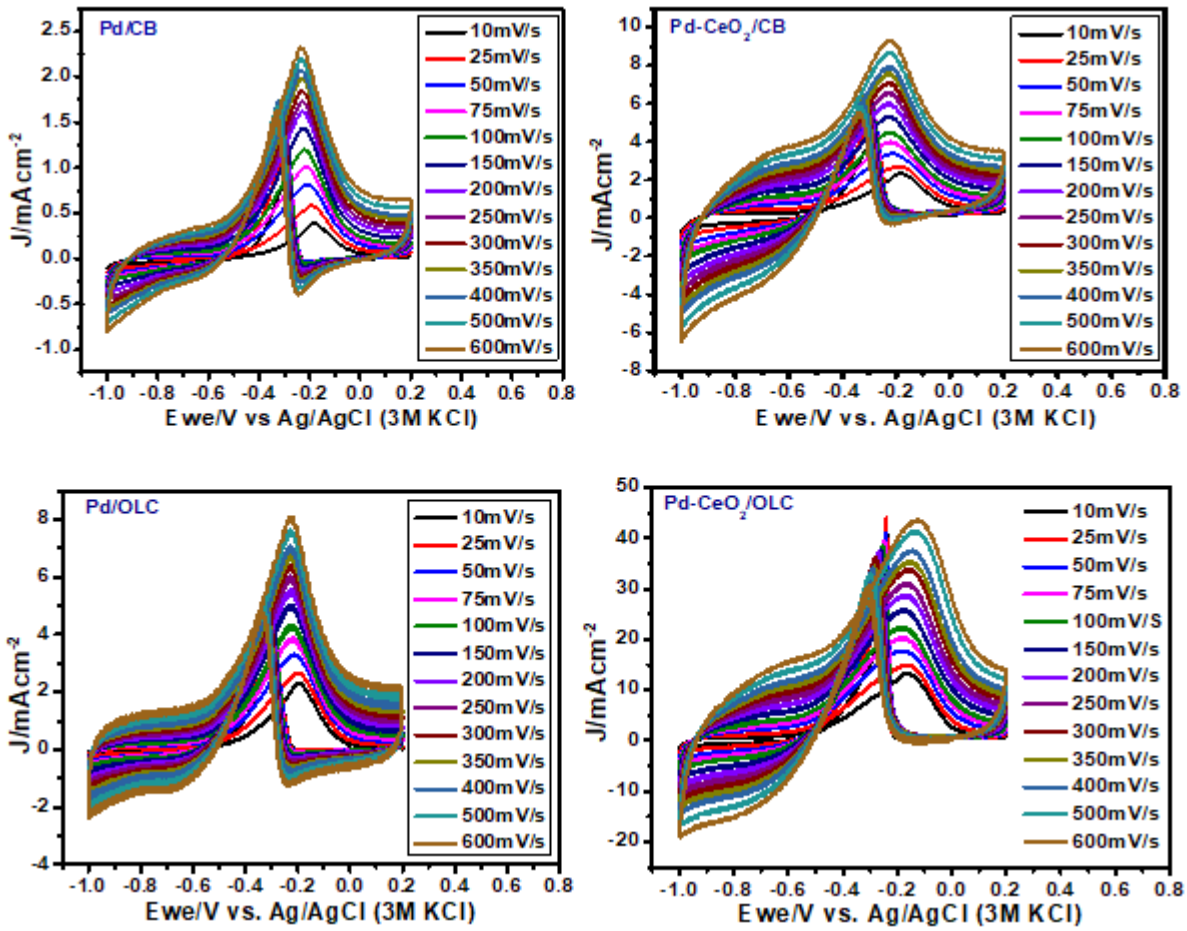


Figure 4.19: Scan rate studies of the Pd-based catalysts.

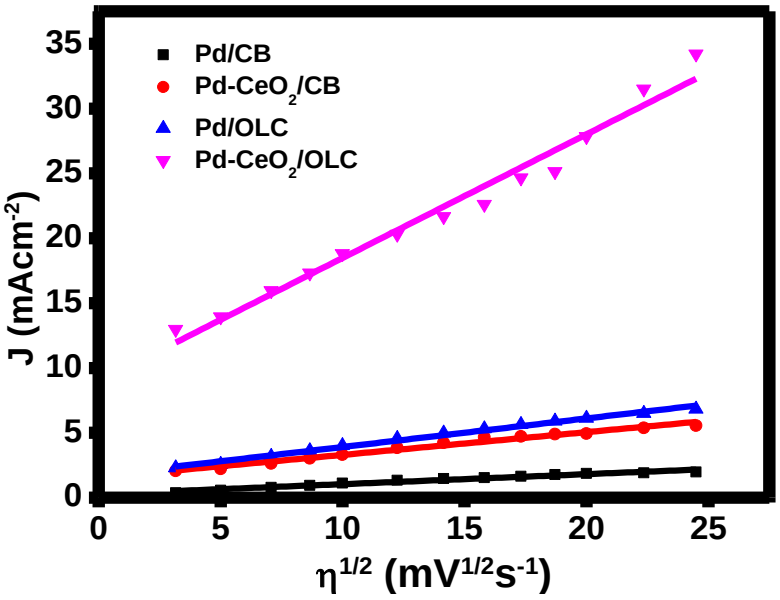


Figure 4.20: Plot of current density against the square root of the scan rates for the EOR of Pd/CB, Pd/OLC, Pd-CeO_2/CB and Pd-CeO_2/OLC.

4.2.2 Linear Sweep Voltammetry (LSV)

LSV (**Figure 4.21**) was used to investigate the kinetics of the electrocatalysis, as well as the EOR performance of the electrocatalysts at different concentrations of EtOH in the 0.5 M KOH electrolyte. The current densities increased for all the electrocatalysts as the concentration of ethanol increased.

However, an abrupt decrease in current density was noticed at 2.00 M ethanol for Pd-CeO_2/OLC and 2.5 M ethanol for Pd-CeO_2/CB, suggesting that the Pd-active sites of the Pd-CeO_2-OLC are easily saturated with carbonaceous species at higher ethanol concentrations, due to the inadequacy of OH^-_{ads}. This suggests that while the diffusion of OH^- ions controls the oxidation of the carbonaceous species, at lower ethanol concentrations the oxidation is controlled by the diffusion of ethanol as there are enough OH^- ions, giving rise to rapidly increasing current densities at lower concentrations [8, 9].

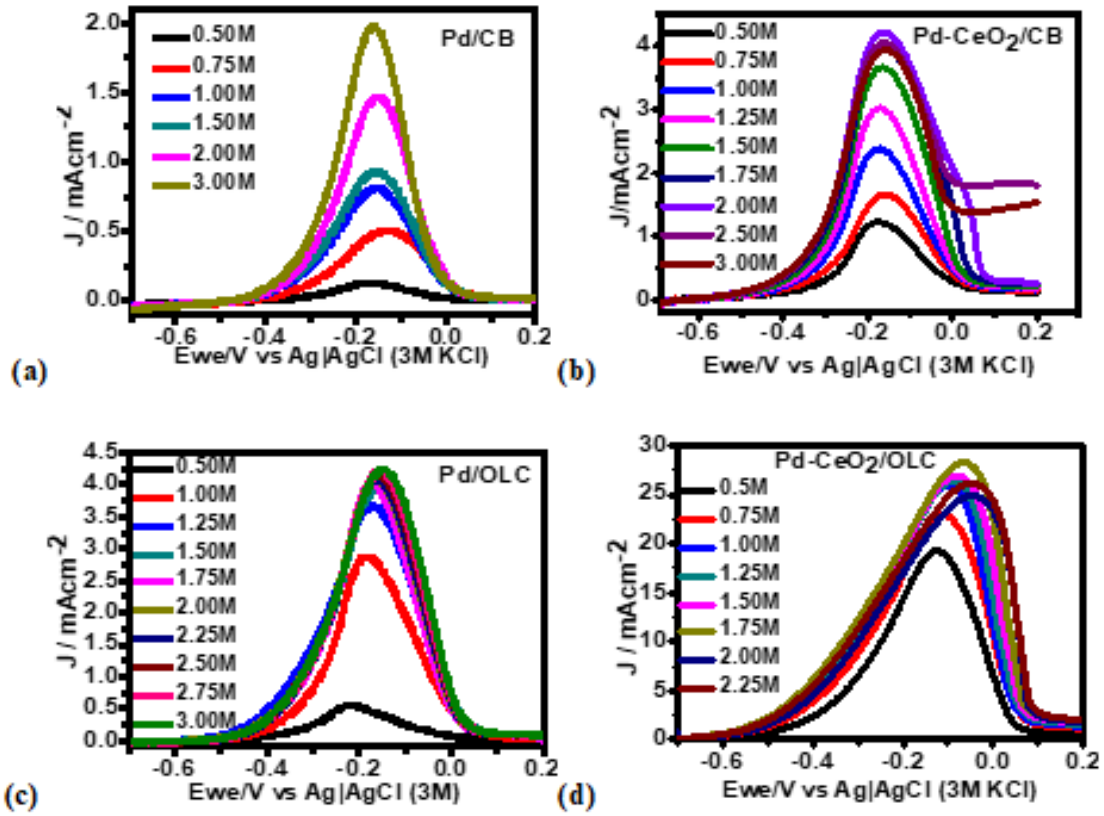


Figure 4.21: LSV concentration studies of (a) Pd/CB (b) Pd-CeO_2/CB (c) Pd/OLC (d) Pd-CeO_2/OLC.

The kinetics of Pd-CeO_2/OLC in ethanol was investigated using the Tafel equation for oxidation processes (**Equations 4.4 and 4.5**) and the Tafel (b) and the transfer coefficient (α) values were determined.

$$\eta = a + b\,logj \qquad \textbf{4.4}$$

$$b = \frac{2.303RT}{(1-\alpha)nF} \qquad \textbf{4.5}$$

With the parameters retaining their meanings as defined in **Chapter 2** (**Section 2.7.4**).

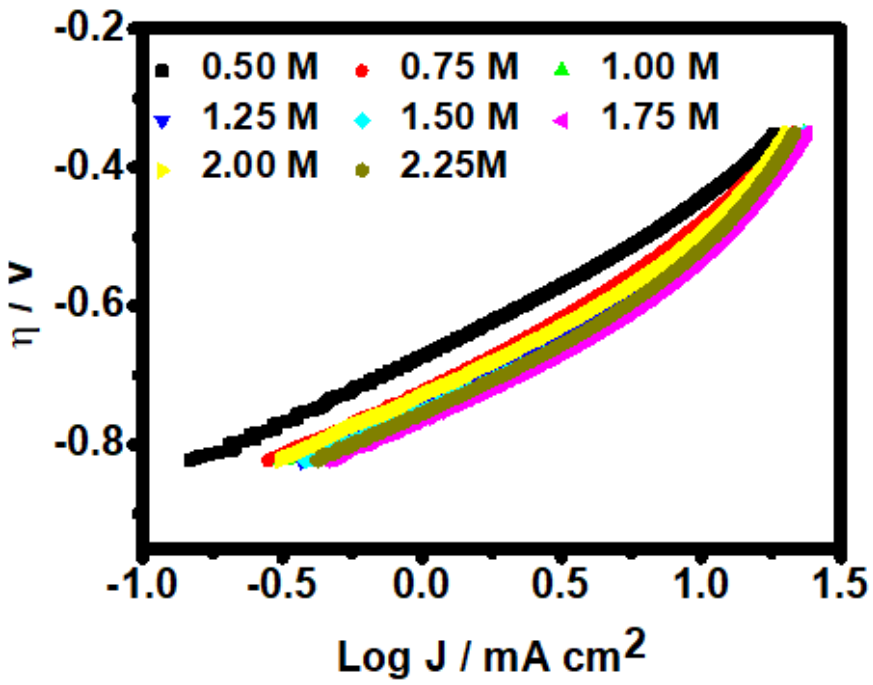


Figure 4.22: Tafel Plot of the EOR at the Pd-CeO_2/OLC electrode.

Every electrochemical process passes through a transition state, which is less stable than both reactants and products. Transfer coefficient (α) is used to define kinetics of electrochemical reaction. [10]. It tells how reactant-like or product-like the transition state is with respect to its electrical behavior and has values between 0 and 1. If it is close to either of the two values (0 or 1), we can say that the transition state is either very reactant-like or very product-like.

$$\alpha = -\frac{2.303RT}{bnF} \qquad \textbf{4.6}$$

From the Tafel plots (η vs. log J) (**Figure 4.22**), the Tafel slope is obtained as 251.30 ± 1.91 mV dec^{-1}. The value of αn ≈ 0.24 for the Pd-CeO_2/OLC electrode, where n = 3 for EOR [11,8]. Thus α ≈ 0.1, which indicates that the EOR is irreversible [12].

4.2.3 Chronoamperometry (CA)

Stability is an important aspect to be considered in the choice of electrocatalyst materials for fuel cell application. CA (**Figure 4.23**) was performed on all the electrocatalysts at a potential of -3.0 V for 1800 seconds.

The EOR current densities rapidly decrease at first. This is caused by the buildup of some carbonaceous species poisoning during ethanol oxidation [13]. The specific activity (**Figure 4.23a**) and the mass activity (**Figure 4.23b**) were plotted for each catalyst and the Pd-CeO_2/OLC-modified GCE showed the least reduction in current density.

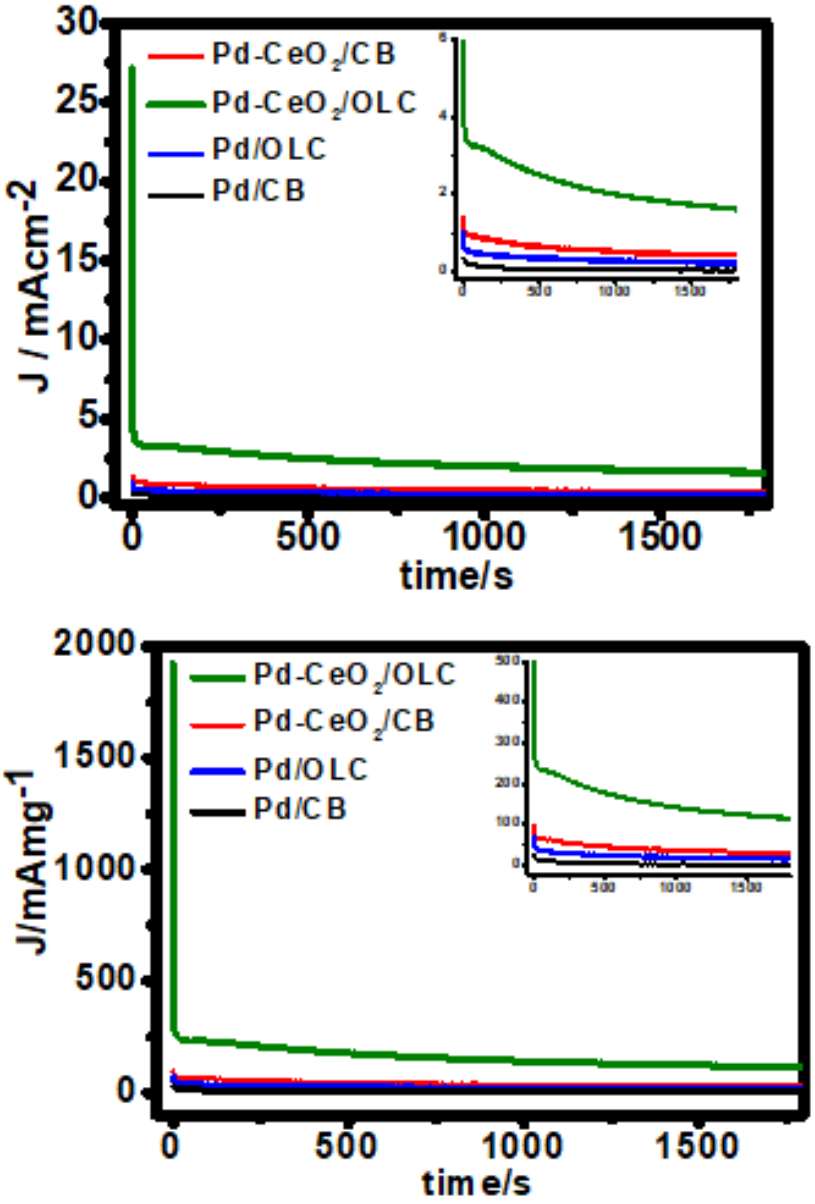


Figure 4.23: CA evolutions of the Pd electrocatalysts.

4.2.4 Electrochemical Impedance Spectroscopy (EIS)

The EIS (**Figure 4.24**) data of the four catalysts were best fitted with the Randles-Sevcik equivalent circuit and the values are summarized in **Table 4.7**. The charge transfer resistance (R_{ct}) obtained in the EIS increases as follows:

Pd-CeO_2/OLC (905.5 Ω) < Pd-CeO_2/CB (3680 Ω) < Pd/OLC (5687 Ω) < Pd/CB (28561 Ω) with errors less than 1.

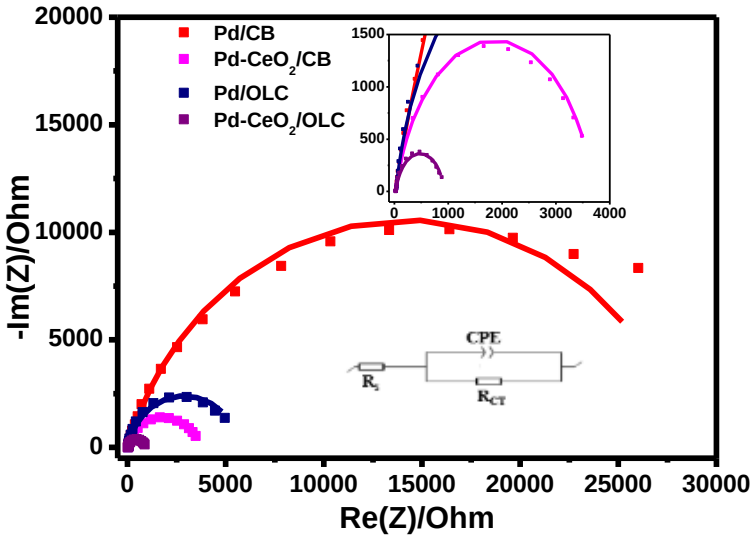


Figure 4.24: Nyquist plots of the electrocatalysts.

Table 4.8: EIS values obtained at the electrodes.

Catalyst	R_s (Ohm)	R_{ct} (Ohm)	a	CPE (F)
Pd/CB	22.36 ± 0.29	28561 ± 2.19	0.81 ± 0.5	13.33E-6 ± 0.58E-9
Pd-CeO_2/CB	27.62 ± 0.29	3680 ± 1.11	0.85 ± 0.5	64.33E-6 ± 58.38E-9
Pd/OLC	31.58 ± 0.27	5687 ± 3.45	0.89 ± 0.5	99.83E-6 ± 84.84E-9
Pd-CeO_2/OLC	24.87 ± 0.28	905.5 ± 1.59	0.86 ± 0.5	0.27E-3 ± 0.74E-6

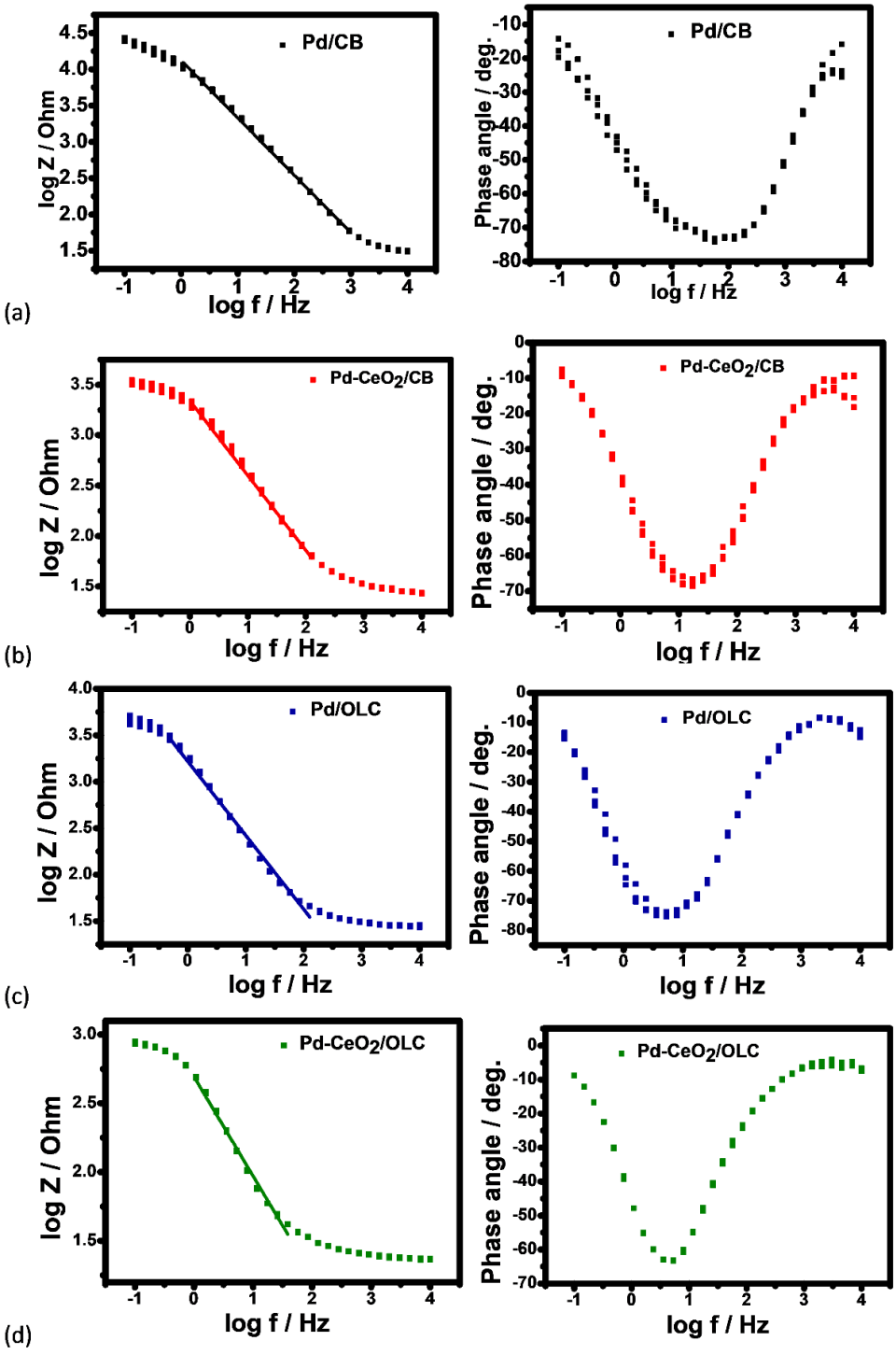


Figure 4.25: Bode plots: (log Z vs log f) and their corresponding (phase angle vs log f).

From the plots of phase angle (θ / °) against log f (Hz) (**Figure 4.25**), the phase angles of EtOH for Pd/CB, Pd-CeO_2/CB, Pd/OLC and Pd-CeO_2/OLC are ~ 75°, ~ 70°, ~ 75° and 65° respectively. These values are less than the 90° expected for an ideal capacitor. This confirms the pseudocapacitive nature of the materials and the presence of CPE.

The slopes of EtoH recorded for each catalyst are (ca. 0.79, 0.74, 0.79 and 0.72) indicative of pseudocapacitive and resistive behaviors at these frequency regions [14, 15].

EIS data throws more light on the reversibility of the redox processes, by calculating the exchange current density (j_0) and rate constant of electron transfer (k_{et}) using the conventional **Equations 4.7 and 4.8** [35]:

$$j_0 = \frac{RT}{nFR_{ct}} \qquad \textbf{4.7}$$

$$k_{et} = \frac{j_0}{nFA} \qquad \textbf{4.8}$$

where A is the geometric surface area of the electrode and R, T, n, and F retain their definitions as described previously. The higher the values of j_0 and k_{et} the better the electrocatalysis.

4.2.5 Direct Ethanol Micro-Fuel Cell (µ-DEFC) Measurement

The alkaline µ-DEFC was explored using a micro-3D printed cell (**Figure 4.26**), fabricated with two-electrode configuration. The cathode was made by preparing slurries of 10.0 mg of FeCo/C (3.0 wt % metal), while the anode was made by preparing slurries of 10.0 mg of the electrocatalysts. The anode and cathode materials were each mixed with 200 µL of EtOH and 20 µL of PTFE binder. The FeCo/C slurry was coated on doubled carbon papers (for the cathode) and the slurry of each electrocatalyst was coated on a piece of nickel foam (for the anode). The anode material and cathode material were then

sandwiched in-between laminated sheets and arranged into anode and cathode compartments, respectively.

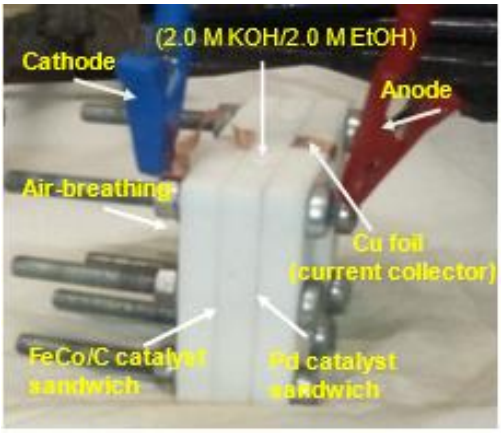


Figure 4.26: A two-electrode set-up consisting of the micro 3D-printed cell for ADEFC test.

All four electrocatalysts were tested for the µ-DEFC using the micro-3D printed cell (**Figure 4.26**) for proof-of-concept. From the power curves of the electrocatalysts **Figure 4.27a**, Pd/CB, Pd/OLC, Pd-CeO_2/CB and Pd-CeO_2/OLC have peak power density (P_m) values of 3.59, 19.72, 22.74 and 27.15 mW cm^{-2} respectively.

From the galvanostatic discharge test (**Figure 4.27b)** at 20 mA cm^{-2} for 48 h, the voltage drop for Pd/CB, Pd/OLC, Pd-CeO_2/CB and Pd-CeO_2/OLC are 0.774 to 0.098 V (12.7% energy retention), 0.904 to 0.156 V (17.3% energy retention), 0.952 to 0.612 V (64.2% energy retention) and 0.927 to 0.624 V (67.3% energy retention) respectively.

The materials containing CeO_2 have significantly better electrocatalytic performance and also retain more energy. EIS (**Figure 4.28a)** was performed at open circuit potentials (*OCV*) of 0.70, 1.0, 1.01 and 1.08 V on the Pd/CB, Pd/OLC, Pd-CeO_2/CB and Pd-CeO_2/OLC electrocatalysts, respectively. and

the spectra were modeled with the Voigt *EEC* (**Figure 4.28b**) and the EIS parameters are summarized in **Table 4.8**.

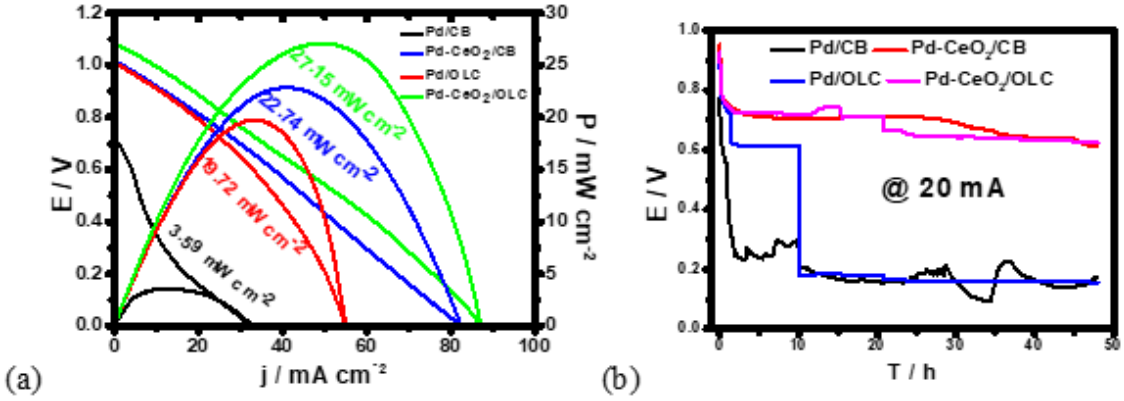
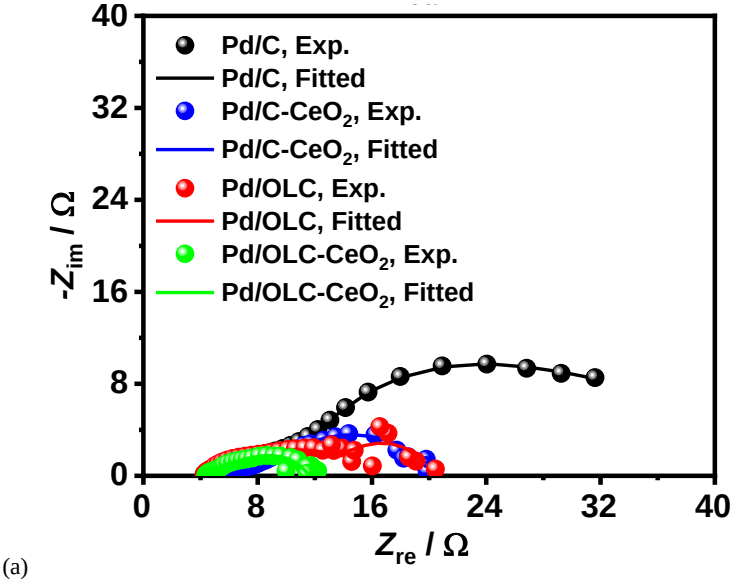


Figure 4.21: (a) potential and power curves, (b) galvanostatic discharge test at 20 mA cm^{-2}.



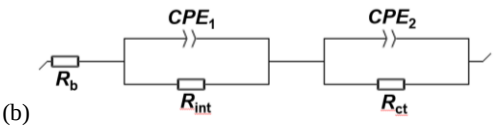


Figure 4.28: (a) Nyquist plot of the Pd/CB, Pd/OLC, Pd-CeO_2/CB and Pd-CeO_2/OLC using a 3D-printed cell; and (b) the Voigt EEC model.

Table 4.9: EIS parameters of the Pd-based electrocatalysts for the µ-DEFC

EIS parameters	**Pd/CB**	**Pd/OLC**	**Pd -CeO_2/CB**	**Pd-CeO_2/OLC**
R_b / Ω	4.39 ± 1.39	3.94 ± 1.00	5.38 ± 1.06	4.34 ± 0.19
R_{int} / Ω	10.72 ± 4.07	4.15 ± 0.87	4.62 ± 0.46	3.16 ± 0.79
CPE_1 / $mF.s^{\wedge(a-1)}$	17.95 ± 8.94	104.00 ± 1.00	10.25 ± 2.72	11.11 ± 0.10
a_1	0.75	0.5	1.00	0.80
R_{ct} / Ω	23.41 ± 2.25	12.07 ± 0.62	11.59 ±1.54	4.14 ± 0.85
CPE_2 / $mF.s^{\wedge(a-1)}$	26.78 ± 4.80	6.43 ± 4.22	20.16 ± 0.00	8.95 ± 0.12
a_2	0.83	0.5	0.70	0.50

From the power-law equation explained in **Equation 2.18**, the *CPE* impedance (Z_{CPE}) is related to the ideality factor, *a,* with values ranging from -1 to +1. If *a* = 0, the Z_{CPE} is a pure resistor. If *a* = -1, it means that it is a pure inductor. If *a* = 1, it is a pure capacitor, while *a* = 0.5 means that the CPE is equal to the Warburg impedance (Z_w) due to diffusion of the electrolyte ion [23,24]. The values obtained ($0.5 < a < 1.0$) confirm the inhomogeneous charge storage elements used in the Voigt *EEC*. Series resistance ($R_b + R_{int} + R_{ct}$) values of *ca.* 38.5, 20.16, 21.59 and 11.64 Ω are recorded for the Pd/CB, Pd/OLC, Pd-CeO_2/CB and Pd-CeO_2/OLC.

4.2.6 DFT Simulation for EOR

The electronic states of Pd in the nanocomposites were investigated by examining the band structures, and from **Figure 4.29 (a-d)**, the Pd surfaces are observed to be metallic with the energy bands crossing the Fermi level.

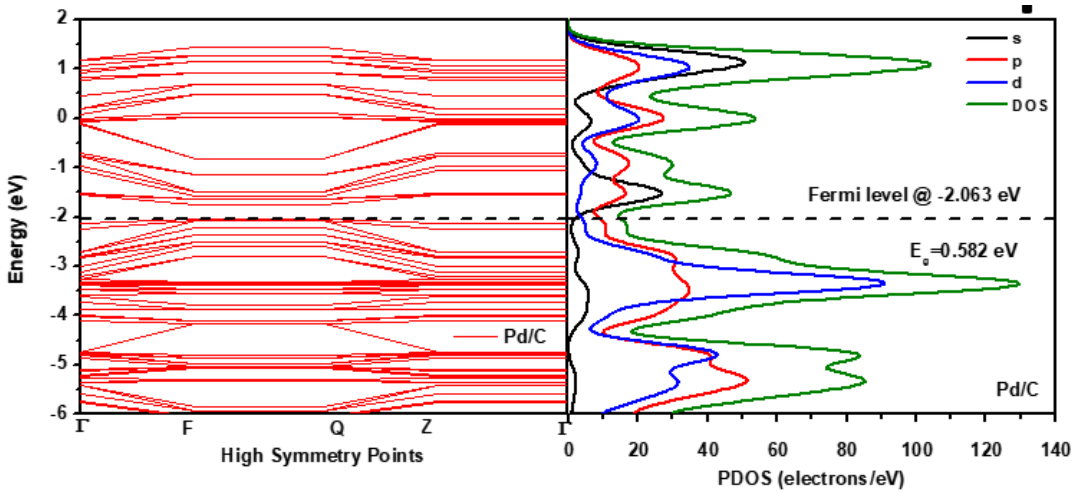


Figure 4.29a: Electronic energy band structures of the Pd surfaces of Pd/CB

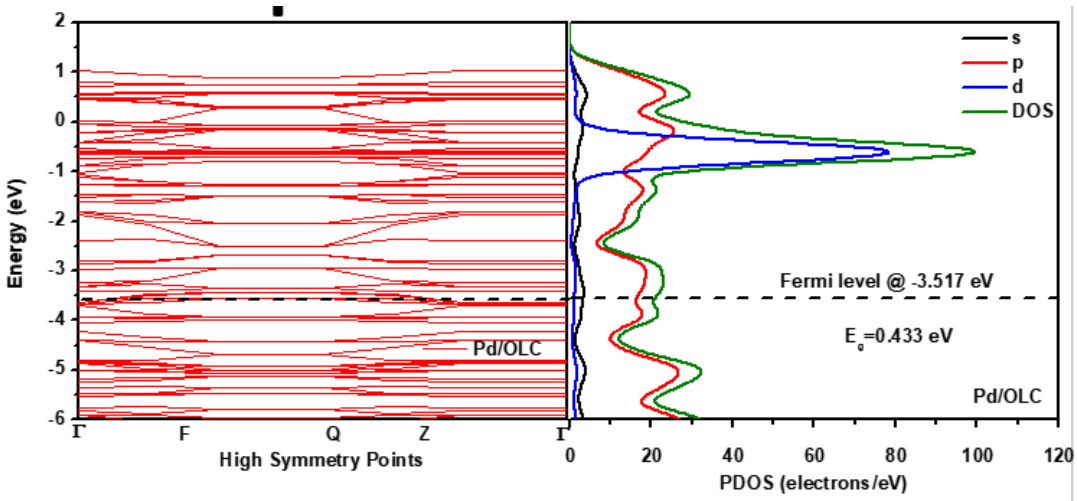


Figure 4.29b: Electronic energy band structures of the Pd surfaces of Pd/OLC

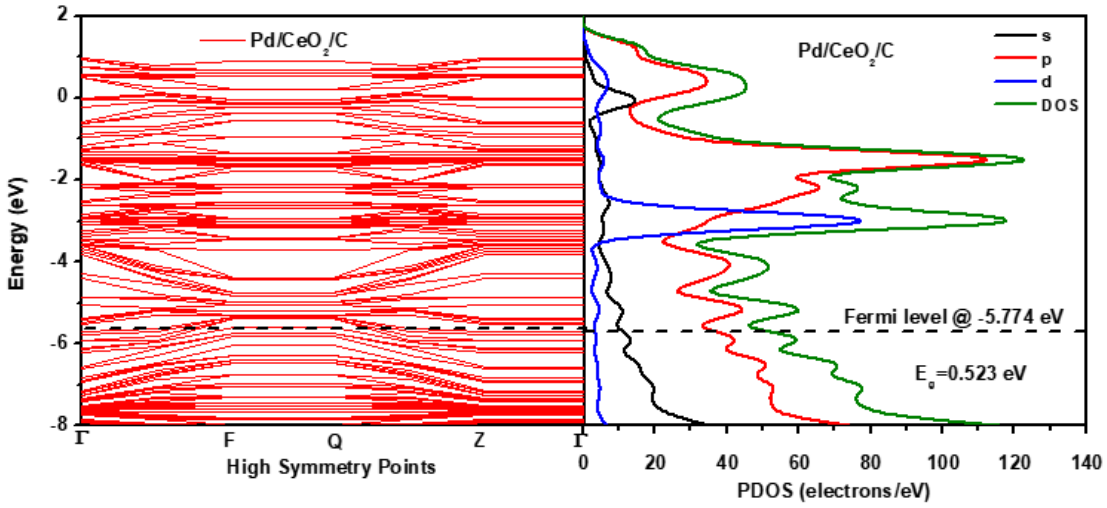


Figure 4.29c: Electronic energy band structures of the Pd surfaces of Pd-CeO_2/CB.

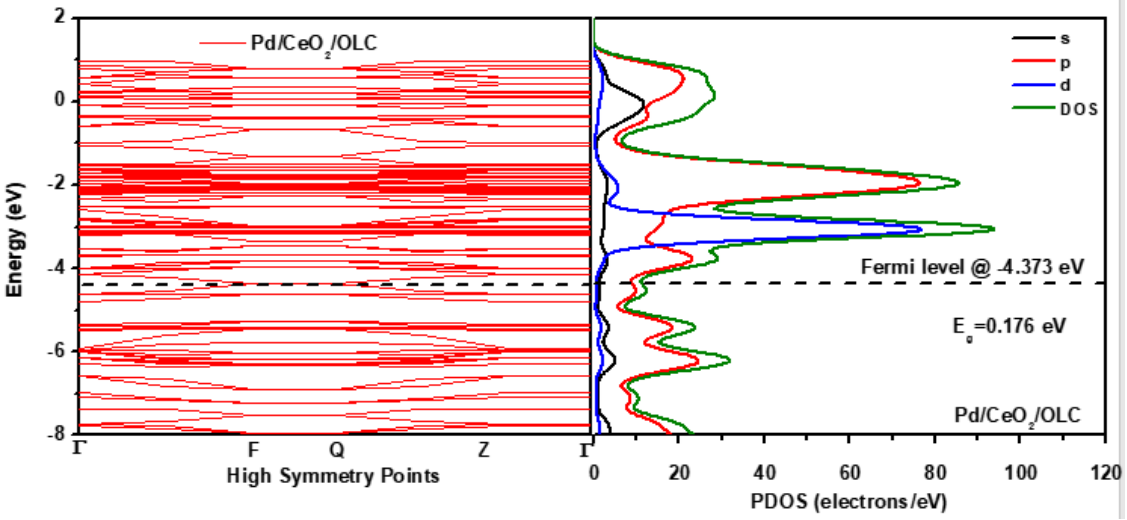
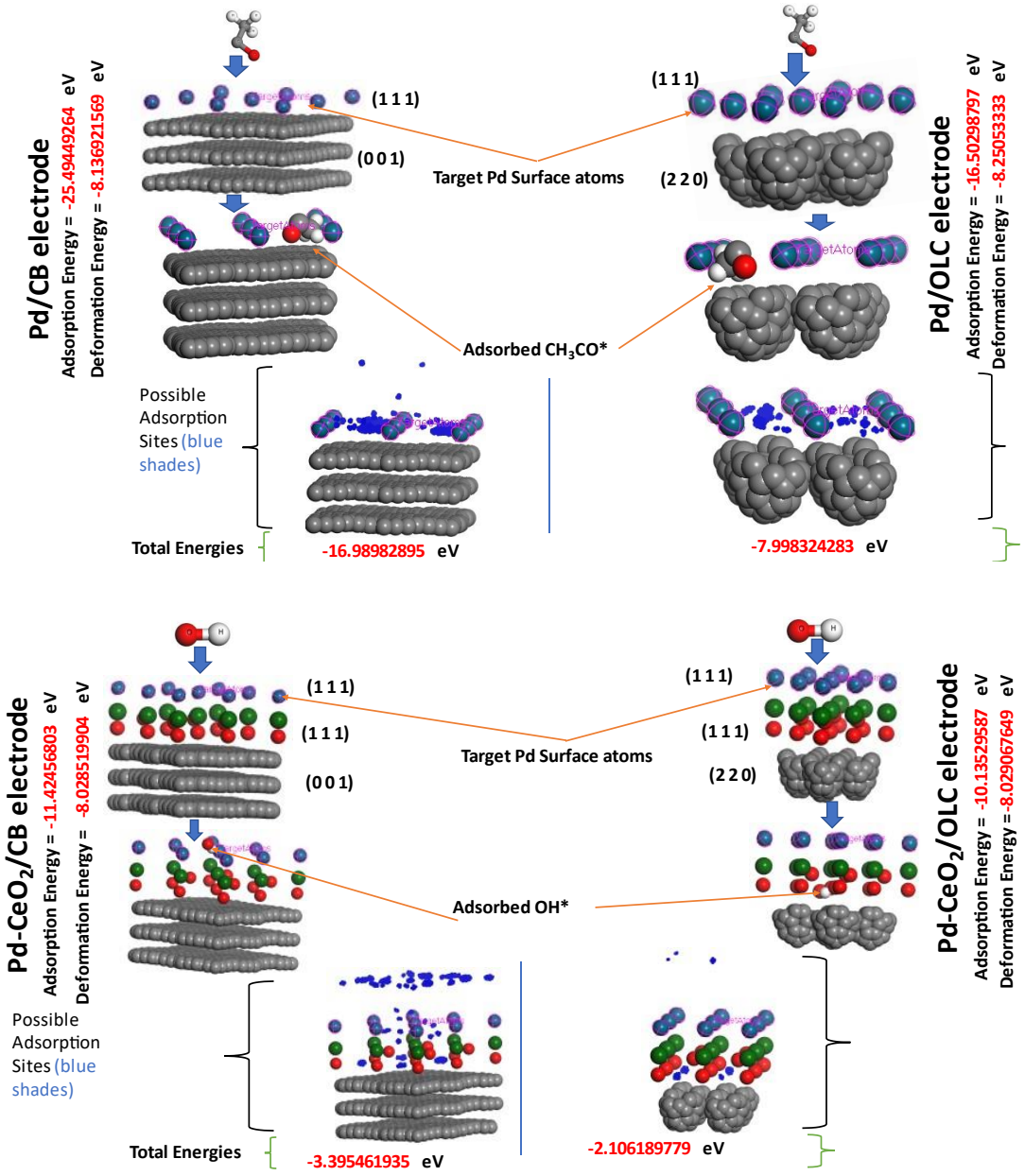


Figure 4.29d: Electronic energy band structures of the Pd surfaces of Pd-CeO_2/OLC.



s

Figure 4.30: The interactions between the ethanol molecule and the different palladium catalysts.

The DFT results (**Figure 4.30** and **Table 4.9**) reveal that the materials containing CeO_2 have weaker adsorption energy (in absolute values) of OH than their counterparts without CeO_2. The CH_3CO adsorption energy of the Pd-CeO_2/CB electrode is -28.933 eV (when compared with Pd/CB calculated to be

-25.494 eV) which means adsorption is improved by 13.5 % and that of Pd-CeO_2/OLC is -16.811 eV (when compared with Pd/OLC calculated to be -16.503 eV); translating to 18.7 % improvement.

Thermodynamically, the more favored catalyst for EOR (based on the values of Gibbs or A.E (eV)) is Pd/CB > Pd-CeO_2/CB > Pd-CeO_2/OLC > Pd/OLC [26]. This prediction is opposite to electrocatalytic data where OLC is better than carbon black, meaning that conductivity is contributing to the electrochemical performance.

Table 4.10: Energies calculated for the Ethanol-Pd configurations.

Electrode	Adsorbate	Gibbs F.E (eV)	A.E (eV)	D.E (eV)	E_f (eV)	E_g (eV)	K.E (Ha)
Pd/CB					-2.063	0.582	-277.311
	OH*	-5.087	-13.116	-8.029			
	CH_3CO*	-16.990	-25.494	-8.137			
Pd/OLC					-3.517	0.433	-109.200
	OH*	-2.418	-10.448	-8.029			
	CH_3CO*	-7.998	-16.503	-8.251			
Pd-CeO_2/CB					-5.774	0.523	-897.591
	OH*	-3.395	-11.424	-8.029			
	CH_3CO*	-20.429	-28.933	-8.040			
Pd-CeO_2/OLC					-4.373	0.176	-170.586
	OH*	-2.106	-10.135	-8.029			
	CH_3CO*	-8.306	-16.811	-8.241			

4.3 Hydrogen Oxidation Reaction

In this section, the electrocatalytic performances of Pd/CB, Pd/OLC, Pd-CeO_2/CB and Pd-CeO_2/OLC electrocatalysts toward alkaline HOR and ORR are discussed. It is known that such non-precious metal electrocatalysts like FeCo/C, NCFe-950 work excellently for driving the ORR in AMFCs [33,34], but the electrocatalysts used in this research were studied out of curiosity.

The AMFCs are considered in this study, therefore the HOR was studied in alkaline environment. The comprehensive alkaline HOR mechanism is given in **Equation 4.9 – 4.11** [35]. The HOR depends on two important descriptors: **Equation 4.9** or **4.10** gives the H binding energy or H adsorption and the promotional effect of oxygen-containing species (oxophilic or spill-over properties) of the metal oxide catalysts (the ability to adsorb OH_{ads} and donate it to the M-H_{ads} to quickly remove the H_{ads} from the active site of the Pd electrocatalysts) are shown in **Equation 4.11**, which is often assumed to be the RDS of the HOR [36,37].

$$H_2 + 2M \rightarrow MH_{ads} + MH_{ads} \text{ (Tafel, } b_a = 29.6 \text{ mV dec}^{-1}\text{)} \quad \textbf{4.9}$$

$$H_2 + OH^- + M \rightarrow MH_{ads} + H_2O + e^- \text{ (Heyrovsky, } b_a = 39.4 \text{ mV dec}^{-1}\text{)} \quad \textbf{4.10}$$

$$MH_{ads} + OH^- \rightarrow H_2O + M + e^- \text{ (Volmer, } b_a = 118.2 \text{ mV dec}^{-1}\text{)} \quad \textbf{4.11}$$

Where M is an active site of the electrocatalysts to chemisorb hydrogen intermediate (H_{ads}).

The HOR measurements were carried out on a Metrohm Autolab workstation (**Figure 4.39**) at room temperature. The workstation comprised of a three-electrode system, including a glassy carbon-disk RDE electrode (diameter 5 mm) as the WE, an Ag|AgCl ($E_{(RHE)} = E_{(Ag|AgCl)} + (0.197 + 0.0591\ pH)$ V)

electrode as the RE, and a platinum wire, which was used as the CE in 0.1 M KOH.

To make the catalyst ink, the powder (1 mg) is dispersed in EtOH (1 mL) (Sigma Aldrich, 99% absolute ethanol) and 20μL of Nafion (5 wt%, Sigma Aldrich). The mixture was then sonicated for 30 minutes to obtain a homogeneous mixture and left overnight.

The glassy carbon disk was cleaned prior to electrode modification. The already prepared catalyst ink was sonicated again for 30 minutes and the ink (30 μL) was deposited dropwise on the GCE and allowed to dry.

Cyclic voltammograms (**Figure 4.31**) were collected in N_2-saturated alkaline solution of 0.1 M KOH prior to the HOR experiments. This was used to determine the ECSA of the electrocatalysts.

The ECSA was determined for all the electrocatalysts by integrating the PdO reduction peak found between 0.5 V and 0.8 V (vs. RHE) to get their charges and following the conventional method by Rand and Wood [38]. The ECSA of the Pd/CB, Pd/OLC, Pd-CeO_2/CB and Pd-CeO_2/OLC electrocatalysts are estimated to be 6.154, 35.309, 59.280 and 91.188 $cm^2\ mg^{-1}$, respectively.

The greater ECSA values of Pd-CeO_2/CB and Pd-CeO_2/OLC are due to the addition of CeO_2, which transfers additional O species to the electrocatalysts, thus enhancing their PdO reduction peak and shifting their potentials to lower values so that they require lower energy for electron transfer than the Pd/CB and Pd/OLC [39].

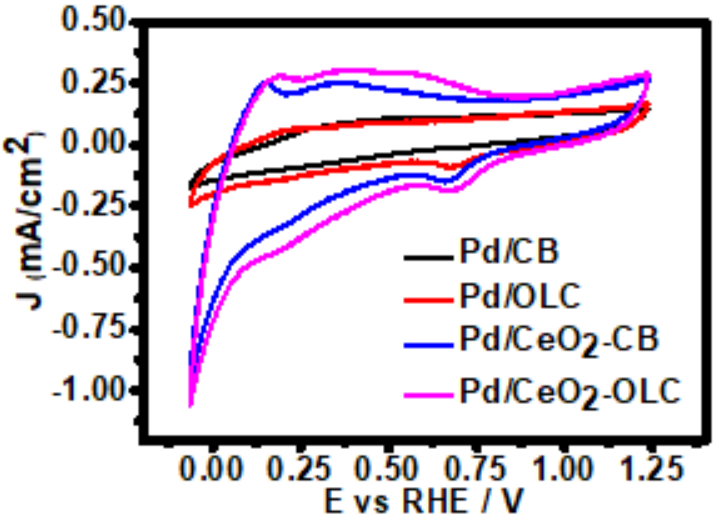


Figure 4.31: Cyclic voltammograms at the (b) Pd/CB (c) Pd/OLC (d) Pd-CeO_2/CB (e) Pd-CeO_2/OLC electrodes.

4.3.1 HOR Polarization Curves

The behaviour of the catalysts toward HOR was investigated using alkaline electrolyte solution of 0.1 M KOH saturated with H_2 at room temperature. LSV (**Figure 4.32 a – e**) was performed at rotation speeds from 400 to 2400 rpm.

As the speed of the RDE increases, the *j* value also increases for all the electrocatalysts (**Figure 4.32 a – d**). This is modeled to the Koutecky-Levich equation [41] using the RDE diffusion-limited current density (j_{lim} = 2.81 mA cm^{-2}_{disk}).

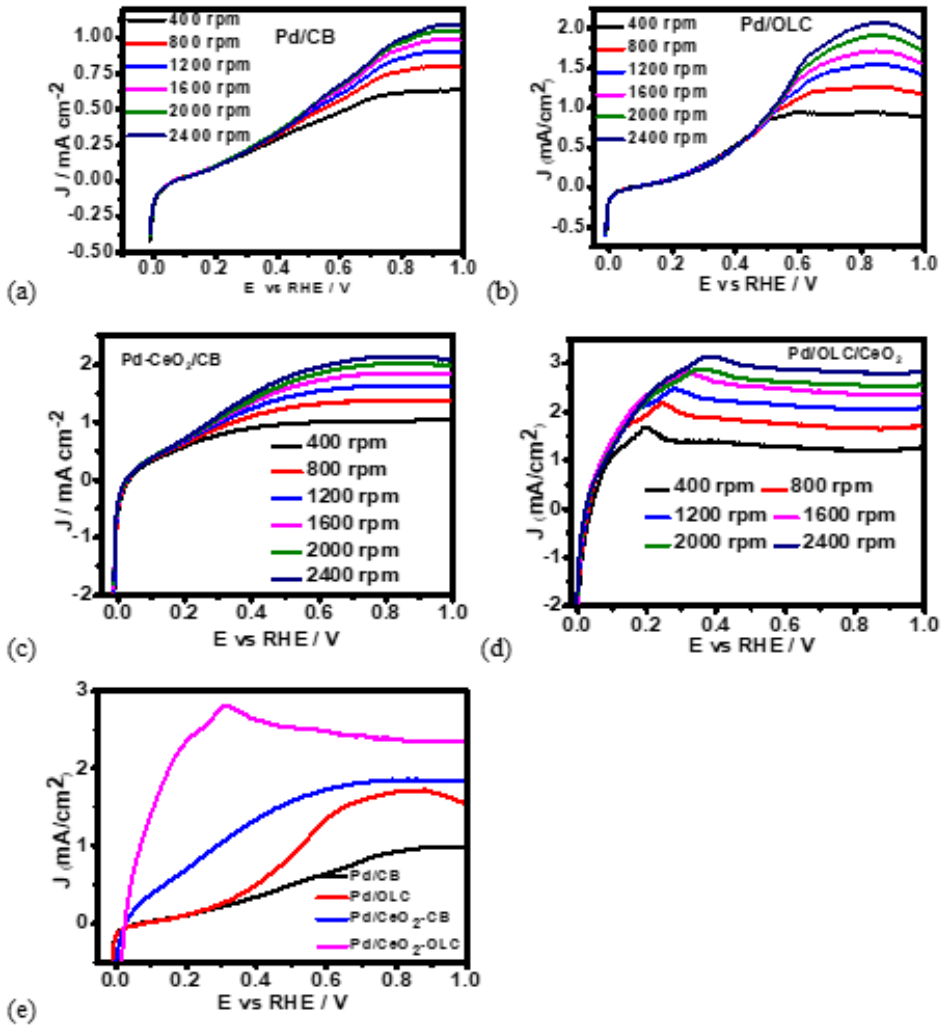


Figure 4.32: HOR Polarization curves at (a) Pd/CB (b) Pd/OLC (c) Pd-CeO_2/CB (d) Pd-CeO_2/OLC (e) 1600 rpm.

The K-L equations are given in **Equations 4.12 and 4.13**, where the overall current density (j_{lim}) is resolved into the kinetic ($1/j_K$) process and the diffusion ($1/j_D$) process.

$$\frac{1}{j_{\text{lim}}} = \frac{1}{j_{\text{K}}} + \frac{1}{j_{\text{D}}} = \frac{1}{j_{\text{K}}} + \frac{1}{B_{\text{L}}\omega^{1/2}} \qquad \textbf{4.12}$$

All parameters retain their meanings as defined in **Chapter 2** (**Section 2.7.6.**1).

$$B_{\mathrm{L}} = \frac{1}{slope} = 0.62nFCoD^{2/3}\upsilon^{-1/6} \qquad \textbf{4.13}$$

where n=2 for the HOR, *c*o = 1.2 x10^{-6} mol cm^{-3} (for H_2 gas in 0.1 M KOH) and υ = 0.01 cm^2 s^{-1}.

The K-L plot (**Figure 4.33**) of the electrocatalysts was obtained at the overpotentials (*vs.* RHE) of 0.65, 0.7, 0.75, 0.8 and 0.85 V.

The j_K values of (1.075, 1.290, 1.564, 1.799 and 1.975 mA cm^{-2}_{disk}), (3.882, 6.268, 8.687, 10.797 and 12.369 mA cm^{-2}_{disk}), (6.841, 7.734, 8.752, 9.296, and 9.038 mA cm^{-2}_{disk}) and (25.063, 28.450, 31.888, 35.436 and 36.324 mA cm^{-2}_{disk}) are derived for the Pd/CB, Pd/OLC, Pd-CeO_2/CB and Pd-CeO_2/OLC respectively from their intercepts ($1/j_K$) at the different η (overpotential) values.

From the j_K values, the HOR heterogeneous rate constant (k_0) at the different overpotentials are determined and the mean values are obtained as (6.653 x 10^{-3}), (3.6278 x 10^{-2}), (3.5982 x 10^{-2}) and (1.35739 x 10^{-1}) cm/s for Pd/CB, Pd/OLC, Pd-CeO_2/CB and Pd-CeO_2/OLC, respectively. The diffusivity (*D*) of H_2 was determined from the slopes, giving mean values of (0.623 x 10^{-2}), (0.659 x 10^{-2}), (0.696 x 10^{-2}) and (0.740 x 10^{-2}) cm^2/s for Pd/CB, Pd/OLC, Pd-CeO_2/CB and Pd-CeO_2/OLC, respectively.

These results show that there is a quicker rate of chemisorption and desorption of H_2 from the active sites of Pd for the Pd-CeO_2/CB and Pd-CeO_2/OLC electrocatalysts than for the Pd/CB and Pd/OLC electrocatalysts.

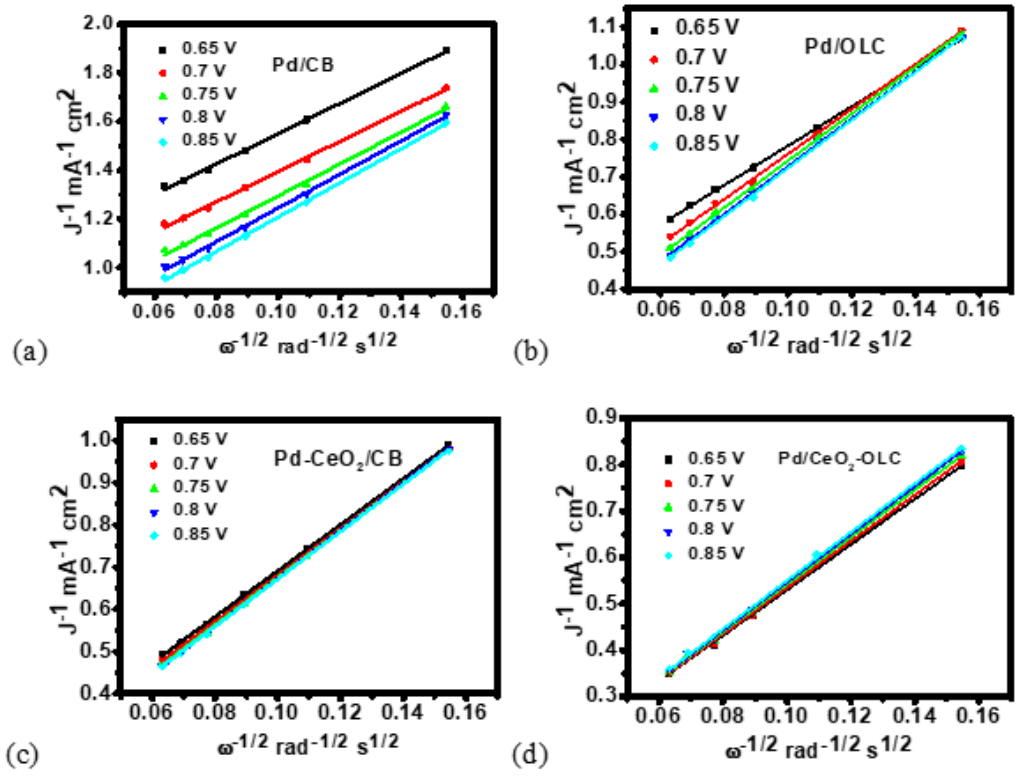


Figure 4.33: (a-d) Koutecky-Levich plot at different overpotential (η = 0.65, 0.7, 0.75, 0.8 and 0.85 V).

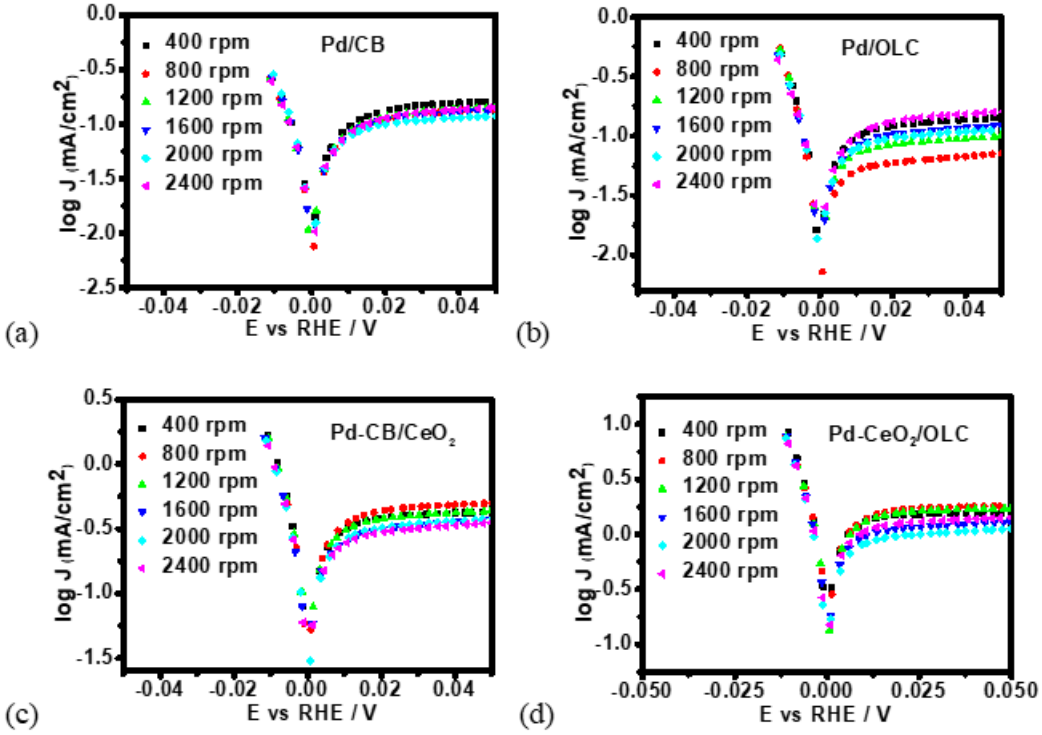


Figure 4.34: (a-d) Butler-Volmer plots of electrocatalysts.

To understand the mass transfer kinetics of the HOR in alkaline media, the Butler-Volmer plots (**Figure 4.34 a-d**) is used to determine the exchange current density ($j_{o,s}$) (**Table 4.10**), which is the rate of electron transfer under reversible conditions [40].

From the mass activity ($j_{o,m}$) values (**Table 4.10**) at 1600 rpm, the value for Pd-CeO_2/OLC is found to be 426.86 $mAmg^{-1}_{Pd}$, which is 23.8 times, 123.3 times and 597.8 times that of Pd-CeO_2/CB (17.90 mA mg^{-1}_{Pd}), Pd/OLC (3.46 mA mg^{-1}_{Pd}) and Pd/CB (0.71 $mAmg^{-1}_{Pd}$) respectively.

Tafel slopes (from **Figure 4.35**) were obtained at 1600 rpm for all the electrocatalysts. The slope values (**Table 4.11**) suggest that depending on the region, the RDS of the HOR is Tafel-Volmer or Heyrovsky-Volmer.

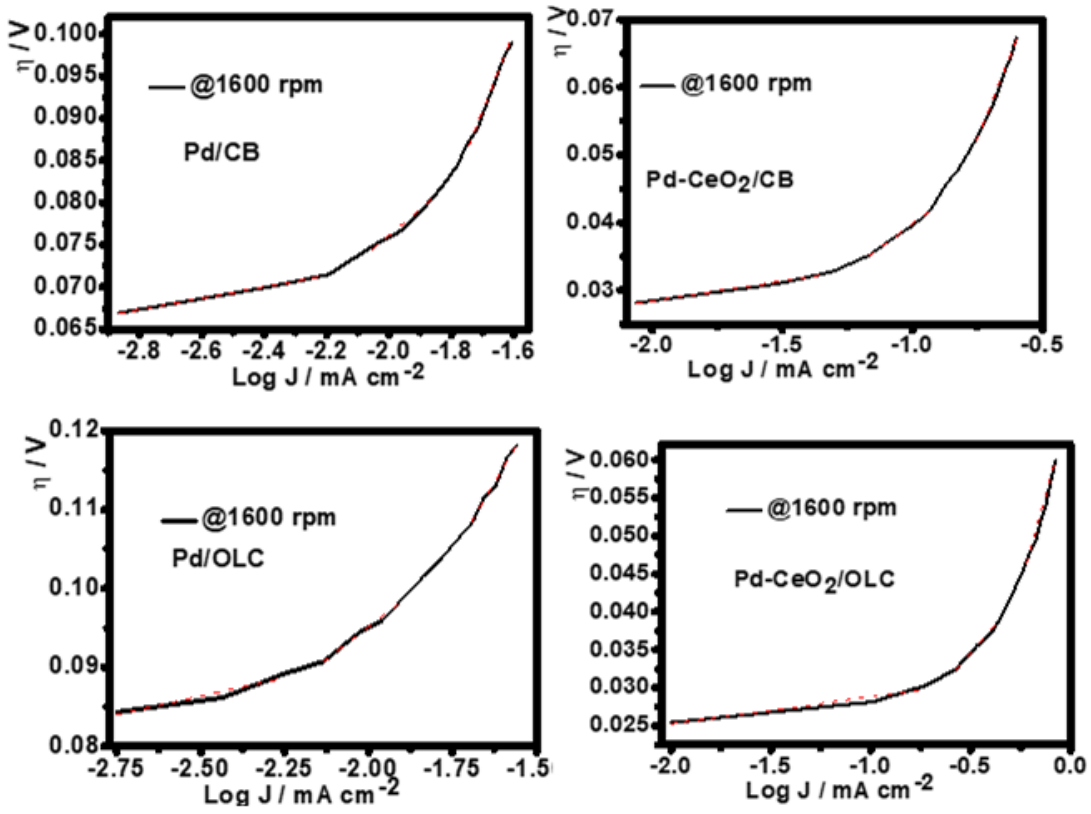


Figure 4.35: The HOR Tafel plots of the electrocatalysts.

Table 4.11: $j_{o,s}$ and $j_{o,m}$ values of Pd/CB, Pd-CeO_2/CB, Pd/OLC and Pd-CeO_2/OLC.

Kinetic parameters	Electrocatalysts			
	Pd/CB	Pd/OLC	Pd-CeO_2/CB	Pd-CeO_2/OLC
400 rpm				
$j_{o,s}$ / mA cm^{-2}	0.15	0.12	0.37	1.55
$j_{o,m}$ / mA mg^{-1}	0.92	4.20	22.05	141.25
800 rpm				
$j_{o,s}$ / mA cm^{-2}	0.12	0.05	0.44	1.74
$j_{o,m}$ / mA mg^{-1}	0.74	1.87	25.91	245.50
1200 rpm				
$j_{o,s}$ / mA cm^{-2}	0.13	0.08	0.36	1.62
$j_{o,m}$ / mA mg^{-1}	0.78	2.79	21.52	398.19
1600 rpm				
$j_{o,s}$ / mA cm^{-2}	0.12	0.10	0.30	1.07
$j_{o,m}$ / mA mg^{-1}	0.71	3.46	17.90	426.86
2000 rpm				
$j_{o,s}$ / mA cm^{-2}	0.10	0.09	0.31	0.91
$j_{o,m}$ / mA mg^{-1}	0.63	3.21	18.32	389.30
2400 rpm				
$j_{o,s}$ / mA cm^{-2}	0.12	0.13	0.27	1.202
$j_{o,m}$ / mA mg^{-1}	0.76	4.63	15.77	467.94

Table 4.12: Tafel slope values of the electrocatalysts at different regions.

Catalyst	@higher overpotential	@lower overpotential
Pd/CB	94.25 ± 4	31.47 ± 3.7
Pd-CeO_2/CB	91.3 ± 4	28.45 ± 1
Pd/OLC	74.26 ± 5	33.05 ± 2
Pd-CeO_2/OLC	105.38 ± 4	30.38 ± 2

4.3.2 Stability tests (HOR)

To investigate the stability of the electrocatalysts toward alkaline HOR, CA (**Figure 4.36**) was performed at 0.6 V *vs.* RHE for 2000 seconds and the enhanced stability in the Pd-CeO_2/OLC and Pd-CeO_2/CB was confirmed (due to CeO_2) compared to the Pd/OLC and Pd/CB.

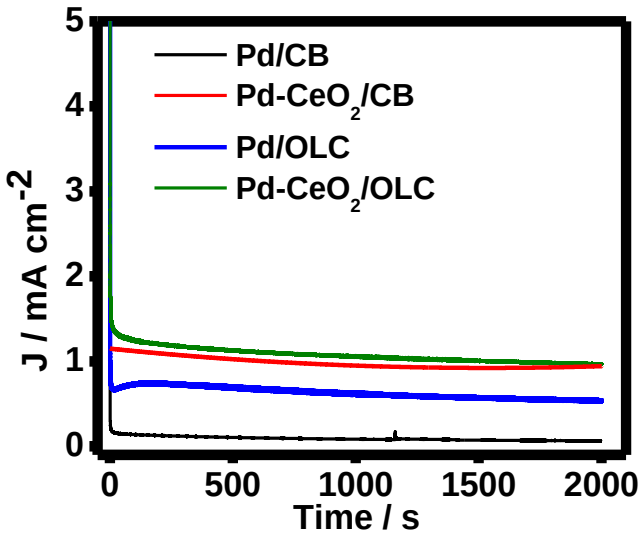


Figure 4.36: Chronoamperometry of the electrocatalysts @ 0.6 V vs. RHE and 1600 rpm.

The stability of each electrocatalyst was further confirmed by running cyclic voltammograms to 1000 cycles on each electrocatalyst, after which linear

sweep voltammograms are recorded at 1600 rpm. It is observed that the activity of the Pd/CB, Pd/OLC, Pd-CeO_2/CB and Pd-CeO_2/OLC reduced by 89%, 87%, 59% and 27% respectively (**Figure 4.37**).

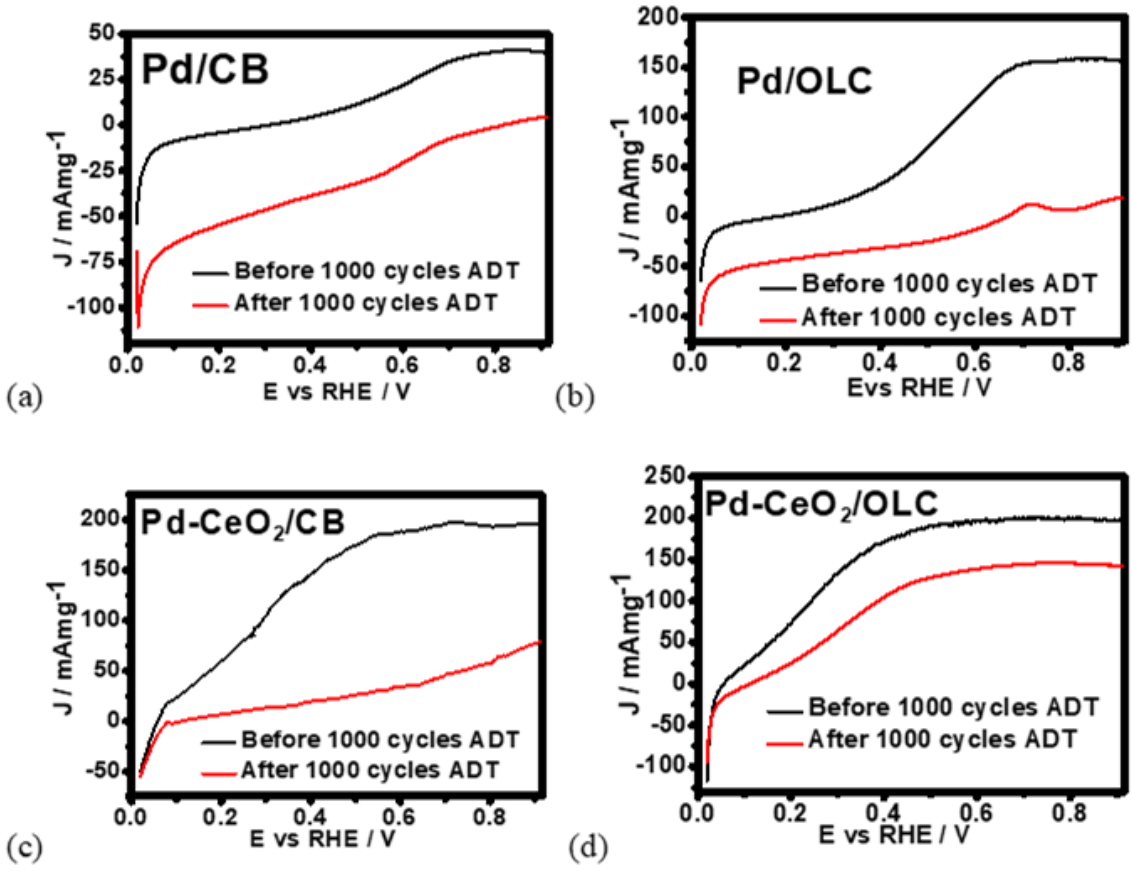


Figure 4.37: LSV after the 1st and 1000th cycles of CV (50 mVs^{-1}) at 1600 rpm (a) Pd/CB (b) Pd/OLC (c) Pd-CeO_2/CB (d) Pd-CeO_2/OLC.

4.3.3 DFT Simulation Results

From the DFT results, the presence of CeO_2 is seen to allow weak absorption of the hydrogen atom on the Pd, which is as a result of the lower adsorption energy of Pd-CeO_2/CB (-1.042 eV) (when compared with Pd/CB calculated to be -1.787) which means adsorption is improved by 41 % and that of Pd-CeO_2/OLC calculated to be -0.272 (when compared with Pd/OLC calculated to

be -0.838); translating to 67 % improvement. A weaker binding (adsorption) energy enhances the oxidation of the hydrogen as shown in **Figure 4.38**.

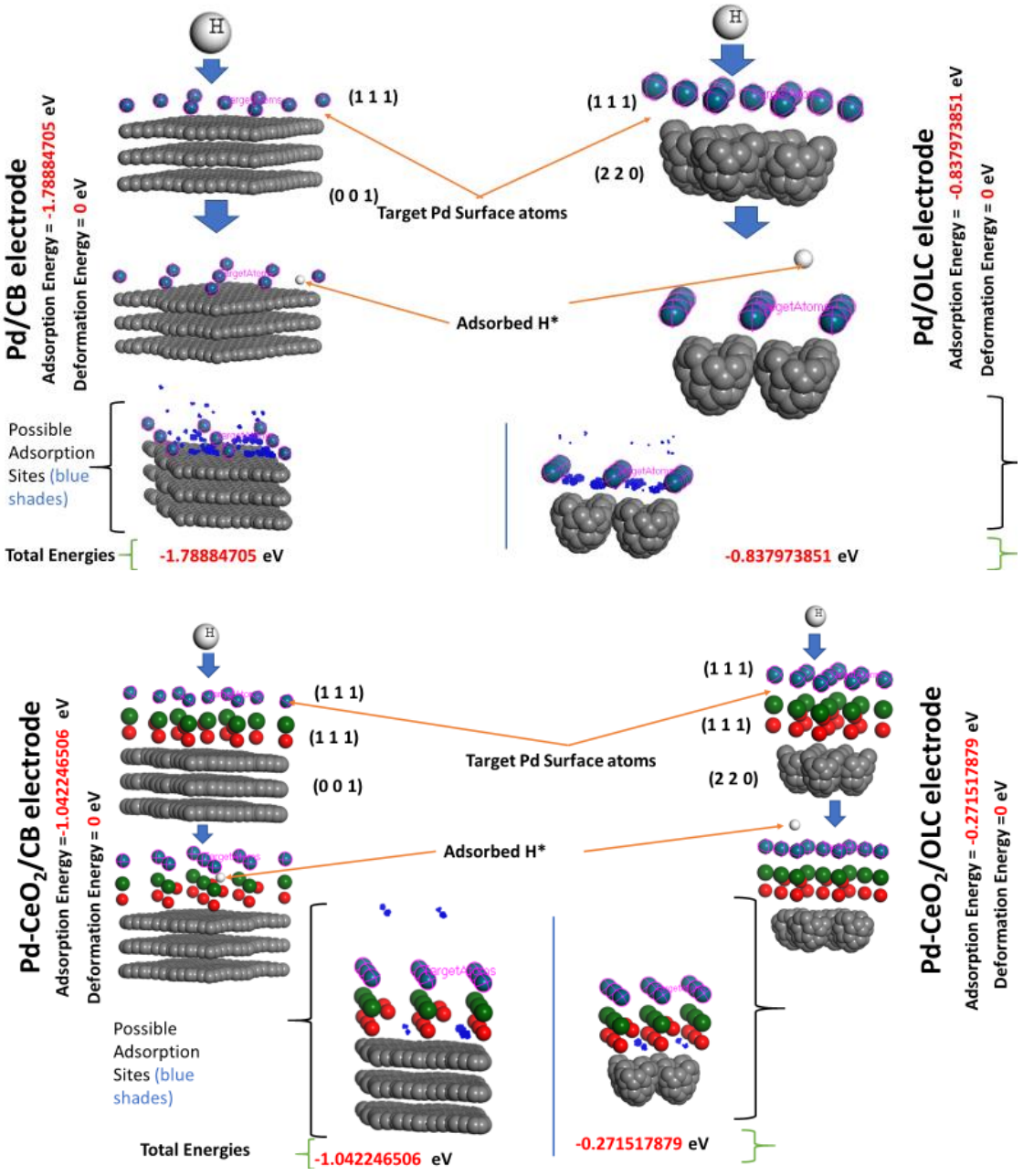


Figure 4.38: The interactions between the hydrogen molecule and the different palladium catalysts.

Table 4.13: The different energies calculated for the HOR at the electrodes.

Electrode	Adsorbate	Gibbs F.E (eV)	A.E (eV)	D.E (eV)	E_f (eV)	E_g (eV)	K.E (Ha)
Pd/CB	H*	-1.787	-1.787	0	-2.063	0.582	-277.311
Pd/OLC	H*	-0.838	-0.838	0	-3.517	0.433	-109.200
Pd-CeO_2/CB	H*	-1.042	-1.042	0	-5.774	0.523	-897.591
Pd-CeO_2/OLC	H*	-0.272	-0.272	0	-4.373	0.176	-170.586

4.4 Oxygen Reduction Reaction (ORR)

The ORR experiments were performed on a Metrohm Autolab workstation using the same conditions as in the HOR.

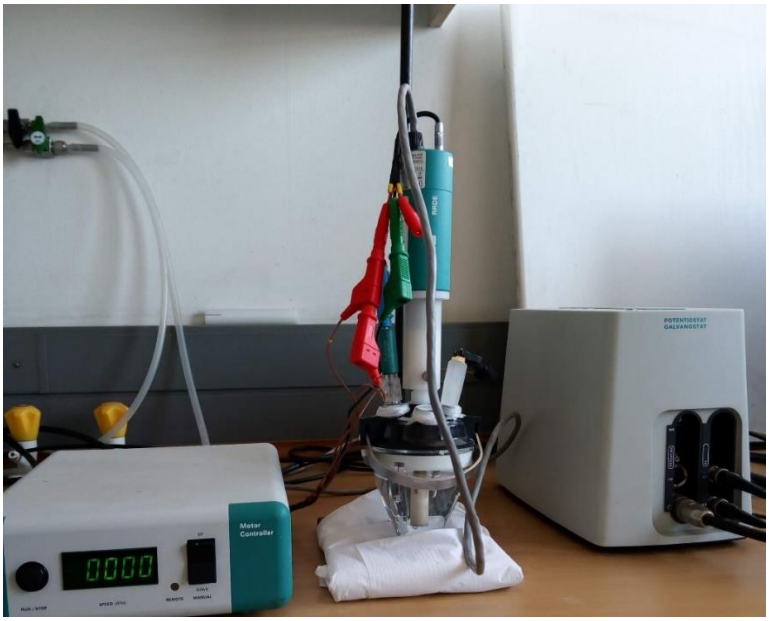


Figure 4.39: The Metrohm Autolab workstation.

The electrolytes were first saturated with O_2 by bubbling oxygen gas in the solution for about 30 minutes. CV was recorded at a scan rate of 50mV/s for each electrocatalyst and LSV was recorded in the potential range from ~ 0.2

V to 1.0 V vs. RHE, at rotation rates from 400 to 4000 rpm and a scan rate of 10 mV s^{-1}.

Alcohol crossover effect was observed on each electrocatalyst using CV by contaminating the electrolyte in use with 4mL of 1M EtOH.

4.4.1 ORR Polarization Curves

The electrocatalytic performance of each sample toward ORR was probed using CV and a peak is observed around 0.5–0.8 V vs. RHE (**Figure 4.40a**) for all the materials. This peak is attributable to oxygen reduction, suggesting ORR activity.

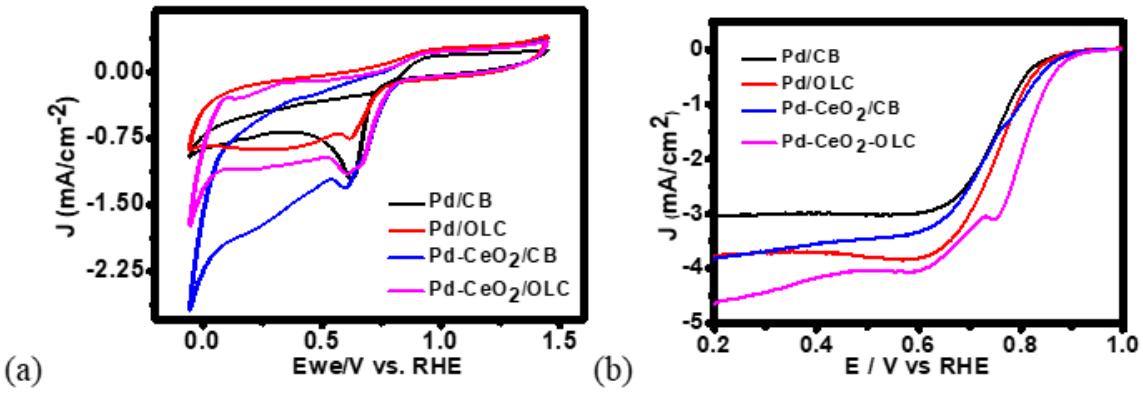


Figure 4.40: (a) CV curves (b) Linear sweep voltammograms at 1600 rpm**.**

From the RDE polarization curves of the ORR for the Pd/CB, Pd-CeO_2/CB, Pd/OLC and Pd-CeO_2/OLC electrodes at different rotation speeds (**Figure 4.41**), the diffusion rate of the oxygen molecules is observed to increase with increasing RDE speeds. Therefore, the *j* (diffusion-limited current density) also increases.

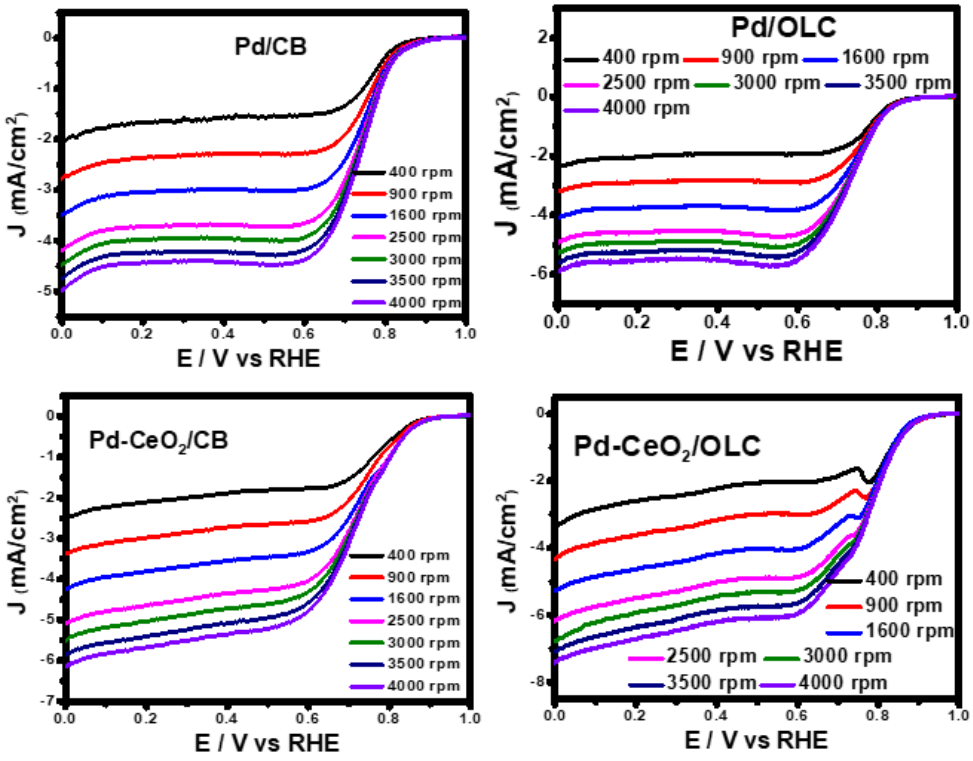


Figure 4.41: Linear sweep voltammograms for the catalysts at rotation rates between 400 and 2500 rpm.

Table 4.14: Summary of the ORR performance (@ 1600 rpm).

Sample	E_{onset} (V vs. RHE)	$E_{1/2}$ (V vs. RHE)	Diffusion-limited current density @ +0.2 V (mA cm^{-2})
Pd/CB	0.912	0.747	-3.041
Pd/OLC	0.956	0.760	-3.740
Pd-CeO2/CB	0.958	0.752	-3.821
Pd-CeO2/OLC	0.962	0.766	-4.601

The polarization curves of the electrocatalysts in **Figure 4.40b** are compared at the rotation of 1600 rpm and summarized in **Table 4.13**. From the table, Pd-

CeO_2/OLC is observed to have an earlier E_{onset} and greater j values than the other samples, suggesting its better performance toward ORR.

The K-L plots at different potentials of the samples (**Figure 4.42**) show a very linear graph with consistent slopes, indicating a first order reaction-kinetics. This suggests that the ORR is controlled by mass transport of the oxygen species as well as kinetics at the surface of the electrode [42, 51].

The Koutecky-Levich equations are useful in analyzing the kinetic parameters (**Equation 4.14 – 4.17)** [43,44,50]:

$$\frac{1}{J_{lim}} = \frac{1}{J_K} + \frac{1}{J_L} = \frac{1}{J_K} + \frac{1}{B_L\omega^{1/2}} \qquad \textbf{4.14}$$

Where:

$$J_L = B_L\omega^{1/2} \qquad \textbf{4.15}$$

$$J_K = nFKCo \qquad \textbf{4.16}$$

$$B_L = \frac{1}{slope} = 0.62nFCoD^{2/3}\upsilon^{-1/6} \qquad \textbf{4.17}$$

where J_{lim}, and J_L are the measured, kinetic, and diffusion-limiting current densities, respectively. Ω (=2πN) is the angular velocity (where N is the linear rotation speed), k is the electron-transfer rate constant, while n, C_0, D, u, and F retain their meanings as previously described in **Chapter 2** (**Section 2.7.6.1**).

The values of C_o, D *and* v in 0.1 M KOH are 1.2 x 10^{-6} mol cm^{-3}, 1.9 x 10^{-5} cm^2 s^{-1} and 0.01 cm^2 s^{-1} respectively [45].

The slope was used to obtain n (**Equation 4.17**), while J_K was derived from the Y-intercept.

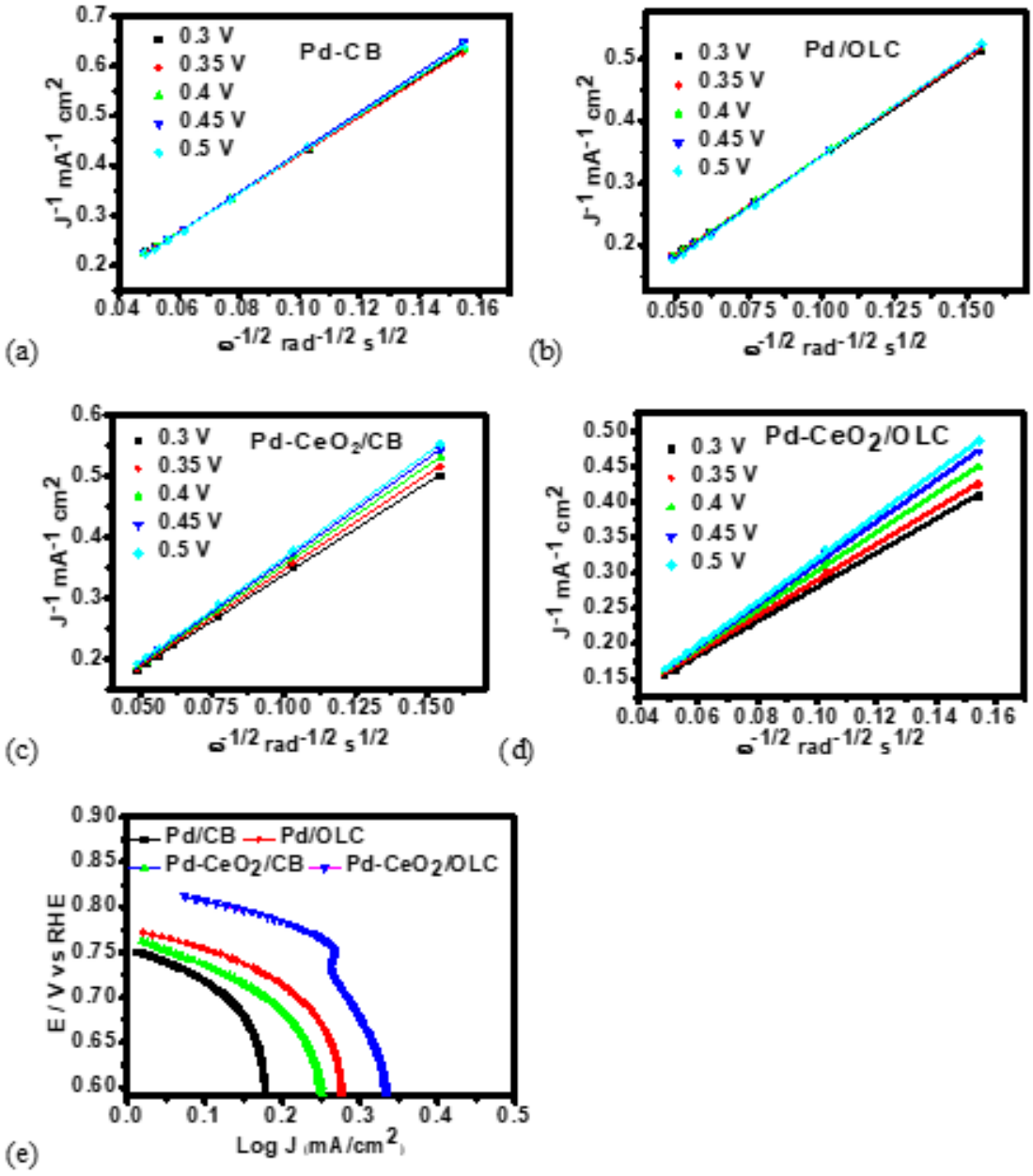


Figure 4.42: (a-d) The K-L plots for the samples at various overpotentials (0.3, 0.35, 0.4, 0.45 and 0.5 V). (e) Tafel plots of all the samples 10 wt% Pd.

From the K–L plot, the n values for the nanocomposites were calculated to be 2.32, 2.83, 2.80 and 3.32 for Pd/CB, Pd/OLC, Pd-CeO_2/CB and Pd-CeO_2/OLC respectively, which is a suggestion that the ORR kinetics of these electrocatalysts proceed through the 2-electron pathway [52].

From the Y-intercept, the kinetic current densities (J_K) are (28.539, 25.807, 30.276, 39.557, 37.037), (33.830, 37.023, 43.802, 54.555, 80.645), (28.580, 30.694, 35.174, 40.209, 41.305) and (25.674, 27.049, 33.979, 48.054, 67.797) for Pd/CB, Pd/OLC, Pd-CeO_2/CB and Pd-CeO_2/OLC.

The kinetic rate constants (k) were estimated as 1.20×10^{-1}, 1.53×10^{-1}, 1.09×10^{-1} and 1.05×10^{-1} cm s^{-1} for the Pd/CB, Pd/OLC, Pd-CeO_2/CB and Pd-CeO_2/OLC respectively.

For the Tafel plot, the kinetic current (J_K) was calculated from the mass-transport correction of RDE by **Equation 4.18** [46-49]:

$$J_K = \frac{J \times J_L}{J_L - J} \qquad \textbf{4.18}$$

$$E_{app} = E_{eq} - b \log J_K \qquad \textbf{4.19}$$

$$E_{app} = E_{eq} - \frac{RT}{\alpha n F} \log J_K \qquad \textbf{4.20}$$

With J being the measured current density, and J_K and J_L retain their meanings, and E_{app} and E_{eq} are the applied potential and equilibrium potential, respectively.

From the Tafel plot (E_{app} vs. log J_K), the slope values of Pd/CB, Pd/OLC, Pd-CeO_2/CB and Pd-CeO_2/OLC were obtained as 300, 218.4, 343.8 and 191.2 mV dec^{-1}, respectively. It is clear that the slope of Pd-CeO_2/OLC is the lowest, which is a confirmation of its ORR outperformance.

4.4.2 Accelerated Durability Test

From the results, Pd-CeO_2/OLC is seen to give off the best ORR performance, prompting the investigation of its stability using voltammograms to 5000 and 15000 cycles, the activity of the Pd/CeO_2-OLC is observed to decrease by

11.6% and 43.1% after 5000 cycles and 15000 cycles respectively (**Figure 4.43**).

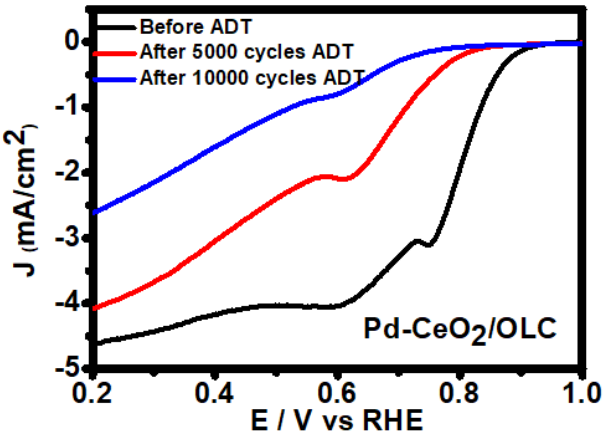


Figure 4.43: Stability test of the Pd-CeO_2/OLC catalysts towards ORR at the rotation rate of 1600 rpm after 5000 and 15000 cycles.

4.4.3 Tolerance to ethanol crossover effect

Alcohol cross-over leads to high overvoltage, and this affects the ORR activities negatively [53 - 55]. Ethanol cross-over effect was checked by depositing 4 mL of 1 M ethanol into the O_2-saturated 0.1 M KOH and running CV at 50 mV/s (**Figure 4.44**). There was only a slight change in the CVs obtained for Pd/CB, clearly showing that the Pd/CB catalyst has the best tolerance to contamination with ethanol compared to the other catalysts which unlike Pd/CB showed increased oxidation activity of ethanol upon contamination with ethanol.

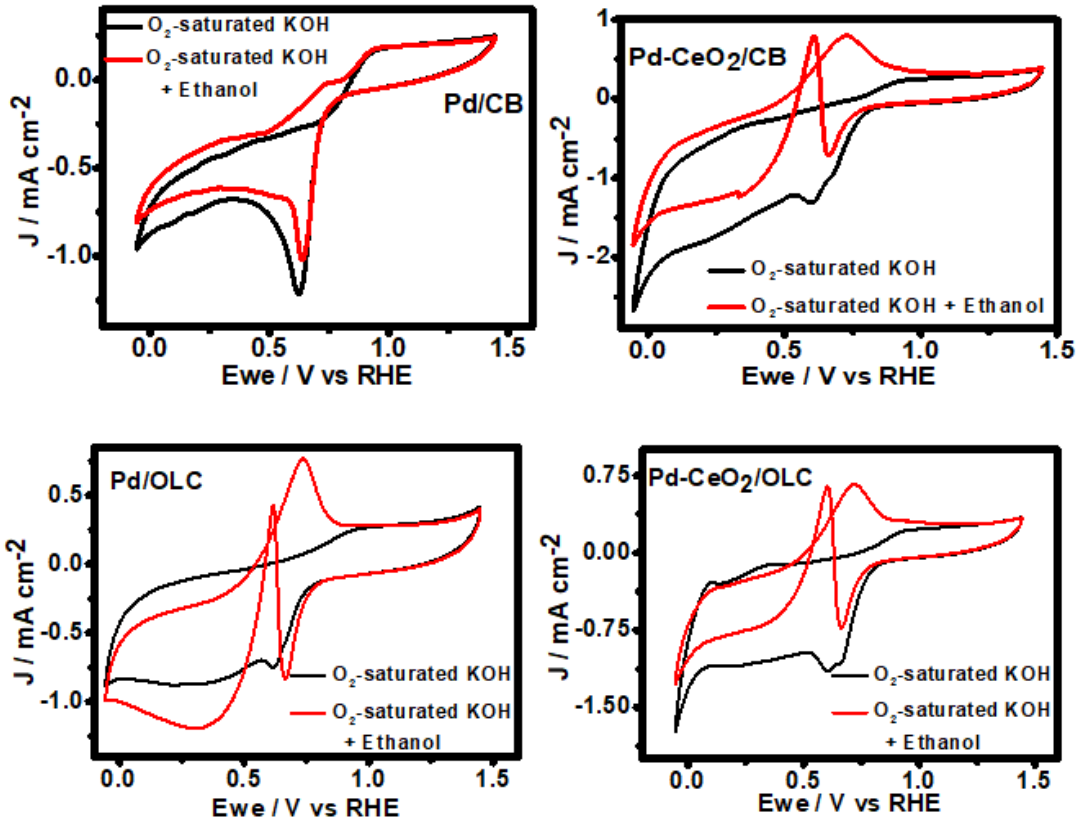


Figure 4.44: Cyclic voltammetric evolutions of the samples in oxygen-saturated KOH with and without ethanol.

4.4.4 DFT Simulation Results

The DFT simulations (**Figure 4.45**) show that the adsorption energies are in the order Pd/CB < Pd-CeO_2/CB < Pd/OLC < Pd-CeO_2/OLC (**Table 4.14**). The presence of CeO_2 allows the adsorbates of the ORR atom to be weakly adsorbed on the Pd. The more negative the A.E. value, the weaker the energy and the more thermodynamically favorable.

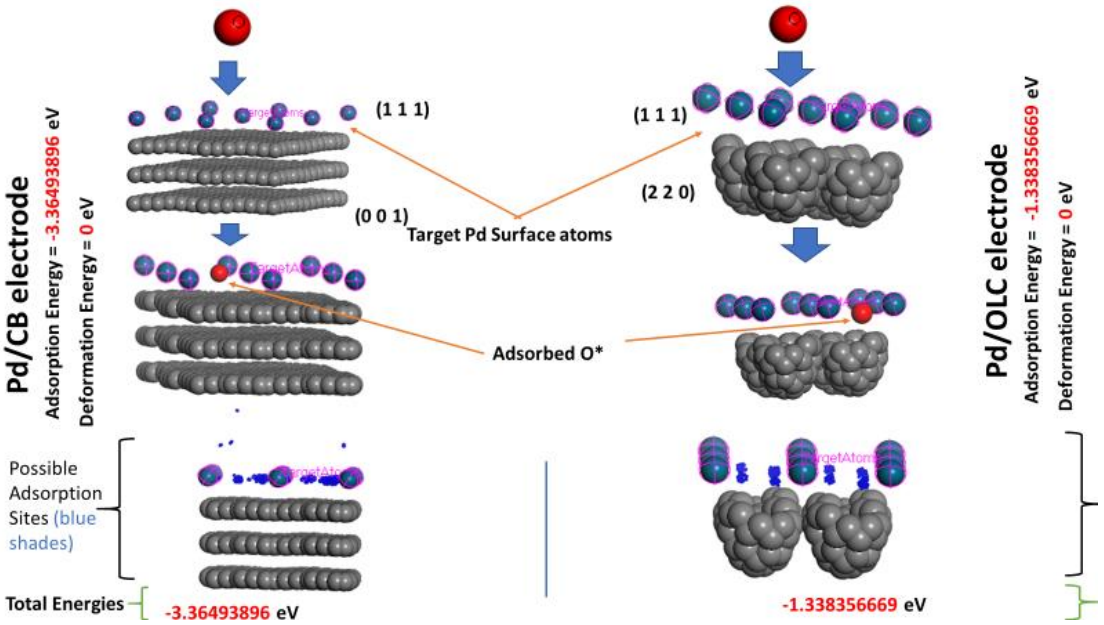


Figure 4.45a: The interactions between O* and the Pd/CB and Pd/OLC catalysts.

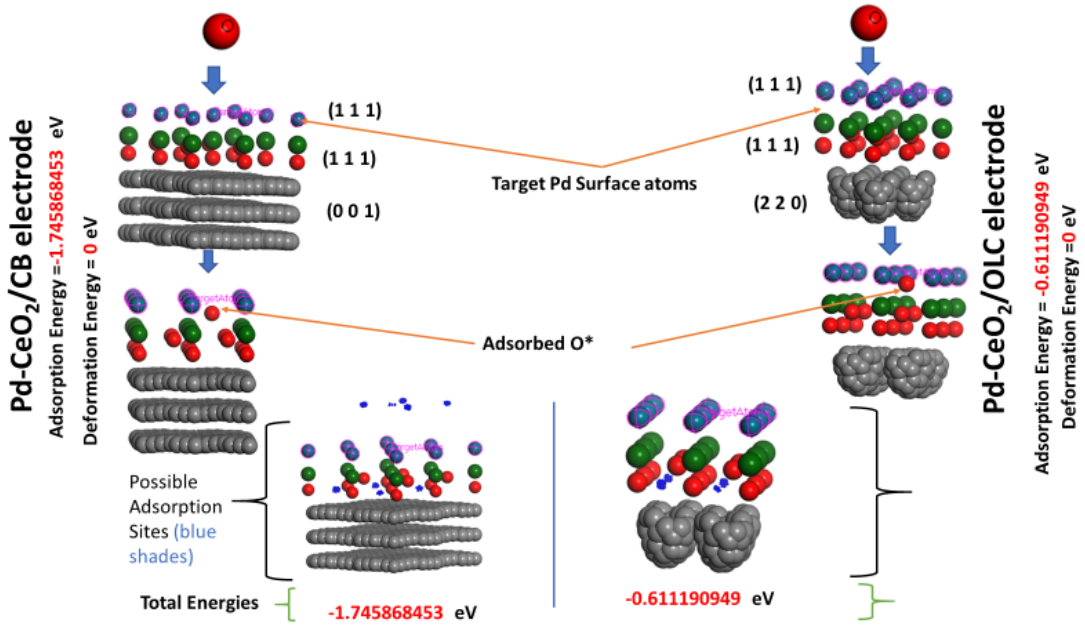


Figure 4.45b: The interactions between O* and the Pd-CeO_2/CB and Pd-CeO_2/OLC catalysts.

Table 4.15: The different energies calculated for the ORR at the electrodes.

Electrode	Adsorbate	Gibbs F.E (eV)	A.E (eV)	D.E (eV)	E_f (eV)	E_g (eV)	K.E (Ha)
Pd/CB	O*	-3.365	-3.365	0	-2.063	0.582	-277.311
Pd/OLC	O*	-1.338	-1.338	0	-3.517	0.433	-109.200
Pd-CeO_2/CB	O*	-1.746	-1.746	0	-5.774	0.523	-897.591
Pd-CeO_2/OLC	O*	-0.611	-0.611	0	-4.373	0.176	-170.586

The purpose of DFT is to unravel the interplay amongst the carbon/carbon-ceria supports and conductivity and interaction with adsorbates in determining the electrocatalytic performance of the catalysts.

Since the adsorption energy of Pt or Pd catalyst on curved carbon support is higher than on a flat carbon support [56,57], it is not surprising that OLC binds more strongly than CB.

However, from literature the weaker the binding, the better. This suggests that the reason for the better behavior of the catalysts with stronger binding may be related to the bandgap (conductivity). Although the binding is strong, the conductivity is higher (smaller bandgap), which makes it easier for electrocatalysis than for poisoning to occur.

H* adsorption is best when Gibb energy is close to zero. Thus, the binding energy decreases as follows Pd-CeO_2/OLC > Pd/OLC >Pd-CeO_2/CB > Pd/CB. This is in agreement with literature [58]. This also follows with conductivity. It also means that OLC is better than CB support.

References

1. A. Vinu, P. Srinivasu, M. Takahashi, T. Mori, V. V. Balasubramanian, and K. Ariga, “Controlling the textural parameters of mesoporous carbon materials,” *Microporous Mesoporous Mater.*, 2007, 100(1-3), 20-26. https://doi.org/10.1016/j.micromeso.2006.10.008

2. T. Wang *et al.*, “Synthesis of ordered mesoporous boron-containing carbon films and their corrosion behavior in simulated proton exchange membrane fuel cells environment,” *J. Power Sources*, 2012, 212, 1-12. https://doi.org/10.1016/j.jpowsour.2012.03.068

3. T. V. Reshetenko *et al.*, “Catalytic filamentous carbon: Structural and textural properties,” *Carbon N. Y.*, 2003, 41(8), 1605-1615. https://doi.org/10.1016/S0008-6223(03)00115-5

4. J. G. Li, C. Y. Tsai, and S. W. Kuo, “Fabrication and characterization of inorganic silver and palladium nanostructures within hexagonal cylindrical channels of mesoporous carbon,” *Polymers (Basel).*, 2014, 6(6), 1794-1809. https://doi.org/10.3390/polym6061794

5. F. Li, B. Zhang, S. Dong, and E. Wang, “A novel method of electrodepositing highly dispersed nano palladium particles on glassy carbon electrode,” *Electrochim. Acta*, 1997, 42(16), 2563-2568. https://doi.org/10.1016/S0013-4686(96)00450-1

6. M. M. O. Thotiyl, T. R. Kumar, and S. Sampath, “Pd supported on titanium nitride for efficient ethanol oxidation,” *J. Phys. Chem. C*, 2010, 114(41), 17934–17941. https://doi.org/10.1021/jp1038514

7. Z. Liu and L. Hong, “Electrochemical characterization of the electrooxidation of methanol, ethanol and formic acid on Pt/C and

PtRu/C electrodes," *J. Appl. Electrochem.*, 2007, 37, 505–510. https://doi.org/10.1007/s10800-006-9282-0

8. J. Liu, J. Ye, C. Xu, S. P. Jiang, and Y. Tong, "Kinetics of ethanol electrooxidation at Pd electrodeposited on Ti," *Electrochem. commun.*, 2007, 9(9), 2334-2339. https://doi.org/10.1016/j.elecom.2007.06.036

9. A. K. Ipadeola, R. Barik, S. C. Ray, and K. I. Ozoemena, "Bimetallic Pd/SnO2 Nanoparticles on Metal Organic Framework (MOF)-Derived Carbon as Electrocatalysts for Ethanol Oxidation," *Electrocatalysis*, 2019, 10, 366–380. https://doi.org/10.1007/s12678-019-00518-5

10. R. Guidelli *et al.*, "Defining the transfer coefficient in electrochemistry: An assessment (IUPAC Technical Report)," in *Pure and Applied Chemistry*, 2014, 86(2), 245–258. https://doi.org/10.1515/pac-2014-5026

11. A. V. Tripković, K. D. Popović, J. D. Momčilović, and D. M. Dražić, "Kinetic and mechanistic study of methanol oxidation on a Pt(111) surface in alkaline media," *J. Electroanal. Chem.*, 1996, 418(1-2), 9-20. https://doi.org/10.1016/S0022-0728(96)04849-8

12. V. Rao, Hariyanto, C. Cremers, and U. Stimming, "Investigation of the ethanol electrooxidation in alkaline membrane electrode assembly by differential electrochemical mass spectrometry," *Fuel Cells*, 2007, 7(5), 417 – 423. https://doi.org/10.1002/fuce.200700026

13. Y. Jiang, Y. Lu, F. Li, T. Wu, L. Niu, and W. Chen, "Facile electrochemical codeposition of 'clean' graphene-Pd nanocomposite as an anode catalyst for formic acid electrooxidation," *Electrochem. commun.*, 2012, 19, 21-24. https://doi.org/10.1016/j.elecom.2012.02.035

14. N. W. Maxakato, K. I. Ozoemena, and C. J. Arendse, "Dynamics of electrocatalytic oxidation of ethylene glycol, methanol and formic acid at

MWCNT platform electrochemically modified with Pt/Ru nanoparticles," *Electroanalysis*, 2010, 22(5), 519-529. doi: 10.1002/elan.200900397.

15. N. W. Maxakato, C. J. Arendse, and K. I. Ozoemena, "Insights into the electro-oxidation of ethylene glycol at Pt/Ru nanocatalysts supported on MWCNTs: Adsorption-controlled electrode kinetics," *Electrochem. commun.*, 2009, 11(3), 534-537. https://doi.org/10.1016/j.elecom.2008.12.038

16. E. Antolini and E. R. Gonzalez, "Alkaline direct alcohol fuel cells," *J. Power Sources*, 2010, 195(11), 3431-3450. https://doi.org/10.1016/j.jpowsour.2009.11.145

17. O. H. Han, "Direct Alcohol Fuel Cells Investigated by NMR Spectroscopy at the Korea Basic Science Institute," *J. Anal. Sci. Technol.*, 2011, 2, A168-A172. doi: 10.5355/jast.2011.a168.

18. S. S. Li, H. P. Cong, P. Wang, and S. H. Yu, "Flexible nitrogen-doped graphene/carbon nanotube/Co3O 4 paper and its oxygen reduction activity," *Nanoscale*, 2014,6, 7534-7541, https://doi.org/10.1039/c4nr02101k

19. D. A. J. Rand, R. Woods, *Journal of Electroanalytical Chemistry*, 1971, 31(1), 29 - 38.

20. V. Bambagioni *et al.*, "Energy efficiency enhancement of ethanol electrooxidation on Pd-CeO2/C in passive and active polymer electrolyte-membrane fuel cells," *ChemSusChem*, 2012, 5(7), 1266-1273. doi: 10.1002/cssc.201100738.

21. B. Ravel and M. Newville, "ATHENA, ARTEMIS, HEPHAESTUS: Data analysis for X-ray absorption spectroscopy using IFEFFIT," in *Journal of Synchrotron Radiation*, 2005, *12*, 537–541. https://doi.org/10.1107/S0909049505012719

22. C. Bianchini and P. K. Shen, “Palladium-based electrocatalysts for alcohol oxidation in half cells and in direct alcohol fuel cells,” *Chem. Rev.*, 2009, 109(9) 4183–4206. doi: 10.1021/cr9000995.

23. J. Pillay and K. I. Ozoemena, “Layer-by-layer self-assembled nanostructured phthalocyaninatoiron(II)/SWCNT-poly(m-aminobenzenesulfonic acid) hybrid system on gold surface: Electron transfer dynamics and amplification of H2O2 response,” *Electrochim. Acta*, 2009, 54(22) 5053–5059. doi: 10.1016/j.electacta.2008.12.056.

24. K. I. Ozoemena, N. S. Mathebula, J. Pillay, G. Toschi, and J. A. Verschoor, “Electron transfer dynamics across self-assembled N-(2-mercaptoethyl) octadecanamide/mycolic acid layers: Impedimetric insights into the structural integrity and interaction with anti-mycolic acid antibodies,” *Phys. Chem. Chem. Phys.*, 2010, 12(2), 345 – 357. doi: 10.1039/b915930d.

25. Y. Luo, L. Calvillo, C. Daiguebonne, M. K. Daletou, G. Granozzi, and N. Alonso-Vante, “A highly efficient and stable oxygen reduction reaction on Pt/CeOx/C electrocatalyst obtained via a sacrificial precursor based on a metal-organic framework,” *Appl. Catal. B Environ.*, 2016, 189, 39-50. doi: 10.1016/j.apcatb.2016.02.028.

26. J. Yang, S. H. Kim, S. K. Kwak, and H. K. Song, “Curvature-Induced Metal-Support Interaction of an Islands-by-Islands Composite of Platinum Catalyst and Carbon Nano-onion for Durable Oxygen Reduction,” *ACS Appl. Mater. Interfaces*, 2017, 9, 28, 23302–23308. doi: 10.1021/acsami.7b04410.

27. M. Luo and S. Guo, “Strain-controlled electrocatalysis on multimetallic nanomaterials,” Nature Reviews Materials. 2017, 2, 17059. doi: 10.1038/natrevmats.2017.59.

28. M. Mavrikakis, B. Hammer, and J. K. Nørskov, “Effect of strain on the reactivity of metal surfaces,” Phys. Rev. Lett., 1998, 81, 2819 – 2822. doi: 10.1103/PhysRevLett.81.2819.

29. Y. Lu, Y. Jiang, X. Gao, X. Wang, and W. Chen, “Strongly coupled pd nanotetrahedron/tungsten oxide nanosheet hybrids with enhanced catalytic activity and stability as oxygen reduction electrocatalysts,” J. Am. Chem. Soc., 2014, 136, 11687–11697. doi: 10.1021/ja5041094.
30. J. Wang et al., “Recent advances in Pt-based octahedral nanocrystals as high performance fuel cell catalysts,” Journal of Materials Chemistry A. 2016, 4, 11559–11581. doi: 10.1039/c6ta02748b.
31. M. Ren, Y. Zhou, F. Tao, Z. Zou, D. L. Akins, and H. Yang, “Controllable modification of the electronic structure of carbon-supported core-shell cu@pd catalysts for formic acid oxidation,” J. Phys. Chem. C, 2014, 118, 12669–12675. doi: 10.1021/jp5033417.
32. P. Strasser et al., “Lattice-strain control of the activity in dealloyed core-shell fuel cell catalysts,” Nat. Chem., 2010, 2, 454–460. doi: 10.1038/nchem.623.
33. L. An *et al.*, “A highly active and durable iron/cobalt alloy catalyst encapsulated in N-doped graphitic carbon nanotubes for oxygen reduction reaction by a nanofibrous dicyandiamide template,” *J. Mater. Chem. A*, 2018, 6(14), 5962 – 5970. doi: 10.1039/c8ta01247d.
34. Y. Zhan *et al.*, “Non Noble Metal Catalyst for Oxygen Reduction Reaction and Its Characterization by Simulated Fuel Cell Test,” *J. Electrochem. Soc.*, 2018, 165(15) J3008. doi: 10.1149/2.0021815jes.
35. E. S. Davydova, S. Mukerjee, F. Jaouen, and D. R. Dekel, “Electrocatalysts for Hydrogen Oxidation Reaction in Alkaline Electrolytes,” *ACS Catal.*, 2018, 8, 6665 – 6690. doi: 10.1021/acscatal.8b00689.
36. T. Bhowmik, M. K. Kundu, and S. Barman, “Palladium Nanoparticle-Graphitic Carbon Nitride Porous Synergistic Catalyst for Hydrogen Evolution/Oxidation Reactions over a Broad Range of pH and Correlation of Its Catalytic Activity with Measured Hydrogen Binding

Energy," *ACS Catal.*, 2016, 6(3), 1929 – 1941. doi: 10.1021/acscatal.5b02485.

37. S. Lu and Z. Zhuang, "Investigating the Influences of the Adsorbed Species on Catalytic Activity for Hydrogen Oxidation Reaction in Alkaline Electrolyte," *J. Am. Chem. Soc.*, 2017, 139, 5156 – 5163. doi: 10.1021/jacs.7b00765.
38. Z. Yang, Y. Ling, Y. Zhang, and G. Xu, "High Performance Palladium Supported on Nanoporous Carbon under Anhydrous Condition," *Sci. Rep.*, 2016, *6*, 36521. doi: 10.1038/srep36521.
39. A. K. Ipadeola, P. V. Mwonga, S. C. Ray, R. R. Maphanga, and K. I. Ozoemena, "Palladium/Stannic Oxide Interfacial Chemistry Promotes Hydrogen Oxidation Reactions in Alkaline Medium," *ChemElectroChem*, 2020, *7, 4562–4571.* doi: 10.1002/celc.202000952.
40. W. Sheng, H. A. Gasteiger, and Y. Shao-Horn, "Hydrogen Oxidation and Evolution Reaction Kinetics on Platinum: Acid vs Alkaline Electrolytes," *J. Electrochem. Soc.*, 2010, 157(11), B1529 – B153. doi: 10.1149/1.3483106.
41. N. M. Marković, S. T. Sarraf, H. A. Gasteiger, and P. N. Ross, "Hydrogen electrochemistry on platinum low-index single-crystal surfaces in alkaline solution," *J. Chem. Soc. - Faraday Trans.*, 1996, 92(20), 3719 – 3725. doi: 10.1039/ft9969203719.
42. J. Tian *et al.*, "Oxygen reduction reaction and hydrogen evolution reaction catalyzed by Pd–Ru nanoparticles encapsulated in porous carbon nanosheets," *Catalysts*, 2018, 8(8), 329. https://doi.org/10.3390/catal8080329
43. U. A. Paulus *et al.*, "Oxygen reduction on carbon-supported Pt-Ni and Pt-Co alloy catalysts," *J. Phys. Chem. B*, 2002, 106(16), 4181–4191. doi: 10.1021/jp013442l

44. Y. Feng and N. Alonso-Vante, “Carbon-supported cubic CoSe 2 catalysts for oxygen reduction reaction in alkaline medium,” *Electrochim. Acta*, 2012, 72, 129-133. doi: 10.1016/j.electacta.2012.04.003.

45. Y. Zhang *et al.*, “Integrated Pt2Ni alloy@Pt core-shell nanoarchitectures with high electrocatalytic activity for oxygen reduction reaction,” *J. Mater. Chem. A*, 2014, 2, 11400-11407. https://doi.org/10.1039/c4ta00731j

46. I. Koç, M. Çamur, M. Bulut, and A. R. Özkaya, “Electrocatalytic performances of carbon supported metallophthalocyanine and pt/metallophthalocyanine catalysts towards dioxygen reduction in acidic medium,” *Catal. Letters*, 2009, 131, 370–380. doi: 10.1007/s10562-009-0075-z.

47. L. L. An, Y. Chen, J. Shi, J. Cao, B. Liu, and J. Yang, “Oxygen reduction activity and stability of composite Pdx/Co-nanofilms/C electrocatalysts in acid and alkaline media,” *Front. Chem.*, 2018, 6, 596. https://doi.org/10.3389/fchem.2018.00596

48. Y. Li *et al.*, “Synthesis of bimetallic Pt-Pd core-shell nanocrystals and their high electrocatalytic activity modulated by Pd shell thickness,” *Nanoscale*, 2012, 4, 845-851. doi: 10.1039/c1nr11374g

49. Y. Liang *et al.*, “Co3O4 nanocrystals on graphene as a synergistic catalyst for oxygen reduction reaction,” *Nat. Mater.*, 2011, 10(10), 780.doi: 10.1038/nmat3087

50. L. R. Faukner and A. J. Bard, Electrochemical Methods: Fundamentals and Applications, Wiley, New York, 2nd edition, 2001.

51. O. O. Fashedemi and K. I. Ozoemena, “Oxygen reduction reaction at MWCNT-modified nanoscale iron(ii) tetrasulfophthalocyanine: Remarkable performance over platinum and tolerance toward methanol in alkaline medium,” *RSC Adv.*, 2015, 5, 22869-22878. doi: 10.1039/c5ra03133h

52. S. Soren, I. Hota, A. K. Debnath, D. K. Aswal, K. S. K. Varadwaj, and P. Parhi, “Oxygen Reduction Reaction activity of microwave mediated solvothermal synthesized CeO2/g-C3N4 nanocomposite,” *Front. Chem.*, 2019, 7, 403. doi: 10.3389/fchem.2019.00403

53. E. Antolini and E. R. Gonzalez, “Alkaline direct alcohol fuel cells,” *J. Power Sources*, 2010, 195(11), 3431-3450. https://doi.org/10.1016/j.jpowsour.2009.11.145

54. O. H. Han, “Direct Alcohol Fuel Cells Investigated by NMR Spectroscopy at the Korea Basic Science Institute,” *J. Anal. Sci. Technol.*, 2011, 2, A168-A172. doi: 10.5355/jast.2011.a168

55. S. S. Li, H. P. Cong, P. Wang, and S. H. Yu, “Flexible nitrogen-doped graphene/carbon nanotube/Co3O 4 paper and its oxygen reduction activity,” *Nanoscale*, 2014, 6, 7534-7541. https://doi.org/10.1039/c4nr02101k

56. J. Yang, S. H. Kim, S. K. Kwak, and H. K. Song, “Curvature-Induced Metal-Support Interaction of an Islands-by-Islands Composite of Platinum Catalyst and Carbon Nano-onion for Durable Oxygen Reduction,” *ACS Appl. Mater. Interfaces*, 2017, 9, 23302−23308. doi: 10.1021/acsami.7b04410

57. N. T. Cuong, A. Fujiwara, T. Mitani, and D. H. Chi, “Effects of carbon supports on Pt nano-cluster catalyst,” *Comput. Mater. Sci.*, 2008, 44(1), 163-166. doi: 10.1016/j.commatsci.2008.01.061

58. J. Zhu, L. Hu, P. Zhao, L. Y. S. Lee, and K. Y. Wong, “Recent Advances in Electrocatalytic Hydrogen Evolution Using Nanoparticles,” *Chemical Reviews*. 2020, 120, 851−918. doi: 10.1021/acs.chemrev.9b00248.

59. A. Arumugam, C. Karthikeyan, A. S. Haja Hameed, K. Gopinath, S. Gowri, and V. Karthika, “Synthesis of cerium oxide nanoparticles using Gloriosa superba L. leaf extract and their structural, optical and antibacterial properties,” Mater. Sci. Eng. C, 2015, 49, 408 – 415. doi: 10.1016/j.msec.2015.01.042.

60. S. Tsunekawa, T. Fukuda, and A. Kasuya, “X-ray photoelectron spectroscopy of monodisperse CeO2-x nanoparticles,” Surf. Sci., 2000, 457, L437–L440. doi: 10.1016/S0039-6028(00)00470-2.

61. D.R. Mullins, S.H. Overbury, D.R. Huntley, “Electron Spectroscopy of Single Crystal and Polycrystalline Cerium Oxide Surfaces,” Surf. Sci., 1998, 409, 307-319. http://dx.doi.org/10.1016/S0039-6028(98)00257-X.

62. R. Vercaemst, D. Poelman, R. L. Van Meirhaeghe, L. Fiermans, W. H. Laflère, and F. Cardon, “An XPS study of the dopants’ valence states and the composition of CaS1 - xSex:Eu and SrS1 - xSex:Ce thin film electroluminescent devices,” J. Lumin., 1995, 63, 19 – 30. doi: 10.1016/0022-2313(94)00059-L.

63. G. Wang, Q. Mu, T. Chen, and Y. Wang, “Synthesis, characterization and photoluminescence of CeO2 nanoparticles by a facile method at room temperature,” J. Alloys Compd., 2010, 493, 202 – 207. doi: 10.1016/j.jallcom.2009.12.053.

64. Y. C. Wei, C. W. Liu, W. Da Kang, C. M. Lai, L. D. Tsai, and K. W. Wang, “Electro-catalytic activity enhancement of Pd-Ni electrocatalysts for the ethanol electro-oxidation in alkaline medium: The promotional effect of

CeO_2 addition," J. Electroanal. Chem., 2011, 660(1), 64-70. doi: 10.1016/j.jelechem.2011.06.006.

65. H. Mao, L. Wang, P. Zhu, Q. Xu, and Q. Li, "Carbon-supported PdSn-SnO_2 catalyst for ethanol electro-oxidation in alkaline media," in International Journal of Hydrogen Energy, 2014, 39(31), 17583–17588. doi: 10.1016/j.ijhydene.2014.08.079.

66. Q. Dong, Y. Zhao, X. Han, Y. Wang, M. Liu, and Y. Li, "Pd/Cu bimetallic nanoparticles supported on graphene nanosheets: Facile synthesis and application as novel electrocatalyst for ethanol oxidation in alkaline media," Int. J. Hydrogen Energy, 2014, 39(27), 14669-14679. doi: 10.1016/j.ijhydene.2014.06.139.

CHAPTER 5

CONCLUSION AND RECOMMENDATION

This chapter concludes the dissertation and offers recommendations for future work.

5.1 Conclusion

5.1.1 Physical Properties

The aim of the study was to synthesize nanostructured palladium-based composites: Pd/CB, Pd-CeO_2/CB, Pd/OLC and Pd-CeO_2/OLC. This study successfully synthesized the various required materials confirmed by XRD, XPS, TGA and EDX. The prepared samples were examined for physical properties and were observed to be exhibiting different structural morphologies, while the materials supported on OLC exhibited the smallest particle sizes and higher porosity.

5.1.2 Ethanol Oxidation and ADEFC Test

The electrochemical behaviours of the catalysts towards ethanol oxidation were probed using a three-electrode setup and a two-electrode setup in alkaline medium. Both experiments revealed Pd-CeO_2/OLC as the best performing electrocatalyst for the electrooxidation of ethanol.

The larger surface area, pore volume and small particle size of Pd-CeO_2/OLC gives it an edge over the rest in terms of the catalytic activity and stability for the electrooxidation reactions of ethanol. This is evidenced by the negative shift to an earlier or lower onset potential and the significantly higher current densities for the reaction on Pd-CeO_2/OLC. However, the existence of Pd-

complexes on the catalyst-modified electrodes didn't allow for proper surface coverage analysis.

5.1.3 Electrocatalysts for Hydrogen Oxidation and Oxygen Reduction Reactions in Alkaline Environment

- ❖ Alkaline HOR and ORR tests were performed on the electrocatalysts (Pd/CB, Pd-CeO_2/CB, Pd/OLC and Pd/CeO_2/OLC).
- ❖ The addition of the CeO_2 to the Pd electrocatalysts enhances their performances toward the alkaline HOR.
- ❖ For the alkaline ORR, the presence of CeO_2 in the Pd-based electrocatalysts enhanced the activity. However, the materials containing OLC showed better behaviors.

5.2 Recommendations for Future Directions

For the next step of this research the following activities may be considered:

- The electrocatalysts with the best activity can be tested for fuel cell-based breath ethanol sensor, and the best fabricated for real-life application.
- Rotating Ring Disk Electrode (RRDE) studies will be carried out to confirm the ORR reaction pathway.
- Composites and electrocatalysts can be varied for further tests on the physicochemical properties of the electrocatalysts for use in energy conversion devices.
- The use of spray pyrolysis to deposit slurries of the catalysts on the substrates (nickel foam and Toray carbon paper) for the micro ADEFC testing.